MICROSTRUCTURAL REMODELING OF VENTRICULAR CARDIOMYOCYTES IN DISEASE AND THEIR RESTORATION AFTER THERAPY

by

Justin George Lichter

A dissertation submitted to the faculty of
The University of Utah
in partial fulfillment of the requirements for the degree of

Doctor of Philosophy

Department of Bioengineering

The University of Utah

May 2016

The University of Utah Graduate School

STATEMENT OF DISSERTATION APPROVAL

The dissertation of **Justin George Lichter**

has been approved by the following supervisory committee members:

Frank Sachse	, Chair	**12/17/2015** Date Approved
Kenneth W Spitzer	, Member	**12/17/2015** Date Approved
John H B Bridge	, Member	**12/17/2015** Date Approved
Robert W Hitchcock	, Member	**12/17/2015** Date Approved
Robert S Macleod	, Member	**12/29/2015** Date Approved

and by **Patrick A Tresco** , Chair/Dean of the Department/College/School of **Bioengineering**

and by David B. Kieda, Dean of The Graduate School.

ABSTRACT

In this thesis I present novel findings of microstructural remodeling that occurs during dyssynchronous heart failure (DHF) and the ability for cardiac resynchronization therapy (CRT) to reverse this remodeling. DHF is an advanced disease state that occurs in a large portion of patients suffering from heart failure. Mechanical dyssynchrony between the left and right ventricles of the heart, the hallmark of DHF, results in significantly increased heterogeneity of stress in the cardiac wall. DHF severely limits cardiac performance, decreasing quality of life and increasing mortality. The main therapy for treating DHF is CRT, a therapy in which mechanical synchrony is restored to the ventricles via electrical pacing. The success of CRT varies widely. Scientific knowledge surrounding DHF and CRT is surprisingly sparse for how widespread the disease and therapy are. A better understanding of the subcellular structure and function altered during DHF will improve our understanding of the disease and potentially help develop novel therapies and even lead to development of assays capable of better predicting success of current therapies. Here we use confocal microscopy to explore protein distributions within isolated cardiomyocytes and intact tissue, Ca^{2+} handling during activation and relaxation of stimulated cardiomyocytes, and to develop a method for quantifying strain in 2D image sequences of contracting cardiomyocytes at an unprecedented spatiotemporal resolution.

Specifically I will demonstrate that α-actinin, the protein comprising the majority of the sarcomeric Z-disk, is significantly altered during DHF and that CRT is able to partially reverse this remodeling. I will then present findings on remodeling of the transverse tubular system and associated ryanodine receptor clusters, both crucial components of excitation-contraction coupling. In particular, I will show that these structures exhibit subcellular heterogeneity during DHF, affecting excitation-contraction coupling. This heterogeneity is reduced after CRT, indicating previously unknown capabilities of restoration. Finally, I will present a novel method to characterize strain within contracting cardiomyocytes. This method expands on previous methods by providing a regional 2D strain tensor at unprecedented spatiotemporal resolution, allowing more accurate description of the mechanical properties of the cell. Together, this work makes a significant contribution to the understanding of DHF and CRT.

This work is dedicated to my mother, who always encouraged
my enthusiasm for science and engineering.

Concetta Lichter
1957-2015

TABLE OF CONTENTS

LIST OF TABLES

Tables

LIST OF ABBREVIATIONS

1D	ONE-DIMENSIONAL
2D	TWO-DIMENSIONAL
ACE	ANGIOTENSIN CONVERTING ENZYME
CRT	CARDIAC RESYNCHRONIZATION THERAPY
DCM	DILATED CARDIOMYOPATHY
DHF	DYSSYNCHRONOUS HEART FAILURE
EC	EXCITATION-CONTRACTION
ECG	ELECTROCARDIOGRAM
HF	HEART FAILURE
LV	LEFT VENTRICLE
RyR	RYANODINE RECEPTOR
SR	SARCOPLASMIC RETICULUM
t-system	TRANSVERSE TUBULAR SYSTEM

ACKNOWLEDGMENTS

I would like to take this opportunity to thank my advisor Dr. Frank Sachse for his support and guidance towards completing my Ph.D. I also thank my committee members, Drs. John Bridge, Ken Spitzer, Robert Hitchcock, and Robert MacLeod, for invaluable advice and lessons in not only experimental preparations but life as well. I thank Dr. Hui Li, Dr. Thomas Seidel, Dr. Natalia Torres, Mr. Eric Carruth, Ms. Chelsea Mitchell, Mr. Robin Moss, Mr. Chris Hunter, Mrs. Jayne Davis, and Mrs. Nancy Allen for all of the technical help and assistance they provided throughout these studies. Thank you to the entirety of the staff and faculty at the Nora Eccles Harrison Cardiovascular Research and Training Institute, not only for technical support, but also for fostering an interest in this field within me. Thank you to Drs. Gordon Tomaselli, David Kass, Andreas Barth, Takeshi Aiba, and Mrs. Deborah DiSilvestre for their help with establishing the DHF/CRT animal model here in Utah. I also thank Dr. Manasa Gudheti and Vutura for their help in obtaining super-resolution images. Financial support was provided by the National Institute of Health, the American Heart Association, and the Nora Eccles Treadwell Foundation.

Finally I would like to thank my father, Mr. Gary Lichter, mother, Mrs. Concetta Lichter, and sister, Ms. Rachel Lichter, for their unwavering support and enthusiasm in my pursuit of science.

CHAPTER 1

INTRODUCTION

1.1 Cardiovascular Disease

Cardiovascular disease is one of the largest problems we face as a society. It is the leading cause of death in developed countries around the world.[1,2] In America, cardiovascular disease was responsible for over 750,000 deaths in 2011 alone.[3] This number is estimated to reach 7.8 million global deaths by the year 2025.[4] Cardiovascular disease encompasses a wide range of pathophysiological conditions ranging from myocardial infarction, coronary artery disease, stroke, and various cardiac myopathies.[2] These conditions are associated with a wide range of symptoms, clinical treatments, and mortality rates.[5] From 2001 to 2011 we have significantly lowered the mortality rate of cardiac diseases by about 31%,[3] however, whether this is due to clinical advancements or overall healthier lifestyle choices in the general population is a topic of debate.[6,7] Nevertheless, there is still much to learn about cardiac disease and how to treat it.

In this work I will focus on HF. This is a general term used to describe any condition in which the heart is unable to pump an adequate blood supply to meet the metabolic demands of the body.[5,8] HF is a degenerative condition that results

from a variety of cardiovascular diseases as time progresses. There are currently over 5 million Americans living with HF and the incidence is approaching 1% for people over the age of 65.[8] When exposed to the abnormal stresses that occur during HF, the heart undergoes structural and functional remodeling, resulting in a deteriorated state.

1.2 Structure and Function of the Heart

Arguably the most important muscle in our body is the heart. On the fundamental level, the heart acts as a pump. By generating a pressure gradient throughout the body, the heart pumps blood through an intricate network of arteries and veins, supplying the body with oxygen for metabolic needs while also removing metabolic waste. The heart accomplishes this function with a very refined structure. From the macroscopic to the microscopic level, the structural makeup of the heart defines its functionality. At the microscopic scale there are a variety of cell types found within the heart. While there are many important cell types, like the cells that make up the blood vessels and the conduction system, the main workhorses are the ventricular myocytes.[9] These cells comprise the majority of volume in the cardiac tissue and are responsible for generating force and producing the contraction of the heart.[10] These cells contain complex machinery responsible for turning electrical signal into mechanical force, a process known as EC coupling.

One crucial element for this coupling is what is known as the t-system or t-tubules. The t-system is a series of membrane invaginations of the cell wall or

sarcolemma.[11] The t-system is associated with many ion channels and proteins involved with EC coupling.[11] Specifically, L-type Ca^{2+} channels and Na^{+}/Ca^{2+} exchangers are found within the t-system membrane.[11] These channels and exchangers allow and facilitate ion flow between the extracellular and intracellular spaces. The structure of the t-system ensures rapid ion flow into the cell interior. The t-system allows for a homogeneous transport of ions across the cell membrane throughout the entirety of the cell interior. If the t-system were not present, transport of extracellular ions to the interior regions of the cell would rely solely on the much slower process of diffusion. Another protein complex closely associated with the t-system is the RyR channel.[11] When Ca^{2+} enters the cell through the L-type Ca^{2+} channels, it interacts with RyR channels located on the membrane of the SR, an intracellular organelle that stores Ca^{2+}, allowing flow of Ca^{2+} ions into the intracellular space.[11] The Ca^{2+} released from the SR comprises the majority of the Ca^{2+} transient within the cell. Once freely diffusing throughout the cell, Ca^{2+} ions bind to the troponin C receptors found within sarcomeres, and the contractile machinery of the cell is switched on.[11] Once contraction is complete, Ca^{2+} is removed from the intracellular space by uptake into the sarcoplasmic reticulum and through the Na^{+}/Ca^{2+} exchangers.[11]

Sarcomeres are the structural component responsible for contraction. They are comprised of a variety of proteins: mainly α-actinin, actin, titin, and myosin.[12] These proteins form an interdigitating structural network allowing close interaction of the myosin filaments with the actin filaments, where the troponin complexes are found and produce the movement required for contraction.[12] For

this movement to produce a contraction, there must be a rigid backbone anchored to the cellular membrane. This backbone structure is known as the Z-disk and is crucial for sarcomere formation as well as maintaining sarcomeric structure and function.[13,14] The main protein found in the Z-disk is α-actinin.[15] Alpha-actinin is an antiparallel homodimer that acts as an anchoring site for titin and actin filaments, while also linking to several transmembrane receptors, regulatory proteins, adherens junctions, focal adhesion sites, and stress fibers.[15,16]

Examining the microstructure of myocytes reveals an anisotropy on many levels. The shape of a ventricular myocyte is inherently anisotropic, resembling a rectangular brick with obvious longitudinal and transverse axes.[10] The arrangement of sarcomeres is anisotropic in that the Z-disks run parallel to the transverse axis of the cell while the actin and myosin filaments run parallel to the longitudinal axis of the cell. This sarcomeric structure is repetitive along the longitudinal axis of the cell. These are not the only form of anisotropic protein distributions found in cardiomyocytes. Many isoforms of the proteins that comprise gap junctions are preferentially distributed to the intercalated disks found at the longitudinal cell ends.[17,18] Gap junctions play a crucial role in the propagation of electrical current. They directly couple the cytoplasmic compartments of connected cells and thus act as diffusion portals for ions and small molecules between cells.[18] Therefore, the anisotropy in their distribution leads to a preferred conduction direction. As individual myocytes join together and create the cardiac tissue, electrical conduction between cells connected

longitudinally results in a fiber orientation that is present throughout the tissue.[19] At the tissue level, electrical propagation moves 3-8 times faster along this fiber orientation than in the transverse direction.[20] At the whole-organ level, the fiber orientation is aligned in a way that, as the cells shorten along their longitudinal axes, the heart contracts in a synchronized motion, resulting in a very efficient pumping of blood from the apex towards the base.[21] The conduction system, wall thickness, and cellular makeup all play a crucial role in ensuring the contraction is as reliable as possible.

1.3 Remodeling of the Heart

The human body is capable of regulating a myriad of physiological processes in order to maintain a stable internal environment.[21] These processes are responsible for a variety of physiological outcomes, from temperature control to body chemistry, and can even trigger protein synthesis and cellular growth.[21] Hypertrophy describes the condition when an organ or tissue becomes enlarged due to an increase in cellular size.[22] In muscles, hypertrophy is often the result of an increased demand placed on the muscle. This process involves subcellular structural changes; in particular, the growth of new sarcomeres in order to accommodate this increased demand.[22,23] In many physiological conditions, this process is reversible.[22]

Similar to other muscles in the body, it is possible for the heart to experience hypertrophy. Hypertrophy is characterized by remodeling of the heart towards an increased wall thickness and physiologically occurs as an adaptive

response to pressure or volume overload.[24] However, in many disease states, hypertrophy results as an initial compensatory response.[24] For instance, after myocardial infarction a loss of contractile tissue places an increased demand on the remaining functional tissue.[25] The hypertrophic response consists of an increase in muscle mass that is thought to reduce wall stress and oxygen consumption.[24] However, although this response can initially be advantageous, over time hypertrophy is deleterious, resulting in decreased cardiac output.[24]

Physiological hypertrophy occurs in pregnant women as well as endurance athletes. In these people it is common to see an enlargement of the heart mass by up to 16% and 20%, respectively.[26,27] Interestingly, in most cases of physiological hypertrophy, the heart is able to return to its natural size after the increased demand is removed, e.g. the baby is delivered.[27] Physiological hypertrophy is thought to be a response to growth factors, while pathological hypertrophy results from stress factors common to cardiovascular disease. The difference in phenotype of physiological versus pathophysiological hypertrophy is also significant. Pathophysiological hypertrophy is often associated with significantly increased deposition of extracellular matrix, i.e. fibrosis, which often results in a worsening condition.[24] At the cellular level, hypertrophied cardiac myocytes exhibit increased cell size and enhanced protein synthesis.[24] This leads to the addition of sarcomeres to the cell, which can occur in parallel or series, resulting in lateral or longitudinal growth, respectively.[24] Pathophysiological hypertrophy is a progressive condition. If diagnosed and treated early and successfully, it can be reversible, similar to physiological

hypertrophy. However, if left untreated, eventually the heart muscle begins to fail. When this happens, the heart remodels into a state known as DCM, characterized by significantly decreased wall thickness and severely reduced cardiac output.[28] It is unclear what exactly causes this transition or why some patients experience a more abrupt transition than others, however, if left untreated, DCM will develop.[28]

As microscopic imaging technology has improved, significant remodeling has been revealed at the cellular and subcellular level of the heart. It has been shown that significant fibrosis of the cardiac tissue occurs during HF, resulting in altered biomechanical properties of the tissue.[29] The distribution of gap junctions has been studied in great detail, including numerous animal models of heart failure. In these models the anisotropic distribution is disturbed as gap junction expression is reduced and protein clusters appear more commonly on the lateral edges of the cell.[17] Remodeling of gap junction protein clusters alone would lead to significant changes in conduction velocity and electrical propagation through the tissue. Numerous studies have revealed significant alterations in the ultrastructure of sarcomeric proteins in animal models of cardiomyopathy.[30-32] Many studies have focused on the arrangement of sarcomeric α-actinin and have reported significant alterations, including down-regulation and loss of physiological structure. Additionally, structural alterations of the t-system and Ca^{2+} regulatory proteins during HF have been described in detail.[33-36] These studies agree that during HF a significant loss of t-system occurs. Due to the importance of the t-system on EC coupling, this specific remodeling is thought to

have significant consequences on Ca^{2+} handling and the ability to generate force.

The study of ionic currents generated by cardiomyocytes has exposed significant alterations in cardiac action potentials associated with HF. For example, it has been shown that during HF, Ca^{2+} transients have decreased amplitudes and increased duration,[37] indicating significant remodeling in the proteins and ion channels involved in EC coupling. In HF, action potential duration is significantly increased in almost all experimental models.[38] This is thought to be a result of a reduction in the repolarizing K^+ currents and an increase in the late Na^+ current.[38] Furthermore, it has been shown that the failing heart is in a significantly altered energetic state. Metabolomics studies have shown that the concentration of adenosine triphosphate is reduced by almost 40% in the failing heart.[39] This happens through a variety of mechanisms, but the result is a switch from fatty acids being the major energy source of the heart to glycolytic metabolism.[39] This has a widely disputed and poorly understood impact on cardiac function.

1.4 Dyssynchronous Heart Failure

HF is a degenerative disease that progresses to worse and worse phenotypes. As the heart adapts to the increased stress associated with HF, the subcellular structural remodeling that occurs often leads to heterogeneous conduction delays, resulting in dyssynchronous propagation of electrical activation within ventricular myocardium.[40] Furthermore, the electrical conduction system of the heart is often damaged, resulting in significant electrical

dyssynchrony between the right and left ventricle. Electrical dyssynchrony leads to mechanical dyssynchrony that further increases stress on the walls of the heart, causing an even larger decline in cardiac output. This disease state is known as DHF and is associated with a poor prognosis. DHF can be detected from the ECG. The hallmark symptom of DHF is an increased QRS duration, which reflects a delay between depolarization of the left and right ventricles of the heart. Increased QRS duration has been shown to be an independent predictor of mortality.[41]

Animal models have shown that DHF is associated with specific remodeling at the cellular and whole-heart levels. Aiba et al. showed a significant increase in action potential duration of ventricular myocytes, along with significant reduction in I_K, I_{K1}, I_{To}, and I_{Ca} current densities.[42] Chakir et al. showed a reduction in β_1 and β_2 adrenergic receptor response due to a decreased gene expression of both receptor subtypes, leading to significantly reduced Ca^{2+} transients.[43] The lateral free wall of the LV is believed to experience higher wall stress and myocyte stretch.[44] Heterogeneity of stress leads to regional remodeling within the LV—specifically, reduced Ca^{2+} transients[42]—and many alterations in genetic expression.[45] Sachse et al. showed that cells isolated from the lateral wall of the LV were partly detubulated.[46] This remodeling was not present in cells isolated from the anterior wall of the LV.[46]

Beyond the listed studies, remarkably little is known about the structural and functional remodeling that occurs on the subcellular scale during DHF. Insight into subcellular proteins involved in excitation contraction coupling would

provide a deeper understanding of the disease state and help shed light onto the mechanisms involved.

1.5 Cardiac Resynchronization Therapy

While drugs like ACE inhibitors, beta-blockers, aldosterone antagonists, and angiotensin receptor blockers are used to help treat overall HF symptoms,[47] the only current method of restoring electrical and mechanical synchrony to the ventricles is through CRT, which is an electrical pacemaker therapy.[48] This is accomplished through a semi-invasive surgery, in which pacemaker electrodes are guided via catheters into the heart using fluoroscopy and other imaging methods. The most common approach to CRT involves placing a sensing electrode in the right atrium in order to detect sinus rhythm and synchronously pace both ventricles. Two electrodes are guided into the ventricles of the heart; one to the apex of the right ventricle while the other is advanced through the coronary sinus until it is in close proximity to the left ventricular wall. Depending on how far the lead is advanced through the coronary sinus, this approach allows pacing of the left lateral, anterior, or septal wall. The pacemaker is used to send stimuli through these electrodes into the left and right ventricles synchronized with atrial activity. Timing of these stimuli can be adjusted to obtain optimal left ventricular outflow.[49] The most efficient electrode placements and pacing protocols have been under debate for many years.[50-52]

CRT has proven to be effective at increasing quality of life and reducing mortality in about 60% of patients.[53] However, the mechanisms by which CRT

improves LV function are still poorly understood. Due to the severity of the problems associated with DHF and HF in general, this therapy was first implemented in humans, and thus the majority of studies performed are clinical trials. While these studies are invaluable and provide tremendous insight into overall mortality and morbidity of various treatments, there is a significant lack of scientific knowledge and the basic understanding of what mechanisms are involved. In the studies mentioned above for DHF[42,43,45,46,54], it was shown that CRT was able to reverse the majority of the remodeling seen in DHF. However, as with DHF, beyond these studies, remarkably little is known about the extent to which CRT is able to reverse the subcellular remodeling that arises from dyssynchrony.

1.6 Focus of This Research

This work aims at building an understanding of remodeling in DHF and restoration after CRT by obtaining insight into the subcellular structure and function. In Chapter 2 I will discuss a novel structural remodeling that occurs in the cellular cytoskeleton. Here we show that the protein comprising the backbone of the sarcomere, α-actinin, exhibits two types of remodeling. One form of remodeling is reversible by CRT while the other is not. In Chapter 3 I describe that detubulation of cells in DHF is heterogeneous and specific to regions near the longitudinal cell ends. This t-system remodeling is associated with an increase in the size of RyR clusters as well as a decrease in spontaneous diastolic Ca^{2+} release events. Finally, Chapter 4 introduces a novel methodology

that is capable of describing subcellular contraction at an unprecedented spatiotemporal resolution, allowing for the detection of heterogeneities in strain generation within myocytes in 2D at the micrometer scale. Together this work has increased our understanding of the subcellular remodeling that occurs during DHF, and sheds new light onto how well CRT is able to reverse structural and functional subcellular remodeling.

CHAPTER 2

REMODELING OF THE SARCOMERIC CYTOSKELETON IN CARDIAC VENTRICULAR MYOCYTES DURING HEART FAILURE AND AFTER CARDIAC RESYNCHRONIZATION THERAPY

Lichter J, Carruth E, Mitchell C, Barth AS, Aiba T, Kass DA, Tomaselli GF, Bridge JH, Sachse FB. Remodeling of the Sarcomeric Cytoskeleton in Cardiac Ventricular Myocytes During Heart Failure and After Cardiac Resynchronization Therapy. *JMCC.* 2014;72:186-95. Reprinted with permission from Elsevier©. No modifications will be permitted.

Journal of Molecular and Cellular Cardiology 72 (2014) 186–195

Contents lists available at ScienceDirect

Journal of Molecular and Cellular Cardiology

journal homepage: www.elsevier.com/locate/yjmcc

Original article

Remodeling of the sarcomeric cytoskeleton in cardiac ventricular myocytes during heart failure and after cardiac resynchronization therapy

Justin G. Lichter [a,b], Eric Carruth [a,b], Chelsea Mitchell [a,b], Andreas S. Barth [c], Takeshi Aiba [c], David A. Kass [c,d], Gordon F. Tomaselli [c], John H. Bridge [a], Frank B. Sachse [a,b,*]

[a] Nora Eccles Harrison Cardiovascular Research and Training Institute, University of Utah, Salt Lake City, UT 84112, USA
[b] Department of Bioengineering, University of Utah, Salt Lake City, UT 84112, USA
[c] Division of Cardiology, Johns Hopkins University School of Medicine, Baltimore, MD 21205, USA
[d] Biomedical Engineering, Johns Hopkins University School of Medicine, Baltimore, MD 21205, USA

ARTICLE INFO

Article history:
Received 11 February 2014
Received in revised form 13 March 2014
Accepted 14 March 2014
Available online 20 March 2014

Keywords:
Heart failure
Cardiac resynchronization therapy
Remodeling
Cardiac recovery
Alpha actinin

ABSTRACT

Sarcomeres are the basic contractile units of cardiac myocytes. Recent studies demonstrated remodeling of sarcomeric proteins in several diseases, including genetic defects and heart failure. Here we investigated remodeling of sarcomeric α-actinin in two models of heart failure, synchronous (SHF) and dyssynchronous heart failure (DHF), as well as a model of cardiac resynchronization therapy (CRT). We applied three-dimensional confocal microscopy and quantitative methods of image analysis to study isolated cells from our animal models. 3D Fourier analysis revealed a decrease of the spatial regularity of the α-actinin distribution in both SHF and DHF versus control cells. The spatial regularity of α-actinin in DHF cells was reduced when compared with SHF cells. The spatial regularity of α-actinin was partially restored after CRT. We found longitudinal depositions of α-actinin in SHF, DHF and CRT cells. These depositions spanned adjacent Z-disks and exhibited a lower density of α-actinin than in the Z-disk. Differences in the occurrence of depositions between the SHF, CRT and DHF models versus control were significant. Also, CRT cells exhibited a higher occurrence of depositions versus SHF, but not DHF cells. Other sarcomeric proteins did not accumulate in the depositions to the same extent as α-actinin. We did not find differences in the expression of α-actinin protein and its encoding gene in our animal models. In summary, our studies indicate that HF is associated with two different types of remodeling of α-actinin and only one of those was reversed after CRT. We suggest that these results can guide us to an understanding of remodeling of structures and function associated with sarcomeres.

1. Introduction

The cytoskeleton is a complex intracellular network of proteins essential for determining the shape and mechanical properties of cells [1]. It also helps to coordinate the function of subcellular proteins in all cell types. These functions range from anchoring cellular organelles such as the Golgi apparatus, nuclei and mitochondria to transmission of extracellular signals and coordinating contraction [1,2]. Cytoskeletal proteins form the sarcomeres, which are the basic contractile units of striated muscle cells. Within each sarcomere is a complex arrangement of proteins [2–4]. Each sarcomere is bounded by the Z-disk [5]. The Z-disk is crucial for maintaining sarcomeric structure and function. The main component of the Z-disk is the protein α-actinin, even though it accounts for less than 20% of Z-disk weight [4]. Alpha-actinin is an anti-parallel homodimer that anchors the actin filaments, which are essential for contraction in myocytes. It was initially believed that α-actinin solely provided an actin binding site [6]. However, subsequent studies demonstrated that α-actinin links to several transmembrane receptors, regulatory proteins, adherens junctions, focal adhesion sites and stress fibers [6]. Further studies revealed that α-actinin plays a pivotal role in the assembly of sarcomeres and the regular arrangement of myofilaments [7,8]. The studies suggest that sarcomere assembly is initiated by small Z-bodies comprising complexes of α-actinin and associated proteins. Subsequently, the Z-bodies expand, fuse and align in Z-bands. Similar as other proteins in the Z-disk α-actinin exhibits a surprisingly dynamic exchange with the cytosolic pool [8]. Exchange rates were larger in Z-bodies than Z-disks indicating that molecular interactions increase the stability of Z-disks. Four different isoforms of α-

* Corresponding author at: Nora Eccles Harrison Cardiovascular Research and Training Institute, University of Utah, Salt Lake City, UT 84112, USA. Tel.: +1 801 587 9514; fax: +1 801 581 3128.
E-mail address: fs@cvrti.utah.edu (F.B. Sachse).

http://dx.doi.org/10.1016/j.yjmcc.2014.03.012
0022-2828/

actinin exist. The genes ACTN-1 and ACTN-4 encode α-actinin isoforms that are expressed in non-muscle cells, where these isoforms of α-actinin contribute to the actin cytoskeleton. ACTN-2 and ACTN-3 encode isoforms specific to the Z-disks of sarcomeres found in striated muscle fibers [4,9–11], with α-actinin-2 being the only cardiac specific isoform [4].

Remodeling of sarcomeric proteins in cardiac disease has been implicated in reduced ventricular function [2]. In particular, it has been suggested that the transition from hypertrophy to heart failure (HF) occurs in two consecutive stages. The first stage is reversible and involves an accumulation of cytoskeletal proteins to counteract the increased strain imposed on the myocardium. The latter stage becomes irreversible and is characterized by a loss of contractile filaments and crucial sarcomeric proteins, including α-actinin, titin, and myomesin. Several cardiac diseases have been associated with remodeling of α-actinin and the Z-disk [9–12]. Melo et al. demonstrated that *Trypanosoma cruzi* in mouse myocytes caused α-actinin distributions to lose their periodic structure and to localize to focal adhesion sites [11]. Hein et al. found depositions of α-actinin-1 in failing myocardium [10], while Oxford et al. showed an accumulation of electron dense material around Z-lines in canines with arrhythmogenic cardiomyopathy. Cardiac disorders have also been linked to mutations in the gene responsible for α-actinin-2, specifically dilated cardiomyopathy [13] and hypertrophic cardiomyopathy [9].

Here we investigated remodeling of α-actinin in two models of HF, synchronous (SHF) and dyssynchronous heart failure (DHF), as well as in a model of cardiac resynchronization therapy (CRT). Approximately 40% of patients suffering from HF develop delays of ventricular electrical activation that result in a dyssynchronous mechanical contraction of the ventricles. The electrical dyssynchrony results in a widened QRS interval, which has been shown to be an independent predictor of mortality and sudden cardiac death [14]. CRT is an established clinical therapy to treat DHF. CRT resynchronizes ventricular mechanical and electrical activity via biventricular pacing and has been proven effective at improving quality of life and reducing mortality in about 55% of patients [15]. A number of studies showed that CRT is associated with restoration of cardiac structure and function, for instance, the transverse tubular system and excitation–contraction coupling [16] as well as the electrophysiological and contractile properties of myocytes [17,18]. However, little is known about the reorganization of sarcomeric structures and associated protein distributions in DHF and CRT.

Our hypothesis is that DHF associated remodeling of sarcomeric organization is reversed after CRT. We used α-actinin as a marker of sarcomeric organization. We applied high-resolution three-dimensional confocal microscopy to image α-actinin distributions in ventricular tissues and cells. Analyses of image stacks allowed us to provide quantitative data on the structural arrangement of α-actinin and its remodeling. Our studies revealed alterations of the spatial regularity of α-actinin. We applied Fourier analysis to characterize remodeling of the spatial arrangement of α-actinin. Also, our studies revealed longitudinal depositions of α-actinin in HF. Using methods of pattern detection we quantified their occurrences. For further insights into the composition of the longitudinal depositions we investigated colocalization of α-actinin with sarcomeric proteins and measured the density of α-actinin based on super-resolution microscopy. To shed light on α-actinin expression in our animal models we performed gene expression analyses and Western blotting.

2. Methods

2.1. Animal model, tissue and isolated cell preparation

All procedures involving the handling of animals were approved by the Animal Care and Use Committees of the Johns Hopkins University and the University of Utah. Protocols complied with the published *Guide for the Use and Care of Laboratory* Animals published by the National Institutes of Health.

The applied animal models have been described previously [16,19–21]. In previous studies, successful implementation of the DHF and CRT models was confirmed by increased and normalized QRS duration, respectively (Table S1) [17]. In brief, adult male mongrel dogs were used as control and models of SHF, DHF and CRT. SHF and DHF animals underwent right atrial pacing for 6 weeks. DHF was caused by left bundle-branch radiofrequency ablation. CRT animals underwent left bundle-branch radiofrequency ablation and 3 weeks of right atrial pacing followed by 3 weeks of biventricular pacing. The pacing rate for SHF, DHF and CRT animals was 180 to 200 bpm. Hemodynamic data were measured at the time of explantation (Table S2).

Lateral and anterior tissue samples from left ventricular subepicardial myocardium were taken shortly after explantation of the heart. Tissue was fixed with paraformaldehyde for confocal imaging or flash frozen in liquid nitrogen for western blot analysis. Cardiac myocytes were isolated enzymatically via retrograde Langendorff perfusion [17]. Myocytes were sampled from the anterior and lateral mid-epi myocardium of the left ventricle.

2.2. Immunohistochemistry

The sarcolemma of isolated myocytes was labeled using wheat germ agglutinin (WGA) conjugated to Alexa Fluor-555 (Invitrogen, Carlsbad, CA, USA). After WGA labeling, cells were fixed and prepared for immunolabeling as previously described [16]. For studies of the subcellular distribution of α-actinin we incubated myocytes with anti-α-actinin (ab9465, clone# EA-53, Abcam, San Francisco, CA) diluted 1:200 in phosphate buffered saline (PBS) solution containing 2% bovine serum albumin, 2% normal goat serum and 0.05% Triton-X 100 overnight at 4 °C. We then applied a secondary goat anti-mouse IgG (H + L) antibody attached to Alexa Fluor-488 (Invitrogen) for confocal microscopy or Alexa Fluor-647 (Invitrogen) for super-resolution imaging. Incubation with either secondary antibody was performed for 1 h at room temperature. For colocalization analyses of α-actinin with proteins of the sarcomeric cytoskeleton we labeled for titin (anti-titin-T12 provided by Dr. Elizabeth Ehler, King's College, London), filamentous actin (A22284, Invitrogen) and heavy chain myosin (ab15, Abcam). Each colocalization study involved staining for α-actinin and one other sarcomeric protein at a time. For dual labeling of α-actinin and titin or heavy chain myosin, we used a polyclonal rabbit anti-sarcomeric α-actinin antibody (ab137346, Abcam) instead of the EA-53 mouse monoclonal antibody. These antibodies were diluted 1:100 and incubated overnight at 4 °C using the same PBS incubation solution as above. The secondary antibodies consisted of either a secondary goat anti-mouse IgG (H + L) antibody attached to Alexa Fluor-488 or 633 (Invitrogen) or goat anti-rabbit IgG (H + L) antibody attached to Alexa Fluor-488 or 633 (Invitrogen). Incubation with either secondary antibody was performed for 1 h at room temperature.

Tissue preparations were fixed in PBS containing 4% paraformaldehyde for 4 h at room temperature. The preparations were immersed in distilled water containing 30% sucrose for 2–3 d. The tissue was then flash-frozen using tissue-freezing medium (Triangle Biomedical Sciences, Durham, North Carolina, USA) at -20 °C and sectioned into 80 μm slices using a Leica CM1850 (Leica Biosystems, Wetzlar, Germany) cryostat. Afterwards tissue sections were stored in PBS, labeled with WGA and for α-actinin as described for isolated myocytes except with the incubation time for the secondary antibody prolonged to overnight at room temperature.

2.3. Confocal imaging and image preprocessing

Imaging was performed using a Zeiss LSM 5 Live Duo (Carl Zeiss, Jena, Germany) confocal microscope equipped with a 63×/1.4 Numerical Aperture oil immersion objective. Tissue sections were imaged with a size

of 1024 × 1024 × ~220 voxels. Voxel sizes were 0.1 μm × 0.1 μm × 0.1 μm. Segments of isolated myocytes from control ($n = 11$), SHF ($n = 7$), DHF ($n = 8$), and CRT ($n = 11$) animals were imaged with a size of 512 × 256 × ~256 voxels with the same resolution. We oriented image stacks so that the longitudinal axis of the cells was parallel to the *y*-axis of the stack (Fig. S1A). Image stacks were cropped to remove empty regions. Afterwards, image stacks were pre-processed for correction of noise, background, attenuation and convolution [16,22,23]. As reported previously, we found that the signal-to-noise ratio of image data decreases significantly with increasing distance from the glass slide [16]. Thus only the first 150 slices (15 μm) of each image stack were used for analysis. We used the α-actinin distribution to identify the cell interior. We dilated the α-actinin signal along the *y*-axis for 6 iterations followed by 10 dilation and erosion steps using a 6-neighbor mask. Subsequent analyses were restricted to the cell interior. The mask of the cell interior was used to calculate a Euclidian distance map. Here, each voxel value represented the distance to the edge of the cell.

2.4. Fourier analysis

Images were transformed into the Fourier domain using the equation:

$$G(u,v,w) = \frac{1}{NMP}\sum_{x=0}^{N-1}\sum_{y=0}^{M-1}\sum_{z=0}^{P-1} g(x,y,z)e^{-2\pi i\left(\frac{xu}{N}+\frac{yv}{M}+\frac{zw}{P}\right)}$$

Here G describes the image in the Fourier domain, while g is the image in the spatial domain. N, M and P are the number of voxels in the *x*-, *y*- and *z*-directions, respectively. We cropped a three-dimensional range in the Fourier domain containing only spatial frequencies 0.4 to 0.66 μm^{-1}. This section was then binned into 10° increments from 0 to 180° with 90° defined along the *y*-axis. A schematic representation of the binning process in 2D is presented in Fig. S1B. The summary intensity in each bin was calculated and normalized across all bins. The resulting histogram provides a measure for the spatial organization and regularity of image components along the specified angles. In Fig. S2 we provide examples for this analysis on four synthetically created images with specified spatial regularity. Fig. S2A represents an image with regular transverse sheets. The patterns in Fig. S2B–D become increasingly more irregular. In particular, Fig. S2D has randomly sized offsets creating a significantly irregular pattern. Fig. S2E shows the results of the Fourier analysis explained above applied to the images.

2.5. Detection of longitudinal depositions

Longitudinal depositions in α-actinin were detected using a series of cross-correlations and thresholding steps (Fig. S3). Cross-correlation was performed in three dimensions using the equation:

$$H(x,y,z) = \sum_{\alpha}\sum_{\beta}\sum_{\gamma} f^*(\alpha,\beta,\gamma)g(x+\alpha,y+\beta,z+\gamma)$$

where H is the resulting image, f^* is the complex conjugate of a Gaussian function f and g is the original image. The Gaussian function was defined as:

$$f(x,y,z) = e^{-\left(\frac{x^2}{2\sigma_x^2}+\frac{y^2}{2\sigma_y^2}\right)}$$

with the parameters σ_x and σ_y. We used two separate functions to extract longitudinal (along *y*-axis) and transversal components (along *x*-axis) in the image. The function for extracting longitudinal components had a σ_x of 0.1 μm and a σ_y of 1 μm. The function for extracting transversal components used a σ_x of 1 μm and a σ_y of 0.1 μm. The resulting functions were discretized into matrices with dimensions of 17, 17, and 1 in *x*-, *y*- and *z*-direction, respectively. Each matrix was correlated separately with the pre-processed image data yielding two image stacks: one with enhanced transversally oriented features (I_{TRANS}) and one with enhanced longitudinally oriented features (I_{LONG}). Three separate conditions were tested to identify longitudinal depositions. First, local extrema in the I_{LONG} image were detected that satisfied the following equation:

$$I_{LONG}(x,y,z) \geq MODE_{TRANS} + STD_{TRANS}$$

where $I_{LONG}(x,y,z)$ is the voxel value at the point (x,y,z) in the I_{LONG} image stack, $MODE_{TRANS}$ and STD_{TRANS} are the mode and standard deviation of the I_{TRANS} image stack, respectively. Points were then checked to satisfy the following two equations:

$$I_{LONG}(x,y,z) > I_{TRANS}(x,y,z) + STD_{TRANS}$$

$$I_{PRE}(x,y,z) > MODE_{PRE} + STD_{PRE}$$

where $I_{TRANS}(x,y,z)$ is the voxel value at the point (x,y,z) in the I_{TRANS} image stack and $I_{PRE}(x,y,z)$ is the voxel value at (x,y,z) in the pre-processed α-actinin image stack. $MODE_{PRE}$ and STD_{PRE} are the mode and standard deviation of the pre-processed image stack, respectively.

2.6. Super-resolution imaging

Super-resolution imaging of isolated cardiomyocytes was performed with a Vutara SR 200 (Vutara, Inc., Salt Lake City, UT). The imaging is based on fluorescence photoactivation localization microscopy (FPALM) [24,25]. Cells labeled for α-actinin with Alexa Fluor-647 (Invitrogen) were immersed in photoswitching buffer. The buffer comprised of 50 mM cysteamine and oxygen scavengers (glucose oxidase and catalase) in 50 mM Tris + 10 mM buffer at pH 8.0. Fluorescence was achieved using a 647 nm excitation laser and a 405 nm activation laser. Images were recorded using a 60×/1.2 NA water immersion objective. Image resolution was 20 nm in the *xy* plane and 50 nm in *z*-direction. A confidence value for each point was calculated as the geometric mean of the photon count and *z*-offset for that particular point.

To analyze these data, 16 spherical regions were visually selected in both transverse sheets and longitudinal depositions from a total of 4 SHF cells. These regions had a radius of 75 nm. The number of detected molecules (confidence > 0.8) within that sphere was calculated for each region.

2.7. Colocalization of α-actinin with sarcomeric proteins

Isolated myocytes labeled for α-actinin and an additional sarcomeric protein were studied using confocal microscopy as described above. Two-dimensional images with an isotropic resolution of 0.1 μm were acquired. Colocalization of α-actinin with titin, actin or myosin was measured using Pearson's correlation coefficient:

$$R_p = \frac{\sum_i\left(S_{1,i}-\overline{S_1}\right)\left(S_{2,i}-\overline{S_2}\right)}{\sqrt{\sum_i\left(S_{1,i}-\overline{S_1}\right)^2\sum_i\left(S_{2,i}-\overline{S_2}\right)^2}}$$

with the image of α-actinin, S_1, the image of a sarcomeric protein, S_2, and the mean image intensity, $\overline{S_1}$ and $\overline{S_2}$, respectively. Pearson's correlation coefficient ranges between −1 and 1. A value of 1 implies an increasing linear relationship of pixel intensities in the measured images. A value of 0 indicates that pixel intensities are not linearly related. A value of -1 indicates a decreasing linear relationship. Colocalization was determined within entire imaged cell segments ($n = 4$ for all models), in sarcomeres with and without longitudinal depositions of α-actinin (titin: $n = 14$, actin: $n = 13$, myosin: $n = 6$) using Fiji with the Coloc 2 plugin [26].

2.8. Gene expression analysis

Gene expression data were retrieved from the Gene Expression Omnibus (GEO) database [27] (GSE14327 [1-color design data] and GSE14338 [2-color design data]). In previous work we generated these data from left ventricular subendocardial myocardium of 11 control, 10 DHF and 9 CRT canine models [28]. In brief, total RNA was isolated with TRIzol reagent (Invitrogen) from the sub-endocardium of the anterior and lateral left ventricular walls. Following a 1-color design, RNA from the anterior and lateral left ventricular myocardium was labeled with Cy3 and hybridized onto 2 separate Agilent 44 K canine-specific microarrays. Studies were repeated in a subset of animals (6 control, 5 DHF, and 5 CRT canine) using a 2-color design. Corresponding anterior and lateral samples from the same heart were labeled with Cy3 and Cy5 and hybridized onto the same microarray to achieve a direct comparison of the relative gene expression in different regions of the same heart. ACTN2 and pro-atrial natriuretic factor (NPPA) were each represented on the microarray by a single specific oligonucleotide. In subsequent studies, we compared the DHF and CRT data to publicly available datasets of fetal and adult human myocardium (GEO accession numbers GSE2051, 2061, 2062). Unpaired 2-class significance analysis of microarrays was used to determine differences in gene expression and correct for multiple testing [29]. Differences in gene expression were regarded as statistically significant if a false discovery rate of $q < 0.05$ was achieved. Functional annotation of differentially expressed genes was based on the Kyoto Encyclopedia of Genes and Genomes (KEGG) pathways database [30] as previously described [28,31].

2.9. Western blotting

Tissue samples were collected from the isolated heart, flash frozen in liquid nitrogen and stored at −80 °C. Samples were homogenized in 0.5 ml of NP40 Cell Lysis Buffer (Invitrogen) containing protease inhibitor cocktail (Sigma-Aldrich, St. Louis, Missouri) for 10 min or until the lysate flowed freely. A protein assay was performed using a Protein Assay Kit (Pierce, Rockford, Illinois). Samples were heated at 70 °C for 10 min and then 10 μg of protein was loaded in each well of a 4–15% polyacrylamide 26 well Criterion TGX Precast Gel (Bio-Rad, Hercules, California, USA) with a standard ladder (Bio-Rad). The gel was electrophoresed for 2 h at 85 V. Samples were transferred to 0.2 μm nitrocellulose at 50 V for 45 min. The blot was incubated in a blocking solution comprised of 0.01 M Tris–HCl, 0.15 M NaCl, 0.05% Tween-20 (TBS-T) with 5% skim milk powder overnight on a shaker platform at 4 °C. Incubation with primary antibodies was performed in blocking solution containing the two primary antibodies: mouse monoclonal to sarcomeric α-actinin at 1:10,000 (Abcam) and mouse monoclonal to GAPDH at 1:10,000 (Abcam) for 2 h at room temperature. The blot was next incubated in goat polyclonal secondary antibody to mouse IgG1 heavy chain conjugated with horseradish peroxidase at 1:20,000 (Abcam) and Streptactin-HRP Conjugate at 1:20,000 (Bio-Rad) in TBS-T for 1 h on a shaking platform at room temperature. The blot was washed several times before addition of Amersham ECL Prime Western Blotting Detection Reagents (GE Healthcare, Waukesha, Wisconsin, USA) and imaged using a ChemiDoc XRS + System (Bio-Rad).

Quantitative analysis was performed using Image Lab Software 4.0.1 (Bio-Rad) to obtain intensities for α-actinin and GAPDH for each lane. Normalization was performed for each lane by dividing the α-actinin signal intensity by the respective GAPDH intensity.

2.10. Statistical analysis

All results are listed and displayed as mean ± standard error. All statistical analyses were performed in Matlab R2012b (The Mathworks Inc., Natick, MA, USA). Significance was established using a one-way analysis of variables (ANOVA) followed by a post-hoc Tukey–Kramer t-test. Only differences with a p-value less than 0.05 were considered significant. Significant differences in bar graphs were marked by brackets.

3. Results

3.1. Distribution of α-actinin in normal and heart failure tissue

We imaged sections from control canine cardiac ventricular tissue. A pre-processed 3D confocal microscopic image stack is shown in Fig. 1A. Pre-processing consisted of deconvolution, background removal and attenuation correction. The corresponding unprocessed image stack is presented in Fig. S4A. In these images, α-actinin was primarily arranged in regular, parallel, transverse sheets. These sheets ran laterally and exhibited frequent gaps and extended throughout the myocytes. This pattern is consistent with previous descriptions of α-actinin arrangement in striated muscle [3,4,6]. Fig. 1B shows a 3D reconstruction of the α-actinin signal. Here the sheet-like structure and repetitive nature of α-actinin are more apparent. We also found that where sheets were interrupted, the gaps were commonly filled with WGA signal (Fig. 1C). This illustrates that the transverse tubular system is closely associated with the α-actinin sheets.

The pre-processed XY images of tissue from SHF, DHF and CRT animals are presented in Fig. 1D, E and F, respectively. The corresponding unprocessed image stacks are presented in Fig. S4B, C and D, respectively. It is clear that the α-actinin distribution in these animals was remodeled versus control. The overall spatial regularity of the α-actinin signal reduced. Furthermore, visual inspection of these images revealed longitudinal depositions of α-actinin spanning and connecting adjacent parallel sheets of α-actinin. While the decrease in spatial regularity is most noticeable in DHF, the = longitudinal depositions are visible in all three models of HF. Examples for three-dimensional structure of the α-actinin distribution from SHF, DHF and CRT are presented in the expanded 3D views of G, H and I respectively. The 3D reconstructions depict that while transversal α-actinin sheets extended throughout the cell depth (z-direction), the longitudinal depositions only extended 1–2 μm in the z-direction.

3.2. Distribution of α-actinin in isolated myocytes

Subsequently, we imaged isolated cells using the same methods as described above for imaging of tissue. Fig. 2 represents an isolated myocyte from an SHF animal labeled for α-actinin and with WGA. The patterns of α-actinin were consistent with those previously observed in tissue indicating that the α-actinin structure was not affected by the cell isolation procedure. We found transverse sheets running regularly throughout the entirety of the cell as well as the longitudinal depositions spanning and connecting adjacent transverse sheets. Furthermore, we noticed thick areas of α-actinin around the longitudinal and lateral edges of the cell.

We acquired 45, 53, 34 and 49 image stacks from segments of control, SHF, DHF and CRT cells, respectively. Fig. 3A–D shows representative 3D pre-processed image stacks for these experimental groups. The corresponding unprocessed image stacks are presented in Fig. S5. The arrangement of α-actinin in these image stacks was similar to that in fixed tissue. In control cells (Fig. 3A) the α-actinin distribution maintained a regular parallel, transversely running, sheet-like pattern. We visually inspected this pattern in cells from our models of SHF, DHF and CRT (Fig. 3B–D) and found a decreased spatial regularity in DHF. Here, α-actinin sheets were broken down into smaller segments with vertical offsets being more common. In the models of SHF, DHF and CRT we found longitudinal depositions of α-actinin similar to those observed in tissue. These longitudinal depositions were most noticeable in the exemplary CRT cell (Fig. 3D). To illustrate differences between cells with a low occurrence of depositions and cells with a high occurrence of depositions, we created 3D reconstructions of the

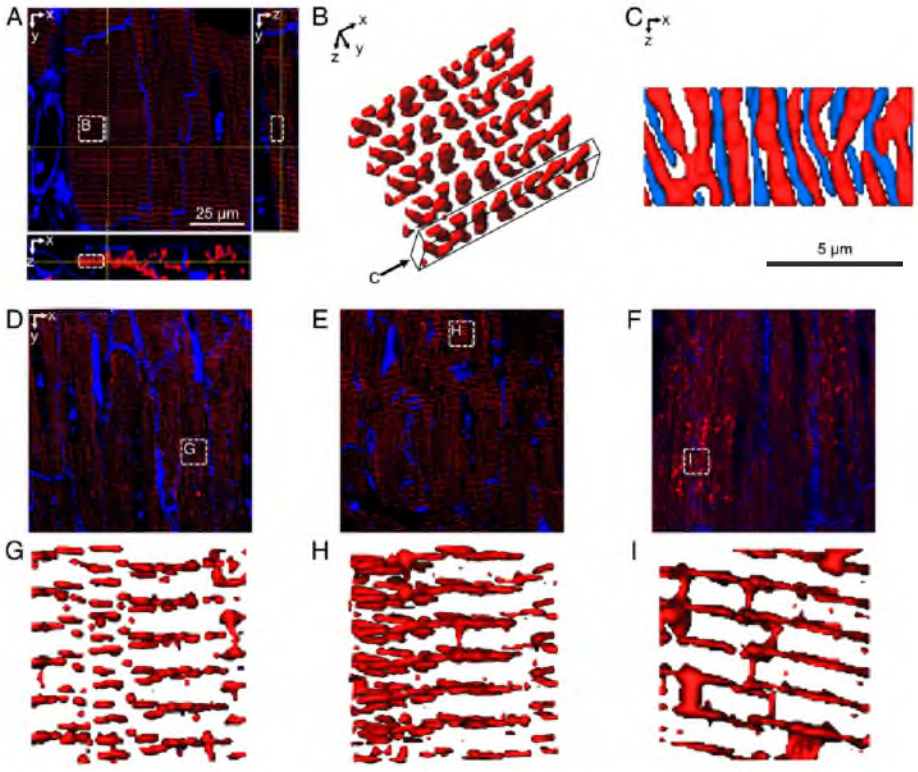

Fig. 1. Pre-processed 3D stacks of tissue labeled with WGA (blue) and for α-actinin (red). (A) Sections through stack acquired from control tissue. The yellow lines indicate the presented cross sections. (B) 3D reconstruction of α-actinin distribution marked with box in (A). (C) 3D reconstruction of α-actinin and t-system labeled with WGA in the transverse sheet marked in (B). Pre-processed 2D XY slices of (D) SHF, (E) DHF and (F) CRT tissue sections. Images reveal frequent longitudinal depositions of α-actinin. (G–I) 3D reconstructions from regions marked in (D–F), respectively. The reconstructions indicate fragmentation and decreased spatial regularity of α-actinin sheets. Bar in (A) applies to (D–F).

α-actinin distribution in control and CRT animals (Fig. 3E and F, respectively).

3.3. Spatial regularity of α-actinin distributions

We applied Fourier analysis to quantify spatial regularity of the α-actinin distribution in isolated myocytes (Fig. 4A and B). We focused on the intensity occurring along the 0° and 90° angles. In the transverse direction (0 ± 5°) the averaged intensity in DHF cells was significantly lower than that in all other animal models (Fig. 4A). Here, decreases in intensity signify that the α-actinin sheets running transversely through the cells were irregular. Examples for irregular distributions are presented in Fig. S2. The examples show an increase in intensity along the transverse direction (0 ± 5°) when the hyphenations are regular (Fig. S2B). However when the offsets are random and without regular pattern, we find a low intensity (Fig. S2D). We did not find significant differences between the control, SHF and CRT groups indicating that CRT restored the α-actinin distribution to a more regular structure after DHF.

Our study revealed significant differences between control and DHF regarding the regularity of α-actinin sheets in the longitudinal direction (90 ± 5°). Here, control cells were different from DHF and SHF cells (Fig. 4B). CRT cells were not different versus control, again indicating that the regularity was partially restored after CRT. The full 180° intensity histogram is presented in Fig. S6. We found further differences between combinations of the control, CRT and DHF animal models along

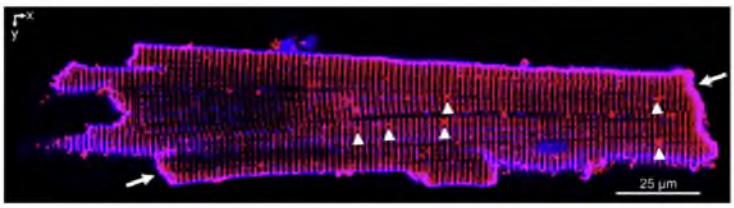

Fig. 2. XY cross section from a 3D image stack of an isolated ventricular myocyte from SHF model. The cell was labeled with WGA (blue) and for α-actinin (red). Arrows point to wide areas of strong α-actinin signal along the cell ends. Triangles point to longitudinal depositions.

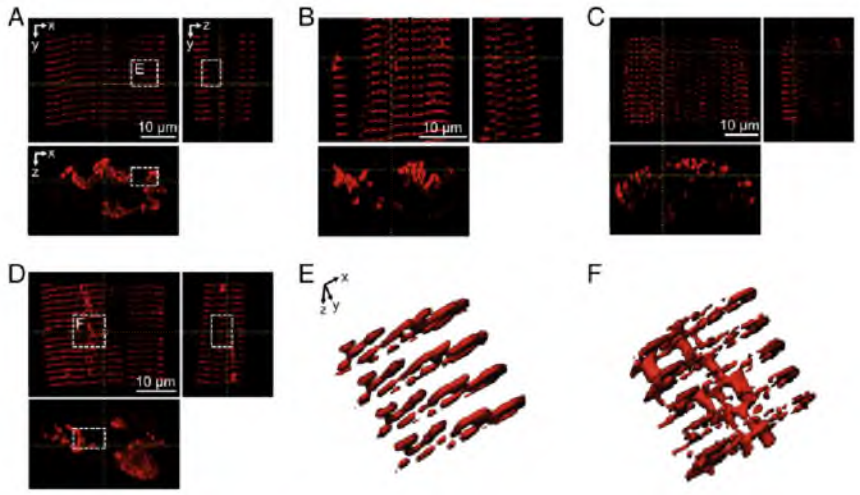

Fig. 3. Pre-processed 3D image stacks of sections of isolated cardiac myocytes from (A) control, (B) SHF, (C) DHF, and (D) CRT animals. Sections were labeled for α-actinin. (E, F) 3D reconstructions of the segments marked in (A, D).

other angles ($20 \pm 5°$, $30 \pm 5°$, $140 \pm 5°$, $150 \pm 5°$ and $160 \pm 5°$). However, the intensities along those angles were mostly small and the differences negligible. Exceptions include the differences between control and DHF at $110 \pm 5°$ and $120 \pm 5°$.

3.4. Longitudinal depositions of α-actinin

Using the algorithm introduced in Section 2.5, we detected the longitudinal depositions in isolated cells. We calculated the occurrence of

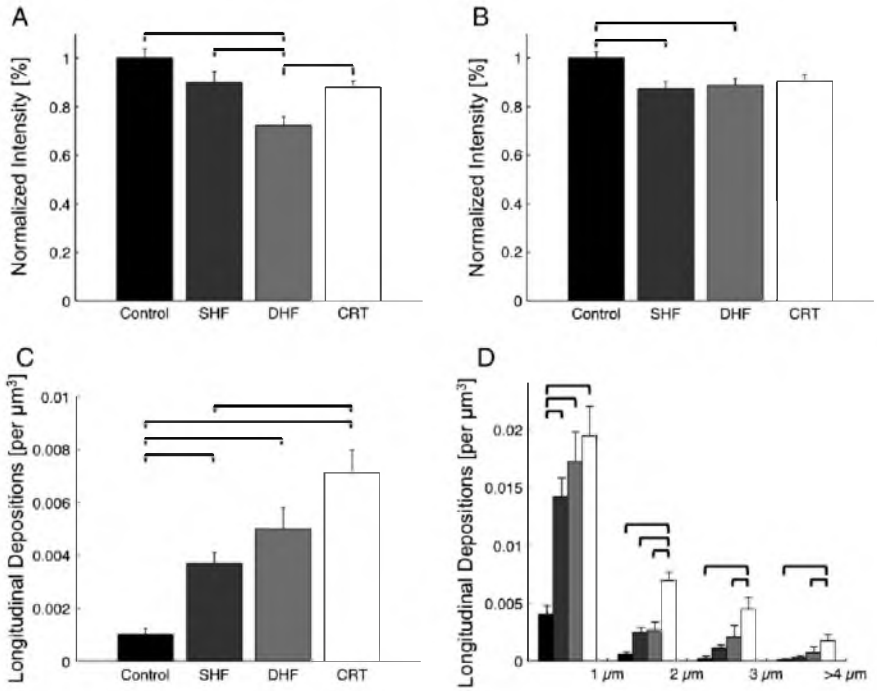

Fig. 4. Quantitative analyses of α-actinin distributions in control, SHF, DHF, and CRT cells. (A) Fourier analysis of image intensities in the transverse direction ($0 \pm 5°$). (B) Fourier analysis of image intensities in the longitudinal direction ($90 \pm 5°$). (C) Average occurrence of longitudinal depositions. (D) Occurrences of longitudinal depositions for each experimental group as a function of the distance from the cell surface.

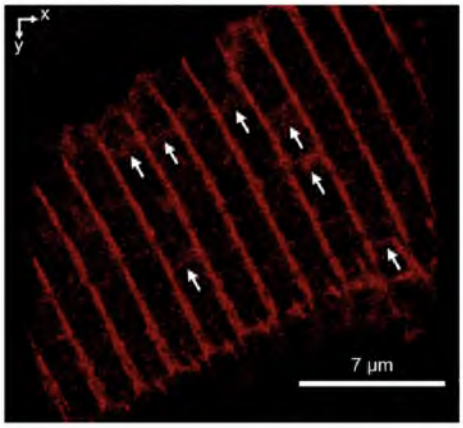

Fig. 5. Three-dimensional image of α-actinin detections from super-resolution microscopy of an isolated cardiac myocyte from SHF model. The field of view is ~22 × 23 × 8 µm. Arrows point to longitudinal depositions spanning between transverse sheets in the cell interior.

these depositions using the volume of the cell (Fig. 4C). The occurrence of longitudinal components was larger in both models of HF versus control. Furthermore, CRT cells had a higher occurrence versus control and SHF. We further analyzed this remodeling to examine if it was localized to a specific area of the left ventricle. Fig. S7 compares the occurrence of these longitudinal depositions in cells from the lateral and anterior left ventricle. We did not find a significant difference between these areas in any of the animal models.

Further analysis allowed us to provide insights into the intracellular distribution of longitudinal depositions. Using the distance map calculated from the intracellular mask, we measured the distance of each detected longitudinal deposition from the edge of the cell (Fig. 4D). In all animal models the majority of depositions were within 1 µm of the cell edge. Here, control cells exhibited a smaller number of depositions versus SHF, DHF and CRT. At larger distances a persistent pattern appeared in the densities of these longitudinal depositions in the different animal models. At all distances control cells displayed the lowest occurrence of depositions, followed by SHF, DHF and then CRT.

3.5. Molecular density of longitudinal depositions

We used super-resolution microscopy to further characterize and quantify the longitudinal depositions that we found. A representative 3D reconstruction (Fig. 5) reveals similar features to those obtained with confocal microscopy, i.e. transverse sheets and longitudinal depositions of α-actinin. Since each point in these images represents a single detection, super-resolution microscopy allowed us to quantify the number of fluorophores present in different regions of the cell. We compared the number of detections in volumes centered at the transverse sheets versus longitudinal depositions. Longitudinal depositions were significantly less dense in detections than regions of the transverse sheets (1.0 ± 0.11 vs 0.49 ± 0.07, normalized to the number of detections in the transverse sheets).

3.6. Remodeling of sarcomeric proteins

To shed light on remodeling of the sarcomeres we examined three additional cytoskeletal proteins. We investigated if these proteins undergo spatial remodeling as described above for α-actinin. Fig S8 shows exemplary images of titin, actin and myosin with α-actinin as well as intensity profiles through longitudinal depositions in CRT cells. The images indicate that the organization of titin, actin and myosin in a sarcomere in relationship to α-actinin is not altered. We applied Pearson's correlation coefficient to investigate if the cytoskeletal proteins accumulate in longitudinal depositions similar as described above for α-actinin (Fig. 6). Colocalization of titin with α-actinin was reduced in sarcomeres with longitudinal depositions versus sarcomeres without longitudinal depositions. This indicates that titin is not a major component in these depositions. Colocalization of actin and myosin with α-actinin was not different in sarcomeres with and without depositions. Inspection of intensity profiles (Fig. S8G, H, K, and L) suggests that these proteins are present in the depositions, but are not accumulated as α-actinin is.

3.7. Analyses of gene expression

Analysis of ACTN2 expression did not show significant transcriptional differences between control, DHF, and CRT animals in either anterior or lateral left ventricular myocardium (Fig S9). However, regional changes in ACTN2 expression were suggested by a significantly larger ratio of ACTN2 expression between the anterior and lateral left ventricles in DHF animals compared to controls. Importantly, the anterior-to-lateral ACTN2 ratio was restored to control levels by CRT (Fig. 7A).

Besides upregulation of natriuretic peptides, dysregulation of sarcomeric genes, including alpha- and beta-myosin heavy chain isoforms, is regarded as a hallmark of the fetal gene expression program, which is characteristic of HF. In our study, we found a negative correlation for the anterior-to-lateral ratios of ACTN2 and NPPA (natriuretic peptide A; coefficient of determination R^2: 0.559; Fig. 7B). Of note, the similarities between the fetal gene expression program and our animal model of dyssynchronous and resynchronized HF extended beyond selected marker genes. When we examined expression of 160 KEGG pathways, we found a highly coordinated regulation of metabolic and signaling

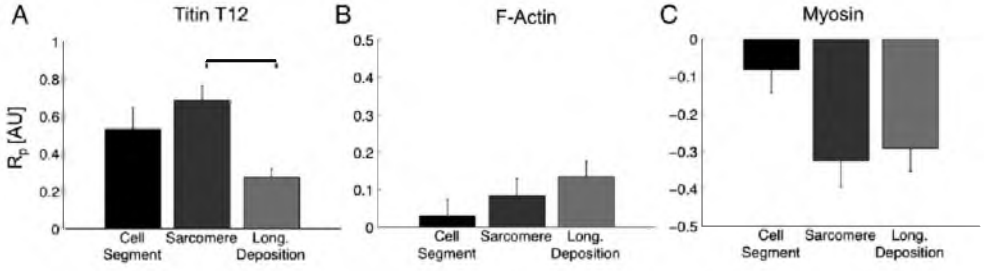

Fig. 6. Colocalizaton analysis of α-actinin with titin (A), actin (B) and myosin (C). Pearson correlation coefficients R_p were calculated for entire cell segments, regions of interest centered on sarcomeres without longitudinal depositions, and regions centered on sarcomeres with longitudinal depositions. Co-localization of α-actinin in sarcomeres and regions with longitudinal depositions was significantly reduced for titin only. For actin and myosin, differences of colocalization were not significant.

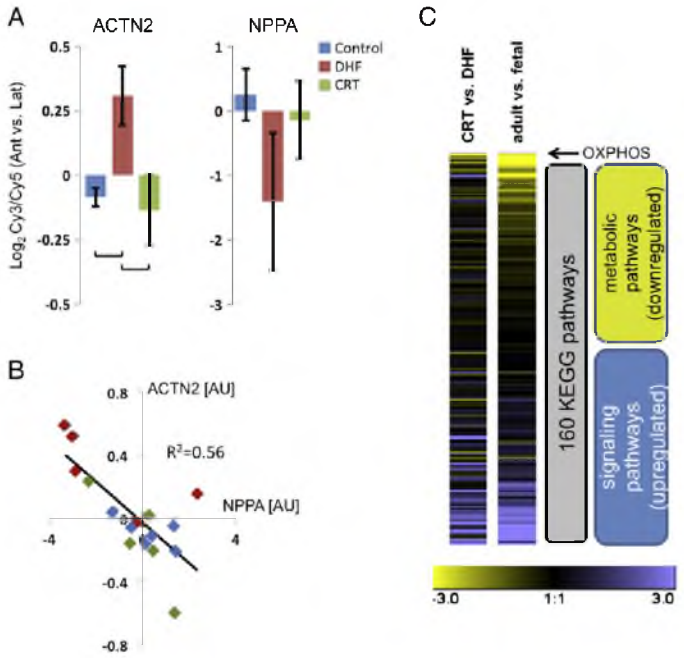

Fig. 7. Gene expression analysis using a two-color microarray and labeling with Cy3 and Cy5. (A) The ratio of ACTN2 gene expression in Ant versus Lat samples is significantly higher in DHF than in control or CRT samples. Differences of NPPA ratios were not significant. (B) The ratio of ACTN2 expression in Ant and Lat samples is negatively correlated to the NPPA ratio. (C) Analysis of KEGG pathways in DHF versus CRT myocardium indicates a similar regulation of pathways as in fetal versus adult myocardium re-expression. The net expression of a KEGG pathway (number of upregulated minus downregulated genes within a study in relation to total number of genes per given KEGG pathway) is color-coded with yellow and blue, representing decreased and increased expression of the pathway genes, respectively. The net expression of the different pathways is depicted vertically and sorted according to their similarity of gene expression of the pathway "oxidative phosphorylation" (OXPHOS).

pathways. Regulation of pathways in CRT versus DHF was similar to the regulation in human adult versus fetal myocardium (Fig. 7C). In general, metabolic and cell signaling pathways in CRT versus DHF were downregulated and upregulated, respectively.

3.8. Western blot results

Based on our analyses of confocal and super-resolution microscopic images, we hypothesized that cells with longitudinal depositions have an up-regulation of α-actinin. To test this hypothesis we measured the expression of α-actinin in tissues from control and CRT animals since they represent the extreme cases of the occurrence of depositions (Fig. 4C and D). Fig. S10 shows a representative western blot stained for α-actinin and GAPDH. Differences between the averaged and normalized α-actinin to GAPDH signal ratios in control and CRT animals were not significant (1.0 ± 0.08 vs 1.08 ± 0.11, normalized to the control ratio).

4. Discussion

Our study used three-dimensional microscopy and image analyses to reveal previously unknown remodeling of sarcomeres in cardiac ventricular myocytes from failing hearts. Visual inspection of images exposed remodeling associated with HF, in particular the irregular arrangement and occurrence of longitudinal depositions of α-actinin. We applied Fourier analysis to measure the decrease of spatial regularity of the α-actinin distribution. In DHF cells, we found decreased regularity of α-actinin sheets. Along the transverse direction, regularity was increased after CRT. In the longitudinal direction, the regularity of the α-actinin distribution was similar in CRT and control cells, while regularity in DHF was lower compared to control. These results support our hypothesis that DHF associated remodeling of sarcomeric organization is partly reversed after CRT. However, our studies also revealed longitudinal depositions of α-actinin in the applied HF models and after CRT. The depositions spanned between adjacent transverse sheets and their density was approximately half of that found in the transverse sheets. We found an increased occurrence of these depositions after CRT versus SHF. However, the difference between DHF and CRT was not significant. We also examined colocalization of proteins of the sarcomeric cytoskeleton with the longitudinal depositions. We found that these proteins do not accumulate in the depositions indicating that their major contributor is α-actinin.

In summary, our study revealed two types of structural remodeling: One identified by reduced regularity of the α-actinin distribution in DHF and normalized regularity after CRT and the other by the increased occurrence of longitudinal depositions in DHF and CRT. In previous work it has been established that DHF is associated with an increased QRS duration and CRT restores QRS duration to similar values as in control (Table S1). Furthermore, comparative gene expression analyses indicated reversion of the fetal gene program in DHF by CRT. Thus, our study suggests that decreased spatial regularity is correlated to prolonged QRS duration and activation of the fetal gene program.

Sarcomeric remodeling has been found in other forms of heart failure. Studies in a canine model elucidated ultrastructural changes in sarcomeric arrangement during arrhythmogenic right ventricular cardiomyopathy [12]. The structural changes were associated with left bundle branch block, which is the basis for our DHF model. However, the fundamental mechanisms underlying block in this disease model are very different to the cause of block in our DHF model, which produced by left bundle branch ablation. Using electron microscopy, the study found an accumulation of electron dense material around the Z-

disk that extended in various directions and filled the entire area of the sarcomere. In this study [12], changes in α-actinin expression were not detected by western blot, which is consistent with our study. The study compared the finding of "Z band streaming" to a human skeletal muscle disease known as nemaline myopathy. Differences between our results, the accumulation of electron dense material in arrhythmogenic right ventricular cardiomyopathy and the ultrastructural phenotypes of nemaline myopathy include the extent and local features of remodeling [12,32,33]. In our study, the degree of disorganization of the Z-disk and local remodeling appears smaller. Nevertheless, the longitudinal depositions could be a special case of Z-band streaming with remodeling of α-actinin restricted to single sarcomeres.

It has also been shown that the Z-disk becomes altered in culture and during diseases other than heart failure. Cultured adult rat cardiomyocytes completely lose striation of α-actinin between 4 and 7 days [34]. In mouse cardiomyocytes, after 72 h of infection with the parasite *T. cruzi*, the overall expression of α-actinin decreased by 32% [11]. Furthermore α-actinin completely lost its periodic arrangement and became localized to focal adhesion sites [11]. A genetic study on hypertrophic cardiomyopathy (HCM) in humans showed that all affected family members had a G to A missense mutation in exon 3 of *ACTN2*. Additionally, 3 further mutations in highly conserved regions of *ACTN2* were found in affected individuals. In this study, 4 of these mutations were identified as causes of HCM, supporting the notion that disruption of Z-disk proteins can lead to heart disease [9,35].

Hein et al. suggested that sarcomeric remodeling during HF occurs in two main stages, an early reversible stage characterized by the accumulation of cytoskeletal proteins to offset the increased strain imposed on the myocardium, and a latter irreversible stage defined by the loss of contractile filaments [2]. We suggest that the remodeling seen here is part of the primary stage when the myocytes are still compensating for the increased strain that arises in HF.

A recent study reported significant reductions in the amount of sarcomere shortening in isolated cells from SHF and DHF animals [18]. The study also showed a decrease of about 40% in the strain magnitude of the anterior-septal and lateral walls in these models versus control [18]. Furthermore, it has been suggested that disorganization of sarcomeres leads to changes of contractility [36]. Thus, the sarcomeric remodeling observed in our study can help explain reduced sarcomere shortening in HF. Also, we suggest that the increase of sarcomere shortening in isolated CRT cells reported in [18] can be explained in part by restoration of sarcomere organization revealed in our studies. It is difficult to separate effects of sarcomere organization on contractility from other remodeling processes in HF and after CRT. Nevertheless, we suggest that remodeling of sarcomere organization plays a complementary role. Also, our studies indicate that longitudinal depositions have only a minor effect on passive mechanical properties and contractility of myocytes. We observed the highest occurrence of longitudinal depositions in CRT cells, which nevertheless have similar contractile properties as control cells.

We performed gene and protein expression analyses to test the hypothesis that the depositions are caused by upregulation of α-actinin. Our analyses rejected this hypothesis. Differences of ACTN2 and α-actinin-2 expression between CRT and control myocardium were not significant. However, the occurrence of depositions was increased in CRT versus control myocytes. We propose two mechanisms to explain why CRT cells exhibited the highest occurrence of longitudinal depositions of α-actinin. In our model of CRT the heart undergoes 3 weeks of DHF followed by 3 weeks of biventricular pacing. It is probable that the heart is experiencing new stressors after initiation of CRT. Therefore, depending on the timescale of the remodeling, our studies could be at the time of peak occurrence of these longitudinal depositions. The second mechanism is that the decreased sarcomere organization in DHF makes the cells more prone to creating longitudinal depositions when synchrony is restored by CRT. Both explanations point at a potential role of longitudinal depositions as a marker of previous and ongoing remodeling at the subcellular scale. We speculate that increased numbers of longitudinal depositions indicate that remodeling processes are initiated.

4.1. Limitations

Rapid pacing is widely used for animal models of non-ischemic HF. The models recapitulate major electrophysiological (action potential prolongation, high incidence of sudden cardiac death, atrial arrhythmias), morphological (ventricular hypertrophy), functional (depressed contractility) and genomic (re-expression of a fetal gene expression pattern) hallmarks of human HF. However, the models do not mimic all aspects of the complex clinical spectrum of congestive HF in patients. The changes in myocardial structure occurring with tachypacing may be dissimilar to clinical forms of HF due to chronic ischemia or hypertensive disease, which usually develop over a longer period of time. Thus, extrapolation of the findings from our HF models to clinical forms of HF requires caution. Also, our CRT model is based on only 3 weeks of biventricular pacing. While studies indicated that 3 weeks of CRT restored some structural and functional properties of the heart [16,17,19], other properties, for instance, hemodynamic properties were not restored (Table S2). Membrane capacitance of isolated myocytes, which is a marker of their size, is increased after CRT versus control myocytes indicating persistent cellular hypertrophy after 3 weeks of CRT [17]. Our study suggests that CRT leads to partial restoration of sarcomeric organization. It is possible that the time scale of restoration of sarcomeric organization is longer than the given 3 weeks. The focus of our study was on characterization of sarcomeric α-actinin. We applied a monoclonal antibody for sarcomeric α-actinin. Similar antibodies have been characterized in previous studies [10,37]. The antibody labels α-actinin 2 and 3, but not α-actinin 1 or 4. We did not find labeling of blood vessels in our images from tissue slices conforming that the antibody does not label smooth muscle α-actinin 1.

In summary, our study provides unique quantitative insights into remodeling of sarcomeric protein organization based on three-dimensional high-resolution confocal microscopy. We introduced new methods to characterize subcellular remodeling in HF and after CRT. The findings of this study will guide us towards developing studies to elucidate the mechanisms and effects of subcellular remodeling in cardiac disease and restoration after therapy.

Disclosures

Dr. Kass has served as a consultant to or on the advisory board of Boston Scientific Consulting. The other authors report no conflicts.

Acknowledgments

Sources of funding: The study has been supported by NIH grants R01 HL094464 (FBS) and PO1 HL077180 (DAK, GFT), and awards from the Nora Eccles Treadwell Foundation (JHB, FBS).

We thank Chris Hunter, Dr. Hui Li and Dr. Natalia Torres for their help and discussions. We also thank Dr. Manasa Gudheti (Vutara, Inc, USA) for her advice on the super-resolution microscopy studies. The titin antibody was a kind gift of Dr. Elisabeth Ehler, King's College, London, UK.

Appendix A. Supplementary data

Supplementary data to this article can be found online at http://dx.doi.org/10.1016/j.yjmcc.2014.03.012.

References

[1] Fletcher DA, Mullins RD. Cell mechanics and the cytoskeleton. Nature 2010;463:485–92.

[2] Hein S, Kostin S, Heling A, Maeno Y, Schaper J. The role of the cytoskeleton in heart failure. Cardiovasc Res 2000;45:273–8.
[3] Papa I, Astier C, Kwiatek O, Raynaud F, Bonnal C, Lebart MC, et al. Alpha actinin-CapZ, an anchoring complex for thin filaments in Z-line. J Muscle Res Cell Motil 1999;20:187–97.
[4] Frank D, Kuhn C, Katus HA, Frey N. The sarcomeric Z-disc: a nodal point in signalling and disease. J Mol Med 2006;84:446–68.
[5] Crawford GL, Horowits R. Scaffolds and chaperones in myofibril assembly: putting the striations in striated muscle. Biophys Rev 2011;3:25–32.
[6] Otey CA, Carpen O. Alpha-actinin revisited: a fresh look at an old player. Cell Motil Cytoskeleton 2004;58:104–11.
[7] Dabiri GA, Turnacioglu KK, Sanger JM, Sanger JW. Myofibrillogenesis visualized in living embryonic cardiomyocytes. Proc Natl Acad Sci U S A 1997;94:9493–8.
[8] Wang J, Shaner N, Mittal B, Zhou Q, Chen J, Sanger JM, et al. Dynamics of Z-band based proteins in developing skeletal muscle cells. Cell Motil Cytoskeleton 2005;61:34–48.
[9] Chiu C, Bagnall RD, Ingles J, Yeates L, Kennerson M, Donald JA, et al. Mutations in alpha-actinin-2 cause hypertrophic cardiomyopathy: a genome-wide analysis. J Am Coll Cardiol 2010;55:1127–35.
[10] Hein S, Block T, Zimmermann R, Kostin S, Scheffold T, Kubin T, et al. Deposition of nonsarcomeric alpha-actinin in cardiomyocytes from patients with dilated cardiomyopathy or chronic pressure overload. Exp Clin Cardiol 2009;14:e68–75.
[11] Melo TG, Almeida DS, Meirelles MN, Pereira MC. Disarray of sarcomeric alpha-actinin in cardiomyocytes infected by Trypanosoma cruzi. Parasitology 2006;133:171–8.
[12] Oxford EM, Danko CG, Kornreich BG, Maass K, Hemsley SA, Raskolnikov D, et al. Ultrastructural changes in cardiac myocytes from Boxer dogs with arrhythmogenic right ventricular cardiomyopathy. J Vet Cardiol 2011;13:101–13.
[13] Mohapatra B, Jimenez S, Lin JH, Bowles KR, Coveler KJ, Marx JG, et al. Mutations in the muscle LIM protein and alpha-actinin-2 genes in dilated cardiomyopathy and endocardial fibroelastosis. Mol Genet Metab 2003;80:207–15.
[14] Iuliano S, Fisher SG, Karasik PE, Fletcher RD, Singh SN. QRS duration and mortality in patients with congestive heart failure. Am Heart J 2002;143:1085–91.
[15] Cleland JG, Daubert JC, Erdmann E, Freemantle N, Gras D, Kappenberger L, et al. The effect of cardiac resynchronization on morbidity and mortality in heart failure. N Engl J Med 2005;352:1539–49.
[16] Sachse FB, Torres NS, Savio-Galimberti E, Aiba T, Kass DA, Tomaselli GF, et al. Subcellular structures and function of myocytes impaired during heart failure are restored by cardiac resynchronization therapy. Circ Res 2012;110:588–97.
[17] Aiba T, Hesketh GG, Barth AS, Liu T, Daya S, Chakir K, et al. Electrophysiological consequences of dyssynchronous heart failure and its restoration by resynchronization therapy. Circulation 2009;119:1220–30.
[18] Chakir K, Depry C, Dimaano VL, Zhu WZ, Vanderheyden M, Bartunek J, et al. Galphas-biased beta2-adrenergic receptor signaling from restoring synchronous contraction in the failing heart. Sci Transl Med 2011;3:100ra88.
[19] Chakir K, Daya SK, Tunin RS, Helm RH, Byrne MJ, Dimaano VL, et al. Reversal of global apoptosis and regional stress kinase activation by cardiac resynchronization. Circulation 2008;117:1369–77.
[20] Spragg DD, Akar FG, Helm RH, Tunin RS, Tomaselli GF, Kass DA. Abnormal conduction and repolarization in late-activated myocardium of dyssynchronously contracting hearts. Cardiovasc Res 2005;67:77–86.
[21] Leclercq C, Faris O, Tunin R, Johnson J, Kato R, Evans F, et al. Systolic improvement and mechanical resynchronization does not require electrical synchrony in the dilated failing heart with left bundle-branch block. Circulation 2002;106:1760–3.
[22] Savio E, Goldhaber JI, Bridge JHB, Sachse FB. A framework for analyzing confocal images of transversal tubules in cardiomyocytes. In: Sachse FB and Seemann G, editors. Lecture notes in computer science, 4466. Springer; 2007. p. 110–9.
[23] Lasher RA, Hitchcock RW, Sachse FB. Towards modeling of cardiac micro-structure with catheter-based confocal microscopy: a novel approach for dye delivery and tissue characterization. IEEE Trans Med Imaging 2009;28(8):1156–64.
[24] Juette MF, Gould TJ, Lessard MD, Mlodzianoski MJ, Nagpure BS, Bennett BT, et al. Three-dimensional sub-100 nm resolution fluorescence microscopy of thick samples. Nat Methods 2008;5:527–9.
[25] Mlodzianoski MJ, Juette MF, Beane GL, Bewersdorf J. Experimental characterization of 3D localization techniques for particle-tracking and super-resolution microscopy. Opt Express 2009;17:8264–77.
[26] Schindelin J, Arganda-Carreras I, Frise E, Kaynig V, Longair M, Pietzsch T, et al. Fiji: an open-source platform for biological-image analysis. Nat Methods 2012;9:676–82.
[27] Edgar R, Domrachev M, Lash AE. Gene Expression Omnibus: NCBI gene expression and hybridization array data repository. Nucleic Acids Res 2002;30:207–10.
[28] Barth AS, Aiba T, Halperin V, DiSilvestre D, Chakir K, Colantuoni C, et al. Cardiac resynchronization therapy corrects dyssynchrony-induced regional gene expression changes on a genomic level. Circ Cardiovasc Genet 2009;2:371–8.
[29] Tusher VG, Tibshirani R, Chu G. Significance analysis of microarrays applied to the ionizing radiation response. Proc Natl Acad Sci U S A 2001;98:5116–21.
[30] Kanehisa M, Goto S. KEGG: kyoto encyclopedia of genes and genomes. Nucleic Acids Res 2000;28:27–30.
[31] Barth AS, Kumordzie A, Colantuoni C, Margulies KB, Cappola TP, Tomaselli GF. Reciprocal regulation of metabolic and signaling pathways. BMC Genomics 2010;11:197.
[32] Morris EP, Nneji G, Squire JM. The three-dimensional structure of the nemaline rod Z-band. J Cell Biol 1990;111:2961–78.
[33] Wallgren-Pettersson C, Jasani B, Newman GR, Morris GE, Jones S, Singhrao S, et al. Alpha-actinin in nemaline bodies in congenital nemaline myopathy: immunological confirmation by light and electron microscopy. Neuromuscul Disord 1995;5:93–104.
[34] Gorelik J, Yang LQ, Zhang Y, Lab M, Korchev Y, Harding SE. A novel Z-groove index characterizing myocardial surface structure. Cardiovasc Res 2006;72:422–9.
[35] Bos JM, Ackerman MJ. Z-disc genes in hypertrophic cardiomyopathy: stretching the cardiomyopathies? J Am Coll Cardiol 2010;55:1136–8.
[36] Kuo PL, Lee H, Bray MA, Geisse NA, Huang YT, Adams WJ, et al. Myocyte shape regulates lateral registry of sarcomeres and contractility. Am J Pathol 2012;181:2030–7.
[37] Hein S, Arnon E, Kostin S, Schonburg M, Elsasser A, Polyakova V, et al. Progression from compensated hypertrophy to failure in the pressure-overloaded human heart: structural deterioration and compensatory mechanisms. Circulation 2003;107:984–91.

Supplemental Material

	Sinus Rhythm				Paced			
	RR (ms)	QT (ms)	QTc (ms)	QRS (ms)	RR (ms)	QT (ms)	QTc (ms)	QRS (ms)
Control	636.1±45.3	279.4±10.0	353.5±10.0	48.0±2.0	---	---	---	---
SHF	510.0±44.6 *	255.0±11.8	359.5±15.2 ∓	55.0±3.5 ∓	300.0±0.0	242.0±10.7	441.8±19.5	56.0±2.9 ∓
DHF	435.6±17.6 *	283.3±11.8	430.5±17.5 *	107.7±6.4 *	318.1±7.3	273.2±5.6	485.0±8.4	112.6±3.7
CRT	418.8±11.2 *	296.9±5.3	459.7±10.6 *	106.3±3.9 *	305.3±5.3	238.1±10.6	430.4±15.8 ∓	66.9±2.5 ∓

Table S1. ECG analyses of animal models. Time intervals were measured during sinus rhythm and pacing. RR: time interval between consecutive R-waves, QT: time interval between the Q wave and the T wave, QTc: corrected QT interval, calculated as: QTc=QT/sqrt(RR/1000 ms), QRS: time interval between the Q wave and the S wave. * indicates $p<0.05$ vs control. ∓ indicates $p<0.05$ vs DHF. Number of animals: Control 9, SHF 5, DHF sinus rhythm 9, DHF paced 17, and CRT: 8.

	LVEDP (mmHg)	LVESP (mmHg)	dP/dt_{max} (mmHg/s)	dP/dt_{min} mmHg/s)
Control	7.4 ± 1.2	149.3 ± 7.9	2275.10 ± 141.70	-2462.80 ± 155.50
SHF	23.0 ± 5.7 *	119.7 ± 9.8	1273.00 ± 148.90 *	-1453.80 ± 145.80 *
DHF	21.5 ± 1.9 *	97.8 ± 7.4 *	858.80 ± 73.10 *	-1095.60 ± 86.80 *
CRT	30.2 ± 4.5 *	103.0 ± 5.9 *	959.90 ± 66.00 *	-1128.80 ± 68.80 *

Table S2. Hemodynamic data of animals used in the imaging studies. End-diastolic pressure (LVEDP); left ventricular end-systolic pressure (LVESP); maximal rate of change in pressure (dP/dt_{max}); minimal rate of change in pressure (dP/dt_{min}). * indicates $p<0.05$ vs control.

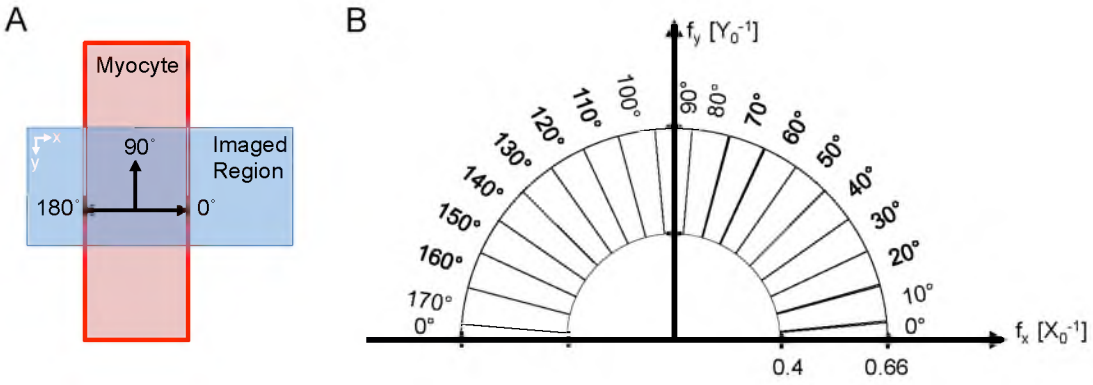

Fig. S1. (A) Schematic of imaging setup with overlay of angles used for Fourier analysis. (B) Two-dimensional representation of cropping in the Fourier domain into a specified distance range and binning coefficients into various angle ranges.

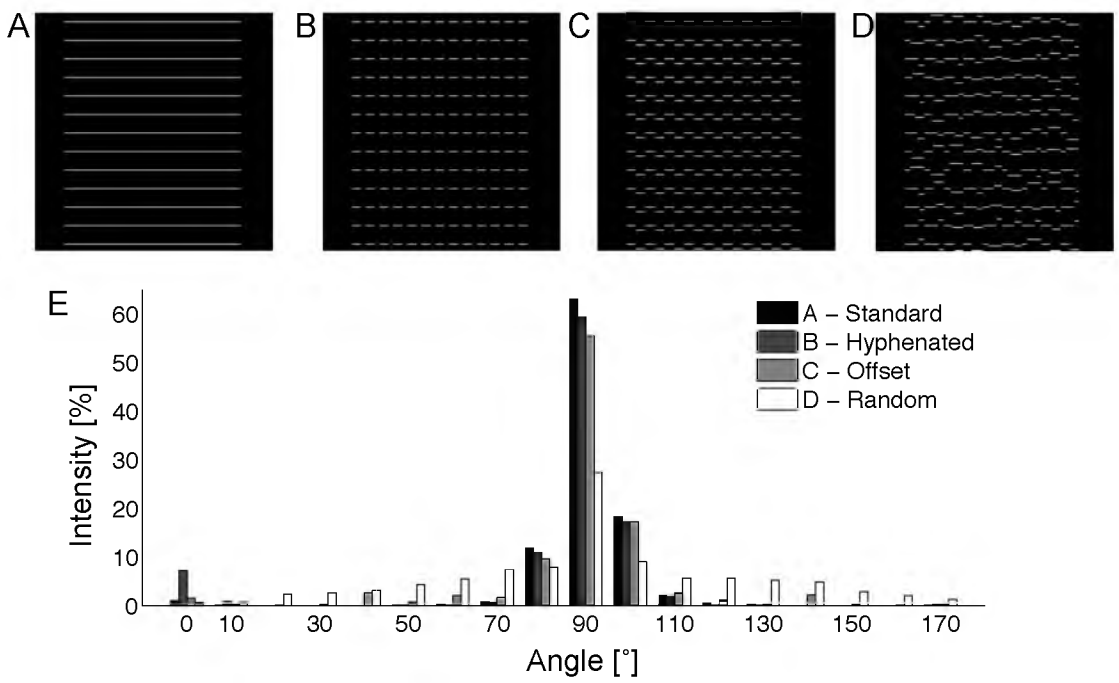

Figure S2. Intensity angle analysis. (A-D) 2D slices from synthetic image stacks, which model patterns seen in Z-disks in myocyte segments. These image stacks are at the same resolution as our confocal images and constant in Z-direction. (E) Fourier analysis on the synthetic images.

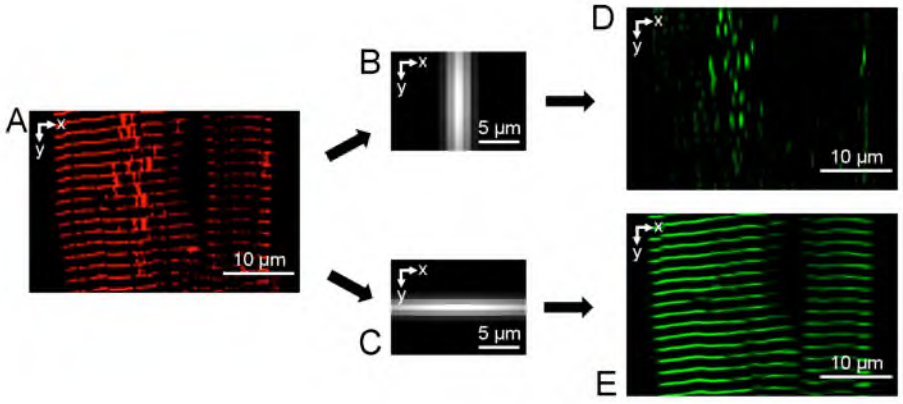

Figure S3. Detection of longitudinal depositions. (A) XY cross-section from pre-processed image stack (I_{PRE}) from a CRT cell. (B) Discretized 2D Gaussian function of dimensions [17 17 1] with σx =0.1 µm and σy =1 µm for detection along the longitudinal direction. (C) Discretized 2D Gaussian function of dimensions [17 17 1] with σx =1 µm and σy =0.1 µm for detection along the transversal direction. (D) Resulting XY image (I_{LONG}) after cross-correlation of I_{PRE} with mask in (B). (E) Resulting XY image (I_{TRANS}) after cross-correlation of I_{PRE} with mask in (C).

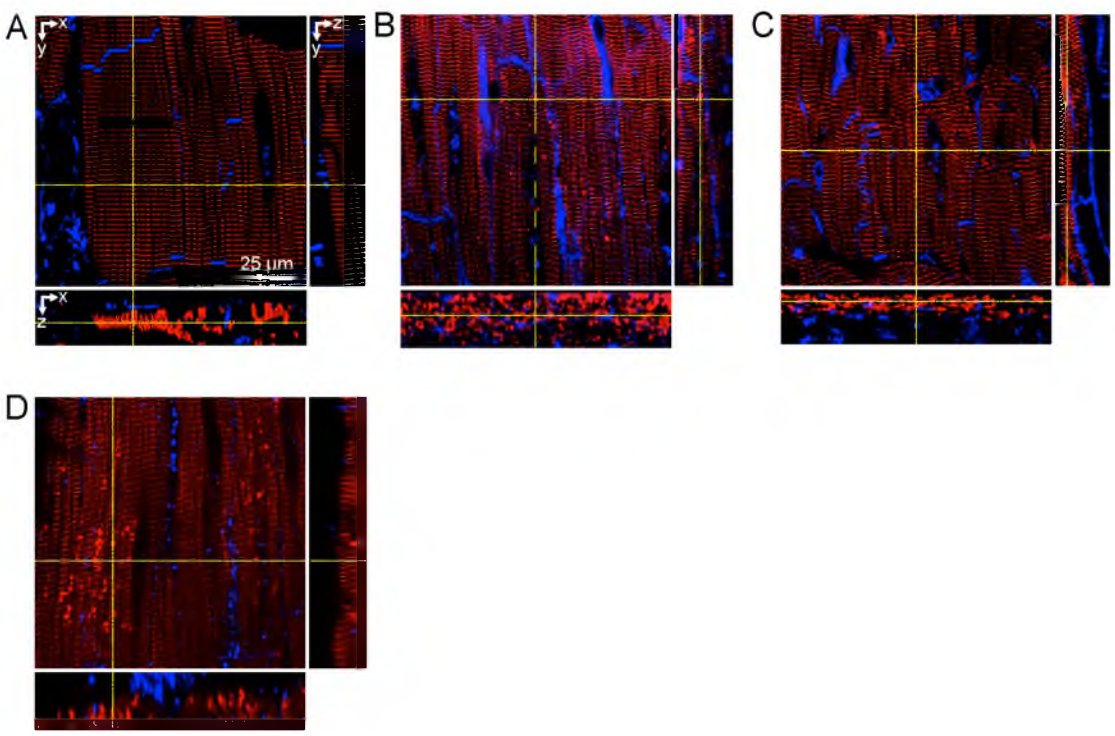

Figure S4. Unprocessed 3D image stacks of (A) control, (B) SHF, (C) DHF, and (D) CRT tissue labeled with WGA (blue) and for α-actinin (red). Yellow lines indicate cross-sections.

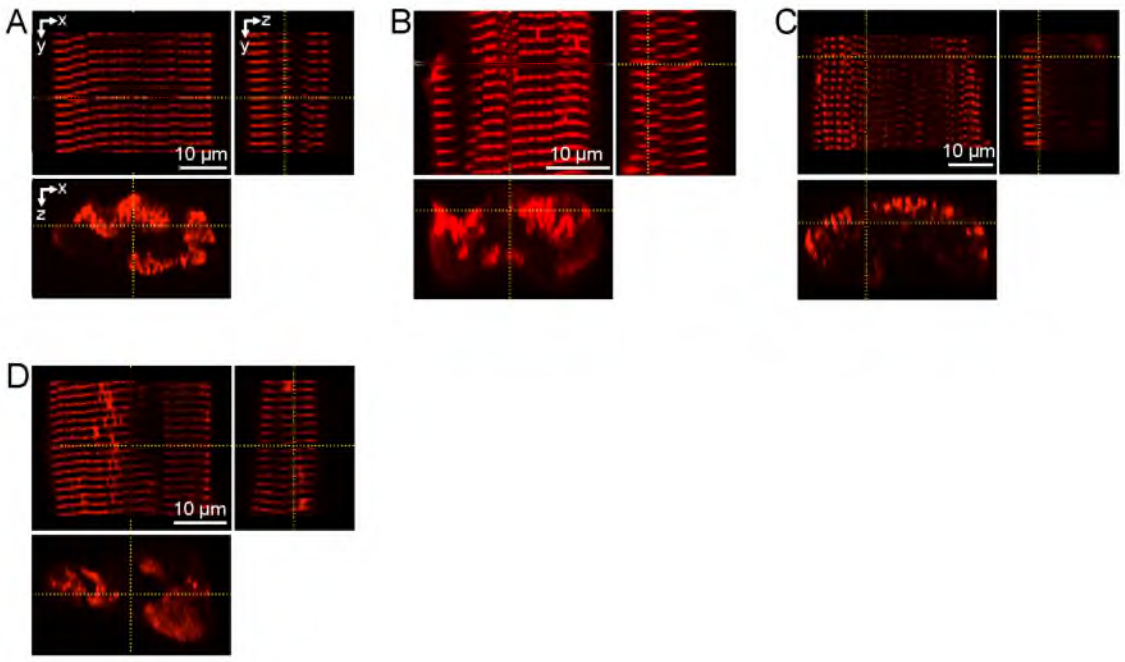

Figure S5. Unprocessed 3D image stacks of sections of isolated cardiac myocytes from (A) control, (B) SHF, (C) DHF, and (D) CRT animals. Sections were labeled for α-actinin.

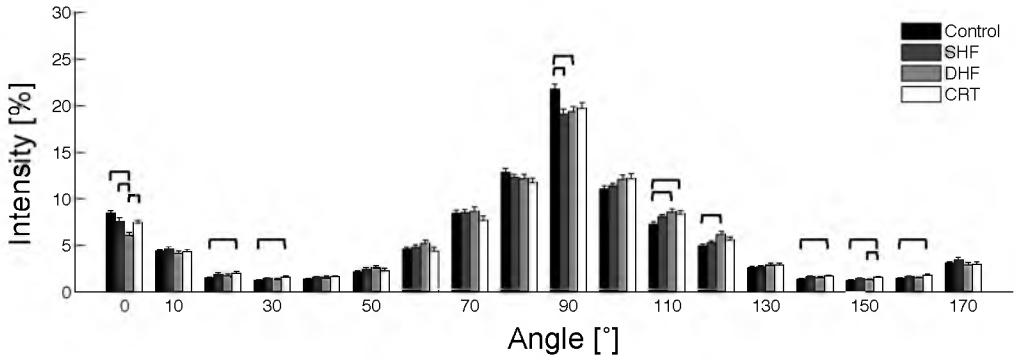

Figure S6. Quantitative analyses of α-actinin distributions in control, SHF, DHF, and CRT cells. Fourier analysis of image stacks. Intensities for full 180° were calculated from the myocyte segments, averaged and normalized.

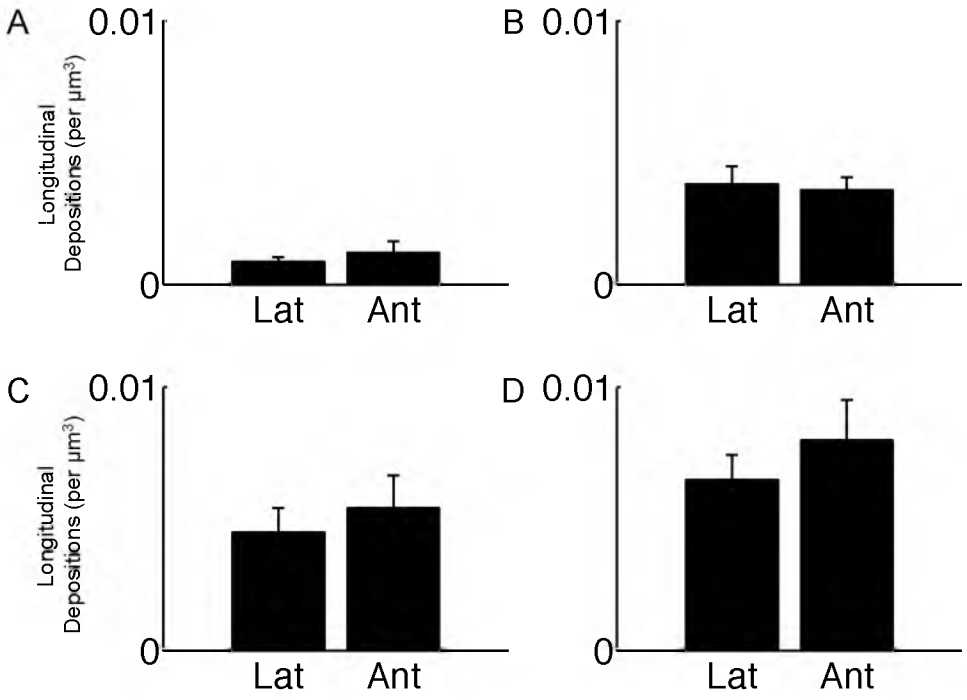

Figure S7. Densities of longitudinal depositions in lateral (Lat) and anterior (Ant) regions of the left ventricle from (A) control, (B) SHF, (C) DHF, and (D) CRT models. No statistical significant difference was found between any of the groups.

Fig. 8

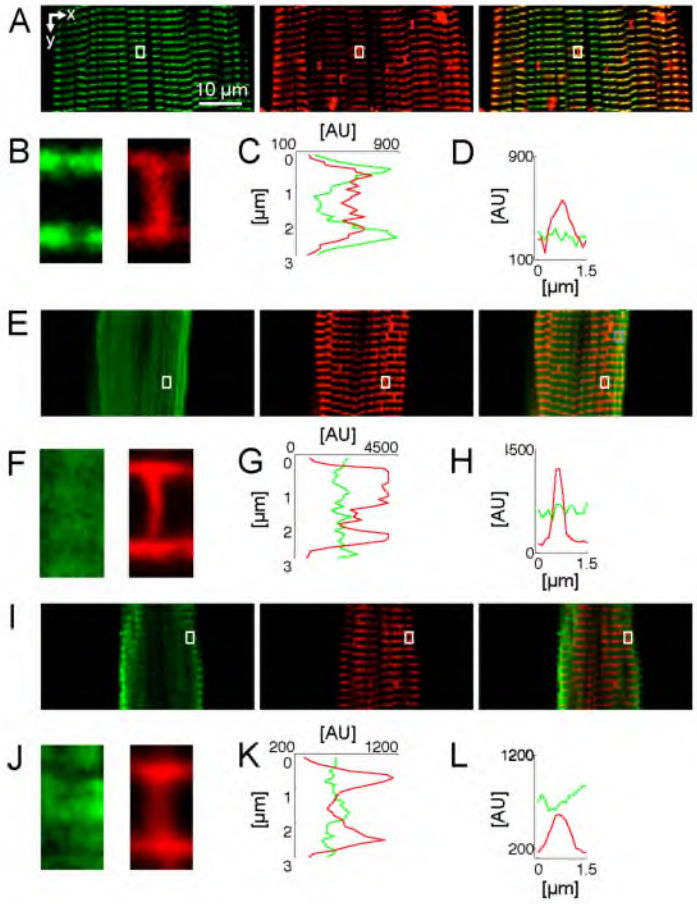

Fig. S8. Imaging and analysis of α-actinin colocalization with titin, actin, and myosin in CRT cells. (A) Titin (green) is colocalized with α-actinin (red) in the z-lines, but not in longitudinal deposition of α-actinin. (B) Zoom in longitudinal deposition highlighted in (A) by white rectangle. Intensity profiles (C) along and (D) transversely through the deposition indicate absence of titin in the depositions. (E) Actin (green) is not colocalized with α-actinin (red). (F) Zoom in longitudinal deposition highlighted in (E) by white rectangle. Intensity profiles (G) along and (H) transversely through the deposition indicate that the colocalization of actin with α-actinin is similarly small in z-lines and depositions.(I) Myosin (green) is not colocalized with α-actinin (red). (J) Zoom in longitudinal deposition highlighted in (I) by white rectangle. Intensity profiles (K) along and (L) transversely through the deposition indicate negative co-localization in z-lines and depositions. The images in (B), (F) and (J) are 1.5 µm in x and 3.0 µm in y and focused on a longitudinal deposition. A detailed colocalization analysis is presented in Fig. 6.

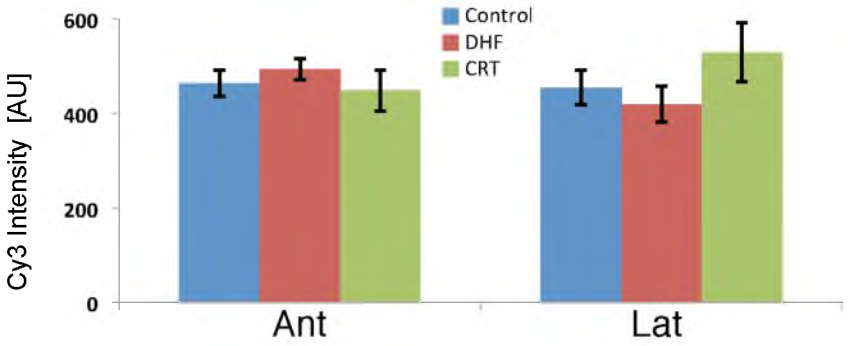

Figure S9. Analysis of ACTN2 gene expression. ACTN2 expression did not change significantly in Ant and Lat myocardium of control, DHF, and CRT animals (GSE14327; single color array, labeling with Cy3 only).

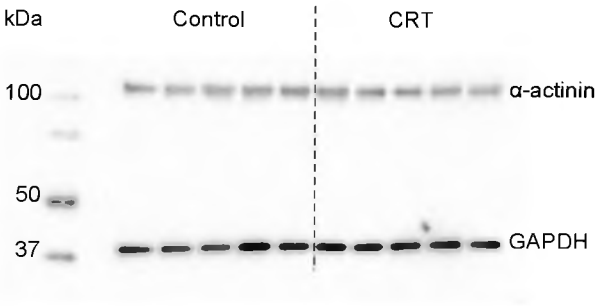

Figure S10. Western blot of α-actinin and GAPDH. Differences of normalized protein density of α-actinin in control and CRT models were not significant.

CHAPTER 3

CARDIAC RESYNCHRONIZATION THERAPY REDUCES SUBCELLULAR HETEROGENEITY OF RYANODINE RECEPTORS, T-TUBULES, AND CA^{2+} SPARKS PRODUCED BY DYSSYNCHRONOUS HEART FAILURE

Li H*, Lichter JG*, Seidel T*, Tomaselli GF, Bridge JH, Sachse FB. Cardiac Resynchronization Therapy Reduces Subcellular Heterogeneity of Ryanodine Receptors, T-Tubules, and Ca^{2+} Sparks Produced by Dyssynchronous Heart Failure. *Circ HF.* 2015;8:1105:1114. Reprinted with permission from Wolters Kluwer Health Lippincott Williams & Wilkins©. No modifications will be permitted.

* Dr. Li, JG Lichter, and Dr. Seidel contributed equally to this work.

Original Article

Cardiac Resynchronization Therapy Reduces Subcellular Heterogeneity of Ryanodine Receptors, T-Tubules, and Ca^{2+} Sparks Produced by Dyssynchronous Heart Failure

Hui Li, MD, PhD*; Justin G. Lichter, BSc*; Thomas Seidel, MD, PhD*; Gordon F. Tomaselli, MD; John H.B. Bridge, PhD; Frank B. Sachse, PhD

Background—Cardiac resynchronization therapy (CRT) is a major advance for treatment of patients with dyssynchronous heart failure (DHF). However, our understanding of DHF-associated remodeling of subcellular structure and function and their restoration after CRT remains incomplete.

Methods and Results—We investigated subcellular heterogeneity of remodeling of structures and proteins associated with excitation–contraction coupling in cardiomyocytes in DHF and after CRT. Three-dimensional confocal microscopy revealed subcellular heterogeneity of ryanodine receptor (RyR) density and the transverse tubular system (t-system) in a canine model of DHF. RyR density at the ends of lateral left ventricular cardiomyocytes was higher than that in cell centers, whereas the t-system was depleted at cell ends. In anterior left ventricular cardiomyocytes, however, we found a similar degree of heterogeneous RyR remodeling, despite preserved t-system. Synchronous heart failure was associated with marginal heterogeneity of RyR density. We used rapid scanning confocal microscopy to investigate effects of heterogeneous structural remodeling on calcium signaling. In DHF, diastolic Ca^{2+} spark density was smaller at cell ends versus centers. After CRT, subcellular heterogeneity of structures and function was reduced.

Conclusions—RyR density exhibits remarkable subcellular heterogeneity in DHF. RyR remodeling occurred in lateral and anterior cardiomyocytes, but remodeling of t-system was confined to lateral myocytes. These findings indicate that different mechanisms underlie remodeling of RyRs and t-system. Furthermore, we suggest that ventricular dyssynchrony exacerbates subcellular remodeling in heart failure. CRT efficiently reduced subcellular heterogeneity. These results will help to explain remodeling of excitation–contraction coupling in disease and restoration after CRT. **(*Circ Heart Fail*. 2015;8:1105-1114. DOI: 10.1161/CIRCHEARTFAILURE.115.002352.)**

Key Words: cardiac resynchronization therapy ■ excitation–contraction coupling ■ heart failure ■ myocyte ■ remodeling ■ ryanodine receptors ■ transverse tubular system

Cardiac resynchronization therapy (CRT) is an established clinical therapy for patients with moderate to severe heart failure (HF). CRT is based on biventricular pacing. It acutely improves left ventricular (LV) mechanical performance[1–3] and reduces myocardial oxygen consumption in patients with HF and intraventricular conduction delays.[4] Several clinical trials demonstrated that CRT leads to a reduction of HF-related rehospitalizations and overall mortality in patients with dyssynchronous HF (DHF).[5–9] A clinical marker of DHF is prolonged QRS duration, which reflects interventricular delays of electric activation. Consequently, mechanical contraction is regionally delayed, which aggravates weak cardiac performance in DHF patients.

Clinical Perspective on p 1114

Although recent studies demonstrated remarkable remodeling of subcellular structures and function in DHF and partial restoration in response to CRT,[10–13] we are only starting to understand pathological remodeling and effects of CRT at the microscopic scale. This study focuses on remodeling of excitation–contraction (EC) coupling in DHF and the ability of CRT to restore structure and function at subcellular level. EC coupling is the mechanism by which an action potential at the membrane of a muscle cell initiates a cascade of events that result in release of Ca^{2+} from the sarcoplasmic reticulum (SR) and activation of contraction. Our current understanding of EC coupling in ventricular myocytes is organized around the concept of the couplon.[14] A couplon comprises one or more voltage-gated L-type Ca^{2+} channels in the sarcolemma and a cluster of ryanodine

Received March 23, 2015; accepted August 17, 2015.

From the Nora Eccles Harrison Cardiovascular Research and Training Institute (H.L., J.G.L., T.S., J.H.B., F.B.S.), and Department of Bioengineering (J.G.L., F.B.S.), University of Utah, Salt Lake City; and Division of Cardiology, Johns Hopkins University School of Medicine, Baltimore, MD (G.F.T.).

*Dr Li, J.G. Lichter, and Dr Seidel contributed equally to this work.

The Data Supplement is available at http://circheartfailure.ahajournals.org/lookup/suppl/doi:10.1161/CIRCHEARTFAILURE.115.002352/-/DC1.

Correspondence to Frank B. Sachse, PhD, Nora Eccles Harrison Cardiovascular Research and Training Institute, University of Utah, 95 S 2000 E, Salt Lake City, UT 84112. E-mail frank.sachse@utah.edu

receptors (RyRs) in the terminal cisternae of the SR.[15] L-type Ca^{2+} channels and RyRs are separated by a junction of ≈12 nm.[16] In ventricular myocytes, couplons are commonly associated with the transverse tubular system (t-system), which is a specialization of the sarcolemma penetrating into the interior of myocytes and in close proximity to the SR. The t-system facilitates rapid transmission of membrane voltage changes into the cell interior to enable synchronous activation of couplons. Our current knowledge of the mechanism by which couplons activate the Ca^{2+} transient is based on the classical work of Fabiato[17] and insights into the subcellular arrangement of structures involved in EC coupling by microscopy.[18] Couplons are activated when L-type Ca^{2+} channels admit small quantities of Ca^{2+} into the junctional region and gate RyRs. Couplons are separated from one another by ≈1 μm.[19] When Ca^{2+} is released by the RyRs, it produces a local Ca^{2+} release event or Ca^{2+} spark.[20,21] The spread of Ca^{2+} in the cytoplasm is governed by diffusion and buffering. Ca^{2+} transients are believed to result from the summation of the activation of many couplons.

Alterations of Ca^{2+} transients are a common feature of cardiac myocytes from HF hearts and thought to contribute to the progression of HF.[22] Recent studies investigated the connection between alterations of Ca^{2+} transients and remodeling of the t-system. The studies suggested that remodeling of the t-system in ventricular myocytes is a consequence of tachycardia-induced HF,[23–25] infarction,[26] and DHF.[11] Our previous work on isolated myocytes revealed regional depletion of t-system in canine DHF models.[11] In particular, lateral LV myocytes were affected by DHF, but not myocytes from the anterior LV wall. We demonstrated that t-system depletion in DHF was accompanied by increased occurrence of nonjunctional RyR clusters. A remarkable recent finding is that t-system depletion is reversible. Partial restoration of t-system was found after CRT,[11] sarcoplasmic reticulum Ca2+ ATPase (SERCA2a) gene therapy,[27] and mechanical unloading of the heart.[28] In those studies, t-system restoration was associated with restoration of Ca^{2+} transients, which emphasizes the crucial role of the t-system for efficient EC coupling.

Beyond those studies, remarkably little is known about the mechanisms and the degree of remodeling and restoration of the t-system. In particular, little is known about the subcellular heterogeneity of remodeling of the t-system and associated proteins, such as RyRs, as well as the effects of this structural remodeling on cell function. Also, we have only sparse information on restoration of structures and function at the subcellular scale. Here, we studied an animal model of synchronous HF (SHF) based on right atrial pacing and a model of DHF based on right ventricular pacing to test the hypothesis that ventricular dyssynchrony accentuates the extent and heterogeneity of t-system and RyR remodeling in HF. Although both models are based on rapid pacing and lead to congestive HF, the DHF model additionally reproduces clinical findings of interventricular delays of electric activation and delayed mechanical contraction of the lateral LV wall. Furthermore, we used an animal model of CRT to test the hypothesis that CRT effectively reduces the extent and heterogeneity of remodeling after DHF. We applied 3-dimensional (3D) confocal microscopy and image analysis to provide insights into the spatial distribution of the t-system and RyRs in cardiac myocytes from animal models of SHF, DHF, and CRT. Segmentation of myocytes in images of cardiac tissue allowed for 3D reconstructions of cells and quantitative analyses of subcellular distributions. We investigated for the first time the subcellular heterogeneity and degree of remodeling of t-system and RyRs in different models of HF and after CRT. Additionally, we measured Ca^{2+} spark density in isolated ventricular myocytes using dual labeling with fluorescent dyes and rapid scanning confocal microscopy, which allowed acquisition of 2-dimensional image sequences at high spatiotemporal resolution. We developed image-processing methods for analysis of these image sequences to investigate at the subcellular scale whether structural heterogeneity is accompanied by functional heterogeneity.

Methods

Animal Models of HF and CRT

All procedures involving the handling of animals were approved by the Animal Care and Use Committees of the Johns Hopkins University and the University of Utah. Protocols complied with the published Guide for the Use and Care of Laboratory Animals published by the National Institutes of Health.

We generated canine models of SHF, DHF, and CRT. These models have been described and characterized in detail previously.[11,12,29–32] In brief, adult mongrel canines (25–30 kg) were used as control and models of SHF, DHF, and CRT. DHF was induced by either 6 weeks of right ventricular pacing or left bundle branch ablation followed by 6 weeks of right atrial pacing. The CRT model was identical to the DHF model for the first 3 weeks, followed by 3 weeks of biventricular pacing. SHF animals underwent right atrial pacing for 6 weeks. The pacing rate for SHF, DHF, and CRT animals was 170 to 200 beats per minute. Our methods for monitoring, tissue collection, and cell isolation are described in the Data Supplement.

Tissue Preparation, Fluorescent Labeling, and 3D Confocal Microscopy

Our approach for preparation and labeling of tissue is detailed in the Data Supplement. We used wheat germ agglutinin conjugated to a fluorophore for labeling of the sarcolemma, t-tubules, and the interstitial space. RyRs were labeled with a monoclonal antibody (MA3-916; ThermoFisher Scientific, Waltham, MA). After labeling, tissue sections were placed on a glass slide, embedded in Fluoromount-G (Electron Microscopy Science, Hatfield, PA), and covered with a No. 1.5 coverslip. 3D image stacks were obtained from labeled tissue sections using a Zeiss LSM 5 Live Duo confocal microscope (Carl Zeiss, Jena, Germany) with a 63× oil immersion objective (numerical aperture: 1.4). Alexa Fluor 488 and 555 were excited using a 488 and 543 nm laser, respectively. Emitted light was band-pass filtered at 505 to 530 nm and long-pass filtered at 560 nm, respectively. Typical stack dimensions were 1024×1024×240 voxels at a resolution of 0.1×0.1×0.1 μm.

Analysis of T-System and RyR Clusters in Image Stacks

A detailed description of the analyses is provided in Data Supplement. In short, we applied methods for noise reduction, deconvolution, and background removal to the image stacks. The wheat germ agglutinin and RyR images were segmented using histogram-based thresholding. Segmented wheat germ agglutinin images were used for semiautomatic segmentation of myocytes.[33] Segmented cells then served as masks to analyze RyR clusters and sarcolemma, including t-tubules. Cells were divided into 2 regions: 0 to 10 μm and 10 to 40 μm from a longitudinal cell end. Analysis of each RyR cluster yielded sum of intensity and intensity-weighted centroid position. Clusters with intensities >90% of all clusters in the same cell (90th percentile) were defined as high-intensity clusters. To determine the distance of voxels

to the nearest sarcolemma, we calculated Euclidean distance maps from the segmented wheat germ agglutinin images (Figure I in the Data Supplement). As a measure of t-system density, we used the mean distance of intracellular voxels to the nearest sarcolemma (Δ_{SL}). Accordingly, high and low distances indicate low and high t-system densities, respectively. Distances of RyR cluster centroids to the nearest sarcolemma (Δ_{RyR}) were calculated. We analyzed RyR clusters in groups proximal (0–1 μm) and distal (> 1 μm) to the sarcolemma. RyR cluster density (ρ_{RyR}) was computed by dividing the number of clusters by the volume of interest. Additionally, we normalized the total intensity of RyR clusters in each segmented cell and in subcellular regions to the corresponding volumes. Dividing intensity densities of subcellular regions by the intensity density of the whole cell yielded subcellular RyR intensity distribution (I_{RyR}).

Rapid Scanning Confocal Microscopy and Analysis of Ca^{2+} Sparks

Isolated LV lateral myocytes were incubated at room temperature in modified Tyrode's solution containing 12.5 μmol/L of the Ca^{2+}-sensitive dye Fluo-4 AM (Invitrogen) for 20 minutes followed by incubation in 6.25 μmol/L of the membrane staining dye Di-8-Anepps (Invitrogen) for 8 minutes. Cells were placed in a perfusion bath system and allowed to settle on the glass slide. The chamber was perfused with the modified Tyrode's solution containing either 2 or 4 mmol/L Ca^{2+} and held at 37°C. Imaging was performed using a Zeiss LSM 5 Live Duo confocal microscope equipped with a 63× oil immersion objective. Only brick-shaped cells with clear striations were imaged. A diode laser emitting a wavelength of 489 nm was used to excite both dyes simultaneously. Emitted light was filtered using a dichromatic mirror and 2 bandpass filters of 505 to 610 nm and 560 to 675 nm for capturing Fluo-4 and Di-8-Anepps signals, respectively. Cells were conditioned with a train of at least 10 stimuli at 0.5 Hz. Image acquisition was triggered 460 ms after the final stimulus to measure Ca^{2+} in the diastolic phase. Sequences of 100 2-dimensional images were acquired at a size of 256×1024 pixels and a frame rate of 9.3 ms/frame. Pixel sizes were 0.1×0.1 μm. Details of the detection algorithm are provided in the Data Supplement. Briefly, cells were segmented using histogram-based thresholding in Di-8-Anepps images (Figure II in the Data Supplement). After preprocessing of the Fluo-4 images (Figures II and III in the Data Supplement), sparks were detected in the cell interior using mode plus 5× standard deviation of the intensity values. We measured the total number of sparks, number of sparks within 10 μm of the cell end, and the number of sparks between 10 and 40 μm from the cell end. Spark number was normalized by temporal duration and area used for detection, which yielded spark density (sparks/μm^2/s).

Statistical Analyses

All results are presented as mean±standard error. All statistical analyses were performed in Matlab R2012b (The Mathworks Inc., Natick, MA). We accounted for multiple measurements from an animal by averaging of data for each animal. We used 1-way analysis of variance followed by Tukey's multiple comparison for microstructural analyses. We applied the paired *t* test for functional analyses. Significance of differences was defined as $P<0.05$.

Results

Subcellular Heterogeneity of Remodeling of RyRs and T-System in DHF

We first analyzed RyR clusters and t-tubules in myocytes in LV lateral tissue from control animals (Figure 1). All images were preprocessed, which improved signal-to-noise ratio and resolution (Figure 1A–1D versus Figure 1E–1H). Control cells exhibited a dense t-system (Figure 1E) and homogenous intracellular RyR density (Figure 1F). This was also visible in 3D reconstructions of sarcolemma and RyR clusters in a segmented cell (Figure 2A–2C). RyR clusters of high intensity were found evenly distributed in all cell regions. We measured the mean intracellular distance to the sarcolemma (Figure 2D). the mean distance of RyR clusters to the sarcolemma (Figure 2E), the mean density of RyR clusters (Figure 2F), and the normalized intensity of RyR signal (Figure 2G) in regions at a distance of 0 to 10, 10 to 20, 20 to 30, and 30 to 40 μm to a cell end. These quantitative measures indicate homogeneity of t-system and RyRs within LV lateral cells in control animals.

In contrast to control, DHF tissue from lateral LV tissue showed a pronounced loss of t-tubules near longitudinal cell ends together with striking heterogeneity in RyR density (Figure 3). RyR intensities were considerably higher near cell ends as compared with cell centers. In this overview image, most cells were affected and exhibited this heterogeneity at least at one cell end. A high-resolution 3D image stack is shown in Figure 4A–4C. Cell ends almost completely lacked t-tubules and exhibited increased RyR intensities. This was confirmed when inspecting 3D reconstructions of sections through a representative DHF cell (Figure 4D–4F). T-tubules were virtually absent within 10 μm from the cell end, whereas RyR clusters of high intensity aggregated in this region. Quantitative data corresponded to these findings. The mean intracellular distance to the sarcolemma was increased within 10 μm from the cell end versus other regions (Figure 4G). The mean distance of RyR clusters to the sarcolemma decreased slightly from the cell end to center (Figure 4H). The increase of density and intensity of RyR clusters at the cell end was remarkable (Figure 4I and 4J, respectively). These findings suggest substantial subcellular heterogeneity of t-tubule and RyR cluster remodeling in LV lateral DHF myocytes.

Partial Restoration in Response to CRT

We next investigated whether CRT was able to reduce the DHF-associated subcellular heterogeneity of remodeling. Our model of CRT is based on application of the DHF model for 3 weeks followed by 3 weeks of resynchronization by rapid biventricular pacing. The RyR and t-system density in myocytes from LV lateral tissue of CRT animals appeared more homogeneous than in DHF (Figure 5A–5C), indicating partial structural restoration. 3D reconstructions of longitudinal and transverse sections through an example cell are presented in Figure 5D–5F, showing low t-system densities in close proximity to the cell end. However, large regions devoid of t-tubules as found in DHF were not observed. Similarly, RyR clusters of high intensity still appeared in higher concentration near the cell end, but to a lesser degree than in DHF. Quantitative analyses confirmed partial restoration of subcellular homogeneity in this cell (Figure 5G–5J).

Statistical Analyses of RyR and T-System Remodeling

We applied the same analyses used for the examples to a group of control, DHF, and CRT cells. Extracted features binned by increasing distance from the cell end are presented in Figure IV in the Data Supplement. Because t-system loss and increased RyR intensities in DHF occurred primarily near cell ends, we compared t-system and RyR properties in regions 0 to 10 μm with regions 10 to 40 μm from the cell end.

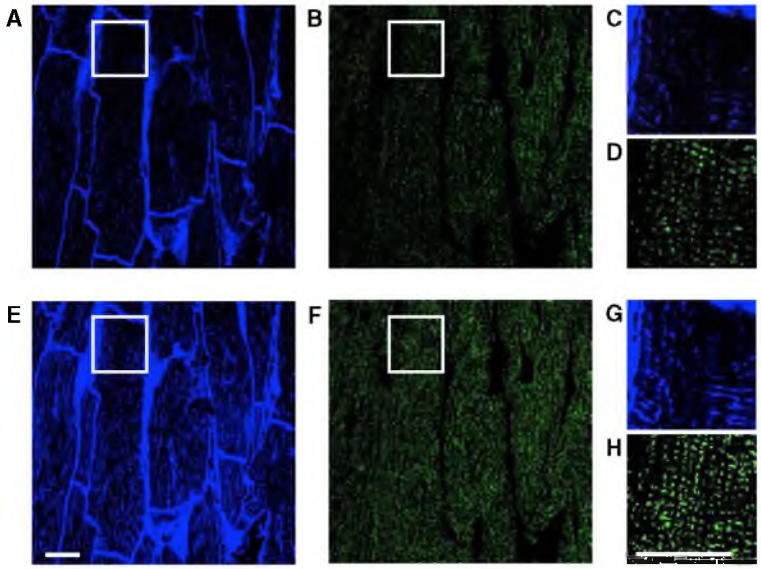

Figure 1. Preprocessing of confocal microscopic images. XY sections at a depth of 27 μm from a 3D image stack (102.4×102.4×35 μm) of control tissue. **A–D**, Unprocessed data. **E–H**, Preprocessed data. Green indicates ryanodine receptors; and Blue, wheat germ agglutinin. White squares indicates zoom-in regions shown in **C** and **D** and in **G** and **H**. Scale bars: 20 μm.

The mean intracellular distance to the nearest sarcolemma indicated high t-system density in control, whereas DHF cells exhibited a pronounced loss of t-tubules at cell ends (Figure 6A). CRT was not able to completely restore this measure to levels of control, but the intracellular distance to the nearest sarcolemma was similar at cell ends and centers. In our analysis of the mean distance of RyR clusters to the sarcolemma (Figure 6B), we found increased values in DHF and CRT versus control near cell ends (0.67±0.4 and 0.66±0.09 versus 0.47±0.03 μm, respectively). The distance was similar in cell centers of DHF, CRT, and control cells (0.52±0.03. 0.52±0.06, and 0.51±0.04 μm, respectively). DHF cells exhibited significant subcellular heterogeneity of mean RyR–sarcolemma distance.

RyR cluster densities ranged from 0.75 to 0.91 μm^{-3}, and our analysis did not indicate significant subcellular heterogeneity in DHF and CRT (Figure 6C). In contrast, analyses of normalized RyR intensities (Figure 6D) revealed that DHF was associated with a substantial increase at cell ends (134±10% of cellular mean) and a decrease in centers (92±2%) versus control (110±6% and 98±1%, respectively). CRT cells presented RyR distributions similar to those of DHF.

Our data show that DHF is associated with pronounced heterogeneity of remodeling of t-tubules and RyR clusters at cell centers and ends. We next sought to determine whether similar changes occur when grouping RyR clusters by their distance to the sarcolemma (Figure V in the Data Supplement). We therefore analyzed cluster density and intensity within 0 to 1 μm and at a distance ≥1 μm to the sarcolemma. Cluster densities did not differ between groups or regions (Figure 6E). However, when analyzing RyR cluster intensities (Figure 6F), DHF cells exhibited decreased intensities 0 to 1 μm (91±2% of cell mean) and strikingly increased intensities ≥1 μm from the sarcolemma (144±12%). A similar, but less pronounced distribution was found in CRT cells (95±1% and 124±6%. respectively). RyR cluster intensity in control cells was almost

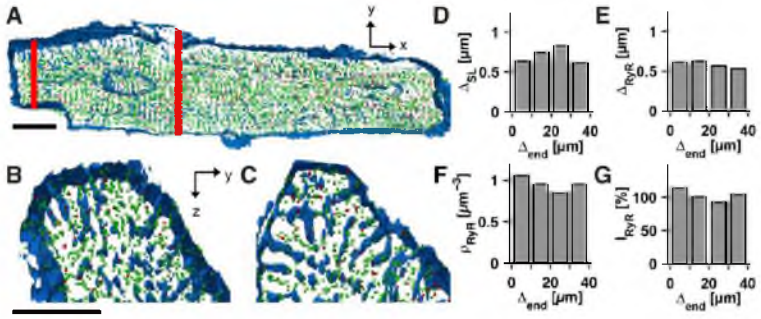

Figure 2. Visualization and analysis of control cell. **A–C**, 3D visualizations of 4-μm-thick sections through example control cell. **A**, Longitudinal section; transverse section 5 μm from cell end (**B**) and 40 μm from cell end (**C**). Red bars indicate section planes; Blue, sarcolemma; and Green and red spheres, ryanodine receptor (RyR) clusters. Clusters of high intensity (90th percentile) are shown in red. Scale bars: 10 μm. Scale bar in **B** applies to **C**. Analysis of mean intracellular voxel distance to the nearest sarcolemma (**D**), mean RyR cluster distance to nearest sarcolemma (**E**), RyR cluster density (**F**), and RyR intensity per volume normalized to mean value of the whole cell (**G**). These parameters were analyzed at distances 0 to 40 μm from the left cell end in bins of 10 μm.

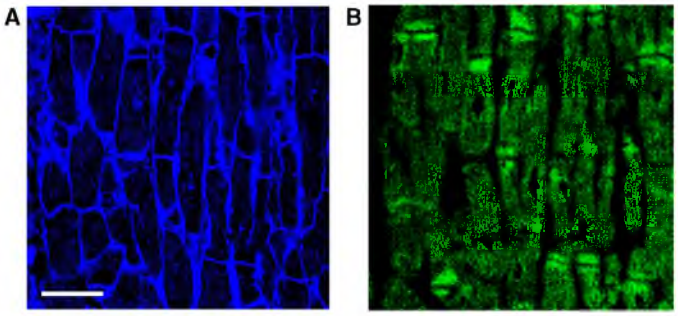

Figure 3. Confocal microscopic image of dyssynchronous heart failure (DHF) tissue from lateral left ventricular (LV) wall. **A**, T-system density decreases at cell ends. **B**, Ryanodine receptor (RyR) clusters exhibit increased intensities near cell ends. Scale bar: 40 μm.

equally distributed at distances 0 to 1 μm and ≥1 μm from the sarcolemma (101±2% and 99±8%, respectively). In DHF and less pronounced after CRT, we also found increased RyR intensities ≥1 μm from the sarcolemma in cell centers. RyR intensities in control, however, were homogeneous throughout the cell (Figure VIA and VIB in the Data Supplement). In all experimental groups, the majority of RyR clusters was found within 1 μm of the sarcolemma (Figure VIC in the Data Supplement).

In summary, control cells were more homogeneous at the subcellular scale than DHF and CRT cells. DHF led to a significant loss of t-tubules and increased RyR intensities at cell ends versus centers, causing pronounced subcellular heterogeneity. Increased RyR intensities were found particularly in regions ≥1 μm from the sarcolemma. CRT was able to partially reverse these structural changes.

RyR Remodeling Despite Preserved T-System in Anterior Cells in DHF

In previous work, we found that subcellular remodeling of the t-system is regional, that is, cells isolated from the lateral LV wall of DHF animals exhibited a higher degree of t-system depletion than cells from the anterior wall.[11] To shed light on this regional heterogeneity of subcellular remodeling, we additionally studied cells from the anterior LV wall obtained from DHF animals. An example cell is shown in Figure VII in the Data Supplement. The mean intracellular distance to the nearest sarcolemma did not differ from control proximal and distal to the cell end (Figure VIIIA in the Data Supplement). In contrast to lateral cells, DHF in anterior cells was not associated with heterogeneous t-system remodeling. However, the distribution of RyR intensity in anterior DHF cells was heterogeneous as observed in lateral cells (Figure VIIID and VIIIF in

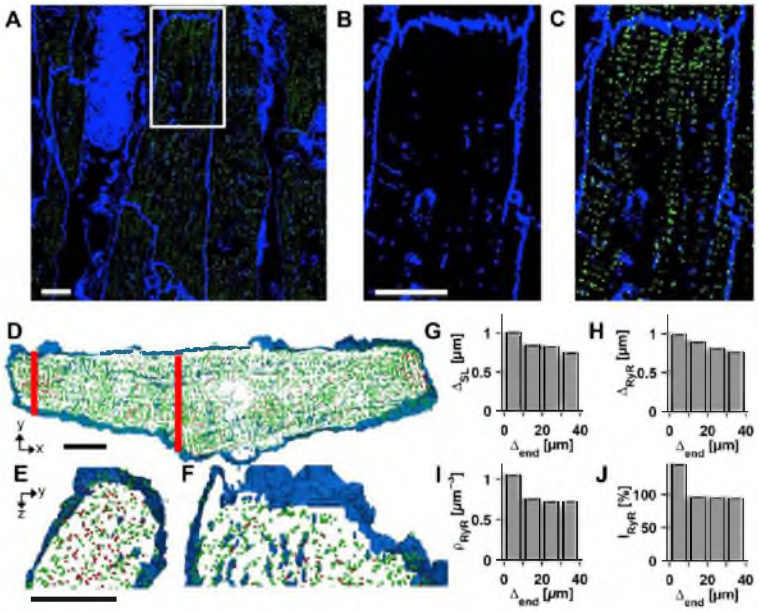

Figure 4. Visualization and analysis of dyssynchronous heart failure (DHF) cell. **A–C**, Confocal microscopic images of extracellular space (blue) and ryanodine receptor (RyR) clusters (green) in DHF tissue. **B** and **C**, Zoom-ins from the region indicated by the white rectangle. Note the increase in RyR intensity and t-system depletion near cell ends. **D–F**, 3D visualizations of 4-μm-thick sections through example DHF cell. Longitudinal section (**D**), transverse section 5 μm from cell end (**E**), and transverse section 40 μm from cell end (**F**). Red bars indicate section planes; Blue, sarcolemma; and Green and red spheres, RyR clusters. Clusters of high intensity (90th percentile) are shown in red. All scale bars: 10 μm. Scale bar in **B** applies to **C**. Scale bar in **E** applies to **F**. Analysis of mean intracellular voxel distance to the nearest sarcolemma (**G**), mean RyR cluster distance to nearest sarcolemma (**H**), RyR cluster density (**I**), and RyR intensity per volume normalized to mean value of the whole cell (**J**).

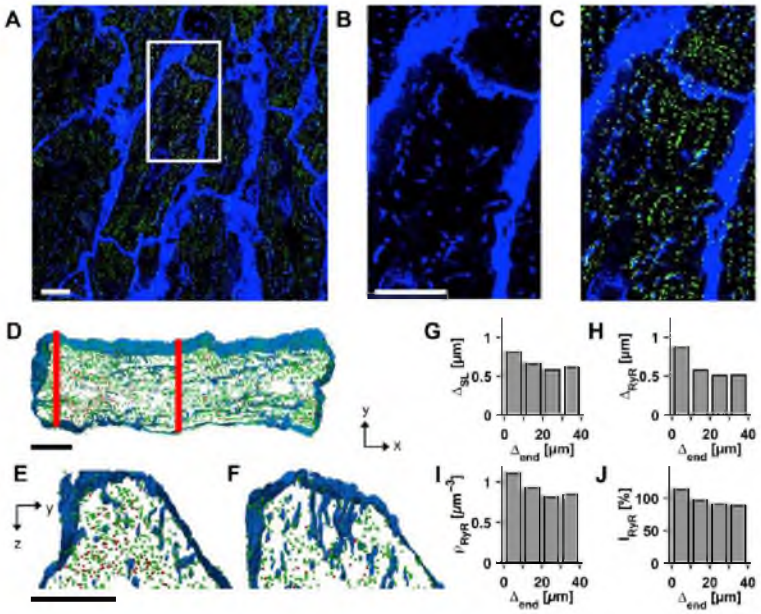

Figure 5. Visualization and analysis of cardiac resynchronization therapy (CRT) cell. **A–C**, Confocal microscopic images of the extracellular space (blue) and ryanodine receptor (RyR) clusters (green) in CRT tissue. **B** and **C**, Zoom-ins from the region indicated by the white rectangle. RyR and t-system remodeling are less pronounced than in dyssynchronous heart failure (DHF). **D–F**, 3D visualizations of 4-µm-thick sections through an example CRT cell. Longitudinal section (**D**), transverse section 5 µm from cell end (**E**), and transverse section 40 µm from cell end (**F**). Red bars indicate section planes; Blue, sarcolemma; and Green and red spheres, RyR clusters. Clusters of high intensity (90th percentile) are shown in red. All scale bars: 10 µm. Scale bar in **B** applies to **C**. Scale bar in **E** applies to **F**. Analysis of mean intracellular voxel distance to the nearest sarcolemma (**G**), mean RyR cluster distance to nearest sarcolemma (**H**), RyR cluster density (**I**), and RyR intensity per volume normalized to mean value of the whole cell (**J**).

the Data Supplement). This indicates that RyR remodeling is independent of t-system remodeling in anterior cells.

Preserved T-System and Marginal RyR Remodeling in SHF

To investigate the role of dyssynchrony in remodeling, we analyzed lateral cells from animals in SHF induced by right atrial pacing. Cells from this group did not show t-system remodeling or changes in the relationship between t-system and RyRs versus control (Figures IX and X in the Data Supplement). However, we found changes in RyR intensity as observed in DHF, although to a lesser degree. RyR intensity at cell ends was higher than at cell centers in SHF.

Subcellular Heterogeneity of Ca^{2+} Sparks

To investigate whether subcellular heterogeneity of structural remodeling was associated with heterogeneity of Ca^{2+} release events, we acquired Fluo-4 images from isolated myocytes using rapid scanning confocal microscopy. Processing of the Fluo-4 images (Figure 7A) enabled the detection of Ca^{2+} release events during the diastolic phase of ventricular myocytes. We applied filtering, attenuation correction, and pixel-wise self-ratioing on the image data to improve signal quality. Results of this processing are presented for a single pixel (Figure 7B and 7C) and region with a spontaneous Ca^{2+} release event (Figure 7D and 7E). In Figure 7F–7H, we present detected sparks localized in the Di-8-Anepps images. We detected the cell orientation and the most distal point of the cell. This enabled the creation of distance maps from the cell end. Subsequently, specific regions of interest at varying distances were compared. Figures 7F, 7G, and 7H show the investigated regions and centroids of detected sparks mapped onto the Di-8-Anepps images of an exemplary control, DHF, and CRT cells, respectively. Example Fluo-4 and Di-8-Anepps images of these cells are presented in Figures II and III in the Data Supplement. Videos I, II, and III in the Data Supplement illustrate the raw and processed Fluo-4 image sequences in control, DHF, and CRT cells, respectively. Although spark density was homogeneously distributed in the control and CRT cell, the DHF cell exhibited a reduced spark density at the end versus center.

Using this approach, we performed a statistical analysis of sparks in control, DHF, and CRT cells bathed in modified Tyrode's solution containing either 2 or 4 mmol/L Ca^{2+} (Figure 8; Figure XI in the Data Supplement). We did not find significant changes in overall spark density for cells in either 2 or 4 mmol/L Ca^{2+} (Figure 8A and 8B). However, cells from DHF animals exhibited a significantly lower spark density in regions 0 to 10 µm versus 10 to 40 µm from cell ends. This heterogeneity was not visible in cells from either control or CRT animals (Figure 8D and 8E), indicating restoration of homogeneity of sparks after CRT.

Discussion

Our study revealed previously unknown subcellular heterogeneity of structural and functional remodeling in ventricular myocytes in HF. 3D analysis of confocal microscopic images

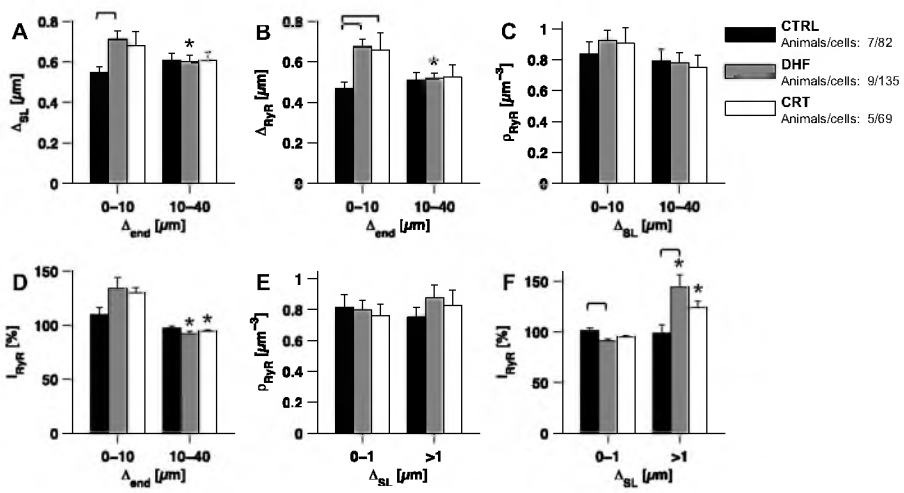

Figure 6. Statistical analysis of myocytes from control (CTRL), dyssynchronous heart failure (DHF), and cardiac resynchronization therapy (CRT) animals. Error bars indicate standard errors of the mean. Parameters were analyzed 0 to 10 μm and 10 to 40 μm from the cell end. **A**, Mean intracellular voxel distance to nearest sarcolemma. **B**, Mean ryanodine receptor (RyR) cluster distance to nearest sarcolemma. **C**, RyR cluster density. **D**, RyR intensity per volume normalized to mean intensity of the whole cell. Parameters were analyzed 0 to 1 μm and ≥1 μm from the sarcolemma. RyR cluster density (**E**) and RyR intensity per volume normalized to mean value of the whole cell (**F**). Brackets mark statistical significance between experimental groups, asterisks between corresponding bins of groups.

of tissue sections from DHF myocytes indicated that t-system density and RyR distribution is heterogeneous at the subcellular scale. Both DHF and SHF cells showed heterogeneous RyR distributions, but only lateral DHF myocytes exhibited t-system depletion at cell ends. The t-system was not affected in anterior DHF and lateral SHF myocytes. In subsequent studies using rapid scanning confocal microscopy, we found that the subcellular heterogeneity of t-system and RyR distribution is associated with heterogeneous Ca^{2+} spark densities. After CRT, subcellular homogeneity of structures and function was, in part, restored.

Our finding of subcellular heterogeneity of the density of RyRs in HF is novel. Our studies revealed increased density and fluorescence intensity of RyR clusters at cell ends versus cell centers in DHF and SHF. In both HF models, the intensity of RyR clusters not associated with sarcolemma was higher than that proximal to sarcolemma. This effect of HF was not restricted to cell ends (Figure VIA in the Data Supplement), but also occurred in cell centers (Figure VIB in the Data Supplement). In contrast, in control cells, the intensity of RyR clusters was not affected by the distance to sarcolemma. This suggests that differences in optical properties or immunostaining do not underlie heterogeneous RyR intensities found in DHF cells. Instead, our study indicates that in HF cells, the number of RyR channels is higher in nonjunctional clusters than in couplons. Accordingly, RyR distribution along the longitudinal cell

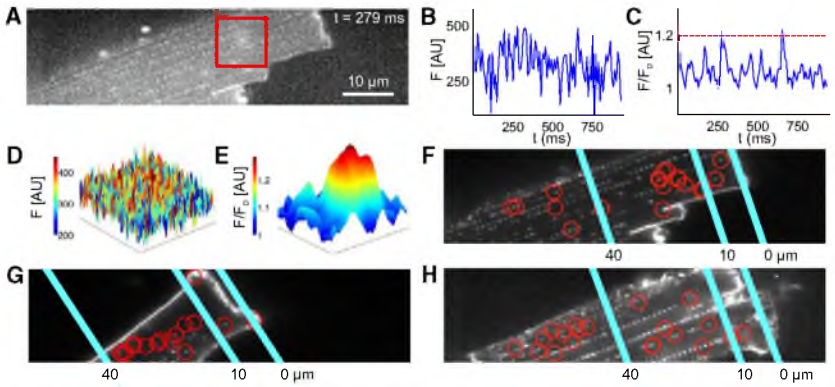

Figure 7. Analysis of subcellular heterogeneity of diastolic Ca^{2+} sparks using rapid scanning confocal microscopy. **A**, Representative Fluo-4 images from control cell with a spark marked by the red box. **B**, Trace of Fluo-4 signal over time for pixel located at center of red box marked in **A**. **C**, Trace of processed Fluo-4 signal in **B**. **D**, Image of Fluo-4 signal in region outlined by red box in **A**. **E**, Processed image of region in **E**. **F–H**, Di-8-Anepps images overlaid with red circles centered on all detected sparks. **F**, Control cell with a spark density of 0.020 sparks/s/μm^2 near the end and 0.0253 sparks/s/μm^2 in the center of the cell. **G**, Dyssynchronous heart failure (DHF) cell with a spark density of 0.0227 sparks/s/μm^2 near end and 0.0418 sparks/s/μm^2 in the center of the cell. **H**, Cardiac resynchronization therapy (CRT) cell with spark density 0.0166 sparks/s/μm^2 near the end and 0.0167 sparks/s/μm^2 in the center of the cell.

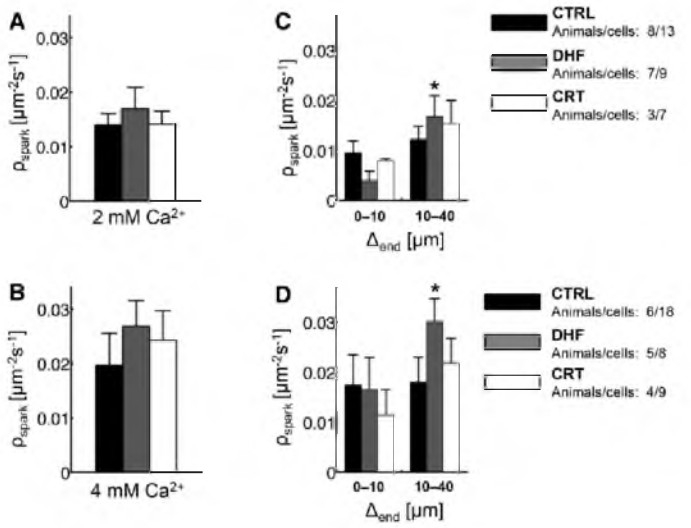

Figure 8. Statistical analyses of diastolic spark density. Overall spark density in control (CTRL), dyssynchronous heart failure (DHF), and cardiac resynchronization therapy (CRT) cells in a bathing solution containing 2 mmol/L (**A**) and 4 mmol/L (**B**) Ca^{2+} was similar. Analysis of spark density with regions <10 μm and between 10 and 40 μm from the cell end in a bathing solution containing 2 mmol/L (**C**) and 4 mmol/L (**D**) Ca^{2+} revealed subcellular heterogeneity in DHF cells. Asterisks mark statistical significance between corresponding bins of groups.

axis was especially heterogeneous in lateral DHF cells. Cell ends, where t-system density was low, presented a higher percentage of nonjunctional RyR clusters. Because these clusters exhibited increased intensity, the overall RyR intensity at cell ends was increased. In agreement with this finding, SHF and anterior DHF cells exhibited an increase of RyR intensity ≥1 μm from the sarcolemma, although the t-system was normal (Figures VIII and X in the Data Supplement). This suggests that RyR remodeling is associated with rapid pacing underlying our HF models. However, subcellular heterogeneity of RyR signal intensity was higher in DHF than in SHF, indicating that ventricular dyssynchrony exacerbates the remodeling.

Previously, significant reduction of RyR mRNA and protein expression has been reported in LV myocytes from DHF and CRT animals.[10] The reduction was found in both anterior and lateral cells. Our analysis of RyR-associated fluorescence revealed an ≈40% increase of RyR expression at ends versus centers of lateral DHF cells (134±10% versus 92±2%; Figure 6D). Assuming an overall decrease of RyR protein expression in DHF lateral cells by ≈20%,[10] this would translate into an increase of RyR expression to 107% at cell ends and a decrease to 74% at cell centers versus control. Similarly, RyR reduction in DHF cells can be explained by reduction of junctional RyRs (Figure 6F). Our data suggest that RyR protein expression is reduced to 73% within 0 to 1 μm and increased to 115% in regions ≥1 μm from the sarcolemma. This reduced RyR expression within 0 to 1 μm from the sarcolemma may reflect decreased junction size, which was suggested to underlie delayed stochastic couplon activation and reduced amplitude of Ca^{2+} transients.[34]

It is well established that t-system depletion is a feature of HF. Our previous study on isolated ventricular myocytes suggested regional heterogeneity of t-system depletion. In particular, this study indicated that t-system depletion is pronounced in the lateral LV region in DHF, but we did not investigate subcellular heterogeneity of t-system depletion. However, it has been observed in isolated cells that t-system depletion in tachypacing-induced HF occurs preferentially at cell ends.[23,24] In agreement with those studies, remodeling of t-system in our DHF model seems to be regional and restricted to ends of myocytes. These findings indicate that ventricular dyssynchrony is a major contributor of this type of regional subcellular remodeling.

Previously, we found reduced amplitudes and slowed decays of Ca^{2+} transients in DHF myocytes and restoration after CRT to levels similar as in control.[10,11] In this study, we provide insights into structural subcellular heterogeneity in DHF, which may underlie these alterations. According to our recent model of Ca^{2+} release,[35] the detubulation and increase in nonjunctional RyRs at cell ends would cause heterogeneous Ca^{2+} transients in DHF cells, in particular delayed onset times at ends versus centers of cells. This hypothesis is supported by a preliminary analysis of a DHF cell (Data Supplement). The analysis also suggests reduced amplitude of the Ca^{2+} transients at cell ends as a further effect of heterogeneous microstructural remodeling in DHF.

Because diastolic Ca^{2+} sparks have been linked to arrhythmogenesis,[36] we investigated whether diastolic sparks are affected by the structural heterogeneity in DHF cells. Spark densities in control and CRT cells were homogeneous, but in DHF, spark density was lower at cell ends than in cell centers. This agrees with a previous study in which regions void of t-tubules lacked sparks in normal and failing canine myocytes.[37] Possible causes of subcellular heterogeneity of spark density include heterogeneous SR Ca^{2+} load and different spark probabilities of junctional and nonjunctional RyR clusters. Interestingly, increased RyR density at cell ends was not associated with increased spark density. Instead spark density was increased in regions with intact t-system and, thus, high ratio of junctional to nonjunctional RyRs. A potential explanation for increased spark probability in couplons is that spontaneous Ca^{2+} releases from junctional RyRs into the dyadic cleft have a higher probability of triggering neighboring RyRs than Ca^{2+} release from nonjunctional RyRs into the cytosol. Overall spark density was modulated by bath Ca^{2+} concentration, which can be explained by a positive relationship between bath Ca^{2+} concentration, SR Ca^{2+} load, and spontaneous spark probability. However, our study did not indicate significant differences of overall spark density in control, DHF, and CRT cells. This

suggests that increased spark density in centers of DHF cells is counterbalanced by reduced spark density at cell ends.

Although our studies revealed striking subcellular remodeling and restoration, the underlying mechanisms remain unclear. A potential mechanism is related to heterogeneity of mechanical properties of cardiac myocytes and their strain profiles during a heartbeat. We previously proposed that changes in strain profiles directly affect t-system structure and maintenance.[11,38] Here we extend this hypothesis by suggesting that subcellular heterogeneity of strain profiles in myocytes leads to subcellular heterogeneous remodeling of t-system and RyRs. Based on principles of mechanics, for instance, Hooke's law,[39] we expect larger stretch in those regions of strained myocytes which have a smaller cross-sectional area. Indeed most cells taper toward their ends and thus have a smaller cross-sectional area at the end (eg, Figure 2). In the cell population of our study, cross-sectional areas within 10 μm from the cell end were reduced to 62.8±1.2% of central cross-sectional areas (within 10–40 μm from the cell end). An alternative explanation of subcellular heterogeneity of strain profiles is subcellular heterogeneity of myocyte stiffness. Hooke's law predicts larger stretch in those regions of strained myocytes which have a smaller stiffness.

It is well established that DHF is associated with contraction in anterior and septal sites, but reciprocal stretch in lateral sites during early systole.[10,32] Opposite strains occur during late systole. Stretch during early systole in lateral sites is significantly larger than that at end diastole. Based on our hypothesis, we expect that lateral LV myocytes are heterogeneously stretched during early systole, with pronounced stretch at the tapered cell ends that is larger than in the cell center. The pronounced stretch at the cell ends could directly destabilize t-system or interfere with its maintenance.

A similar argument based on mechanical principles can be made to suggest potential mechanisms for upregulation of RyRs at cell ends in SHF and DHF in the context of a general RyR downregulation in ventricular myocardium. Both SHF and DHF are associated with increased LV end diastolic blood pressure.[11] Based on our new hypothesis, we expect that ventricular myocytes in SHF and DHF are heterogeneously stretched during diastole, with larger stretch at the tapered cell ends than in the cell center. We speculate that the increased stretch at cell ends provides a signal for local upregulation of RyR expression. Alternatively, the locally increased stretch might interfere with protein degradation.

Limitations

Limitations of our animal models have been explained previously.[10,11,13] Further limitations related to confocal microscopy, image analysis, and tissue preparation are summarized in the Data Supplement.

Sources of Funding

The study has been supported by National Institutes of Health grants R01 HL094464 (Dr Sachse) and PO1 HL077180 (Dr Tomaselli) and awards from the Nora Eccles Treadwell Foundation (Dr Bridge and Dr Sachse). We acknowledge funding by the American Heart Association grant 14POST19820010 (Dr Seidel). We thank Mrs Deborah DiSilvestre, Mr Robin Moss, Mrs Jayne Davis, Mrs Nancy Allen, and Mr Chris Hunter for expert technical assistance. We thank Drs David A. Kass, Kenneth W. Spitzer, and Natalia Torres for useful discussions. We acknowledge support of this project by the Medtronic device donation program facilitated by Dr Brian Neudeck and Mr Patrick Collins. We thank Dr Greg Stoddard, Study Design and Biostatistics Center, University of Utah, for advice on statistical analyses and data presentation.

Disclosures

None.

References

1. Blanc JJ, Etienne Y, Gilard M, Mansourati J, Munier S, Boschat J, Benditt DG, Lurie KG. Evaluation of different ventricular pacing sites in patients with severe heart failure: results of an acute hemodynamic study. *Circulation*. 1997;96:3273–3277. doi: 10.1161/01.CIR.96.10.3273.
2. Kass DA, Chen CH, Curry C, Talbot M, Berger R, Fetics B, Nevo E. Improved left ventricular mechanics from acute VDD pacing in patients with dilated cardiomyopathy and ventricular conduction delay. *Circulation*. 1999;99:1567–1573. doi: 10.1161/01.CIR.99.12.1567.
3. Auricchio A, Klein H, Tockman B, Sack S, Stellbrink C, Neuzner J, Kramer A, Ding J, Pochet T, Maarse A, Spinelli J. Transvenous biventricular pacing for heart failure: can the obstacles be overcome? *Am J Cardiol*. 1999;83(5B):136D–142D.
4. Nelson GS, Berger RD, Fetics BJ, Talbot M, Spinelli JC, Hare JM, Kass DA. Left ventricular or biventricular pacing improves cardiac function at diminished energy cost in patients with dilated cardiomyopathy and left bundle-branch block. *Circulation*. 2000;102:3053–3059. doi: 10.1161/01.CIR.102.25.3053.
5. Abraham WT, Fisher WG, Smith AL, Delurgio DB, Leon AR, Loh E, Kocovic DZ, Packer M, Clavell AL, Hayes DL, Ellestad M, Trupp RJ, Underwood J, Pickering F, Truex C, McAtee P, Messenger J; MIRACLE Study Group. Multicenter InSync Randomized Clinical Evaluation. Cardiac resynchronization in chronic heart failure. *N Engl J Med*. 2002;346:1845–1853. doi: 10.1056/NEJMoa013168.
6. Cleland JG, Daubert JC, Erdmann E, Freemantle N, Gras D, Kappenberger L, Tavazzi L. Longer-term effects of cardiac resynchronization therapy on mortality in heart failure [the CArdiac REsynchronization-Heart Failure (CARE-HF) trial extension phase]. *Eur Heart J*. 2006;27:1928–1932. doi: 10.1093/eurheartj/ehl099.
7. Cleland JG, Daubert JC, Erdmann E, Freemantle N, Gras D, Kappenberger L, Tavazzi L; Cardiac Resynchronization-Heart Failure (CARE-HF) Study Investigators. The effect of cardiac resynchronization on morbidity and mortality in heart failure. *N Engl J Med*. 2005;352:1539–1549. doi: 10.1056/NEJMoa050496.
8. Bristow MR, Saxon LA, Boehmer J, Krueger S, Kass DA, De Marco T, Carson P, DiCarlo L, DeMets D, White BG, DeVries DW, Feldman AM; Comparison of Medical Therapy, Pacing, and Defibrillation in Heart Failure (COMPANION) Investigators. Cardiac-resynchronization therapy with or without an implantable defibrillator in advanced chronic heart failure. *N Engl J Med*. 2004;350:2140–2150. doi: 10.1056/NEJMoa032423.
9. Cazeau S, Leclercq C, Lavergne T, Walker S, Varma C, Linde C, Garrigue S, Kappenberger L, Haywood GA, Santini M, Bailleul C, Daubert JC; Multisite Stimulation in Cardiomyopathies (MUSTIC) Study Investigators. Effects of multisite biventricular pacing in patients with heart failure and intraventricular conduction delay. *N Engl J Med*. 2001;344:873–880. doi: 10.1056/NEJM200103223441202.
10. Aiba T, Hesketh GG, Barth AS, Liu T, Daya S, Chakir K, Dimaano VL, Abraham TP, O'Rourke B, Akar FG, Kass DA, Tomaselli GF. Electrophysiological consequences of dyssynchronous heart failure and its restoration by resynchronization therapy. *Circulation*. 2009;119:1220–1230. doi: 10.1161/CIRCULATIONAHA.108.794834.
11. Sachse FB, Torres NS, Savio-Galimberti E, Aiba T, Kass DA, Tomaselli GF, Bridge JH. Subcellular structures and function of myocytes impaired during heart failure are restored by cardiac resynchronization therapy. *Circ Res*. 2012;110:588–597. doi: 10.1161/CIRCRESAHA.111.257428.
12. Chakir K, Depry C, Dimaano VL, Zhu WZ, Vanderheyden M, Bartunek J, Abraham TP, Tomaselli GF, Liu SB, Xiang YK, Zhang M, Takimoto E, Dulin N, Xiao RP, Zhang J, Kass DA. Galphas-biased beta2-adrenergic receptor signaling from restoring synchronous contraction in the failing heart. *Sci Transl Med*. 2011;3:100ra88. doi: 10.1126/scitranslmed.3001909.

13. Lichter JG, Carruth E, Mitchell C, Barth AS, Aiba T, Kass DA, Tomaselli GF, Bridge JH, Sachse FB. Remodeling of the sarcomeric cytoskeleton in cardiac ventricular myocytes during heart failure and after cardiac resynchronization therapy. *J Mol Cell Cardiol*. 2014;72:186–195. doi: 10.1016/j.yjmcc.2014.03.012.
14. Stern MD, Pizarro G, Ríos E. Local control model of excitation-contraction coupling in skeletal muscle. *J Gen Physiol*. 1997;110:415–440. doi: 10.1085/jgp.110.4.415.
15. Franzini-Armstrong C, Protasi F, Ramesh V. Shape, size, and distribution of Ca(2+) release units and couplons in skeletal and cardiac muscles. *Biophys J*. 1999;77:1528–1539. doi: 10.1016/S0006-3495(99)77000-1.
16. Radermacher M, Rao V, Grassucci R, Frank J, Timerman AP, Fleischer S, Wagenknecht T. Cryo-electron microscopy and three-dimensional reconstruction of the calcium release channel/ryanodine receptor from skeletal muscle. *J Cell Biol*. 1994;127:411–423.
17. Fabiato A. Time and calcium dependence of activation and inactivation of calcium-induced release of calcium from the sarcoplasmic reticulum of a skinned canine cardiac Purkinje cell. *J Gen Physiol*. 1985;85:247–289.
18. Izu LT, William Balke C. The Ca2+ synapse redo: a matter of location, location, location. *Circ Res*. 2002;91:276–277.
19. Shacklock PS, Wier WG, Balke CW. Local Ca2+ transients (Ca2+ sparks) originate at transverse tubules in rat heart cells. *J Physiol*. 1995;487 (Pt 3):601–608.
20. Cheng H, Lederer WJ, Cannell MB. Calcium sparks: elementary events underlying excitation-contraction coupling in heart muscle. *Science*. 1993;262:740–744.
21. Wier WG, Egan TM, López-López JR, Balke CW. Local control of excitation-contraction coupling in rat heart cells. *J Physiol*. 1994;474:463–471.
22. Hasenfuss G. Alterations of calcium-regulatory proteins in heart failure. *Cardiovasc Res*. 1998;37:279–289.
23. Balijepalli RC, Lokuta AJ, Maertz NA, Buck JM, Haworth RA, Valdivia HH, Kamp TJ. Depletion of T-tubules and specific subcellular changes in sarcolemmal proteins in tachycardia-induced heart failure. *Cardiovasc Res*. 2003;59:67–77.
24. He J, Conklin MW, Foell JD, Wolff MR, Haworth RA, Coronado R, Kamp TJ. Reduction in density of transverse tubules and L-type Ca(2+) channels in canine tachycardia-induced heart failure. *Cardiovasc Res*. 2001;49:298–307.
25. Wei S, Guo A, Chen B, Kutschke W, Xie YP, Zimmerman K, Weiss RM, Anderson ME, Cheng H, Song LS. T-tubule remodeling during transition from hypertrophy to heart failure. *Circ Res*. 2010;107:520–531. doi: 10.1161/CIRCRESAHA.109.212324.
26. Heinzel FR, Bito V, Biesmans L, Wu M, Detre E, von Wegner F, Claus P, Dymarkowski S, Maes F, Bogaert J, Rademakers F, D'hooge J, Sipido K. Remodeling of T-tubules and reduced synchrony of Ca2+ release in myocytes from chronically ischemic myocardium. *Circ Res*. 2008;102:338–346. doi: 10.1161/CIRCRESAHA.107.160085.
27. Lyon AR, Nikolaev VO, Miragoli M, Sikkel MB, Paur H, Benard L, Hulot JS, Kohlbrenner E, Hajjar RJ, Peters NS, Korchev YE, Macleod KT, Harding SE, Gorelik J. Plasticity of surface structures and β(2)-adrenergic receptor localization in failing ventricular cardiomyocytes during recovery from heart failure. *Circ Heart Fail*. 2012;5:357–365. doi: 10.1161/CIRCHEARTFAILURE.111.964692.
28. Ibrahim M, Navaratnarajah M, Siedlecka U, Rao C, Dias P, Moshkov AV, Gorelik J, Yacoub MH, Terracciano CM. Mechanical unloading reverses transverse tubule remodelling and normalizes local Ca(2+)-induced Ca(2+)release in a rodent model of heart failure. *Eur J Heart Fail*. 2012;14:571–580. doi: 10.1093/eurjhf/hfs038.
29. Spragg DD, Akar FG, Helm RH, Tunin RS, Tomaselli GF, Kass DA. Abnormal conduction and repolarization in late-activated myocardium of dyssynchronously contracting hearts. *Cardiovasc Res*. 2005;67:77–86. doi: 10.1016/j.cardiores.2005.03.008.
30. Spragg DD, Leclercq C, Loghmani M, Faris OP, Tunin RS, DiSilvestre D, McVeigh ER, Tomaselli GF, Kass DA. Regional alterations in protein expression in the dyssynchronous failing heart. *Circulation*. 2003;108:929–932. doi: 10.1161/01.CIR.0000088782.99568.CA.
31. Leclercq C, Faris O, Tunin R, Johnson J, Kato R, Evans F, Spinelli J, Halperin H, McVeigh E, Kass DA. Systolic improvement and mechanical resynchronization does not require electrical synchrony in the dilated failing heart with left bundle-branch block. *Circulation*. 2002;106:1760–1763.
32. Chakir K, Daya SK, Tunin RS, Helm RH, Byrne MJ, Dimaano VL, Lardo AC, Abraham TP, Tomaselli GF, Kass DA. Reversal of global apoptosis and regional stress kinase activation by cardiac resynchronization. *Circulation*. 2008;117:1369–1377. doi: 10.1161/CIRCULATIONAHA.107.706291.
33. Seidel T, Drabing T, Seemann G, Sachse FB. A semi-automatic approach for segmentation of three-dimensional microscopic image stacks of cardiac tissue. In: Ourselin S, Rueckert D, and Smith N eds. *Functional Imaging and Modeling of the Heart*. Lecture Notes in Computer Science. *Vol. 7945*. Berlin Heidelberg: Springer; 2013:300–307.
34. Wu HD, Xu M, Li RC, Guo L, Lai YS, Xu SM, Li SF, Lü QL, Li LL, Zhang HB, Zhang YY, Zhang CM, Wang SQ. Ultrastructural remodelling of Ca(2+) signalling apparatus in failing heart cells. *Cardiovasc Res*. 2012;95:430–438. doi: 10.1093/cvr/cvs195.
35. Torres NS, Sachse FB, Izu LT, Goldhaber JI, Spitzer KW, Bridge JH. A modified local control model for Ca2+ transients in cardiomyocytes: junctional flux is accompanied by release from adjacent non-junctional RyRs. *J Mol Cell Cardiol*. 2014;68:1–11. doi: 10.1016/j.yjmcc.2013.12.019.
36. Cheng H, Lederer WJ. Calcium sparks. *Physiol Rev*. 2008;88:1491–1545. doi: 10.1152/physrev.00030.2007.
37. Meethal SV, Potter KT, Redon D, Munoz-del-Rio A, Kamp TJ, Valdivia HH, Haworth RA. Structure-function relationships of Ca spark activity in normal and failing cardiac myocytes as revealed by flash photography. *Cell Calcium*. 2007;41:123–134. doi: 10.1016/j.ceca.2006.05.006.
38. McNary TG, Spitzer KW, Holloway H, Bridge JH, Kohl P, Sachse FB. Mechanical modulation of the transverse tubular system of ventricular cardiomyocytes. *Prog Biophys Mol Biol*. 2012;110:218–225. doi: 10.1016/j.pbiomolbio.2012.07.010.
39. Bathe KJ. *Finite Element Procedures*. Englewood Cliffs, N.J.: Prentice Hall; 1996.

CLINICAL PERSPECTIVE

Cardiac resynchronization therapy (CRT) is an established clinical therapy for patients with dyssynchronous heart failure. Previous studies demonstrated remodeling of microscopic structure and function in dyssynchronous heart failure and their partial restoration in response to CRT. In this work, we introduce the novel concept of subcellular heterogeneity to describe the detrimental effects of dyssynchronous heart failure on subcellular structure and function of ventricular myocytes. We studied the spatial distribution of the transverse tubular system and sarcoplasmic calcium release channels, ryanodine receptors (RyRs), and spontaneous calcium sparks to investigate whether structural heterogeneity is accompanied by functional heterogeneity. Three-dimensional analyses of confocal microscopic images of myocytes from left ventricular tissue sections indicate that dyssynchronous heart failure, but not synchronous heart failure, produces heterogeneous subcellular distribution of both the transverse tubular system and ryanodine receptors. We found that these structural subcellular heterogeneities are associated with heterogeneous calcium spark distributions. Our studies further revealed that CRT efficiently reduces subcellular heterogeneity of structure and function. We therefore suggest that altered strain profiles of myocytes caused by ventricular dyssynchrony may underlie the observed subcellular heterogeneous remodeling of structures and function. Furthermore, our studies indicate that restoring ventricular synchrony by CRT reduces these heterogeneities, which we think underlies the improvements of heart function observed in CRT patients.

Supplemental Material

Supplemental Methods

Monitoring of Animal Models

After device implantation weekly ECGs were obtained to ensure correct lead placement and capture of the pacing. Only animals with increased QRS duration after DHF and decreased QRS duration after CRT were used for our studies (Supplemental Table I).

Tissue Collection and Cell Isolation

Animals were anesthetized by propofol injection and isoflurane inhalation. Hearts were excised quickly and perfused retrogradely through the aorta for 10 min with Ca^{2+} free modified Tyrode's solution comprising (in mM) NaCl 92, KCl 4.4, $MgCl_2$ 5, NaH_2PO4 5, D-glucose 11, HEPES 24, NaOH 12.5, Taurine 20, Creatine 5, Na Pyruvate 1. Tissue samples were collected from the subepicardial anterior and lateral LV free wall. Tissue samples were flash-frozen in Tissue-Tek Cryo-Oct compound (ThermoFisher Scientific, Waltham, MA, USA). Cardiac cells were isolated by perfusion of Ca^{2+} free modified Tyrode's solution containing Collagenase P (0.1-0.2 mg/ml, Roche Diagnostics, Indianapolis, IN, USA) and Protease Type XIV (0.06 mg/ml, Sigma-Aldrich, St. Louis, MO, USA). Once an acceptable degree of tissue dissociation was reached digestion was stopped by wash out with the modified Tyrode's solution containing 50 µM Ca^{2+}. Tissue from anterior and lateral LV were collected separately and manually chopped into small pieces. These samples were then gently shaken in a beaker at 37°C for 10 min. To remove undigested tissue chunks, cell solutions were filtered through a strainer. After 10-20 min the Ca^{2+} concentration was increased from 50 µM to 1 mM in 4 steps over 24 min.

Tissue Sectioning and Labeling

Tissue samples were sectioned into 80 µm slices using a cryostat (Leica Biosystems, CM1950, Buffalo Grove, IL, USA). The slices were fixed using 2% paraformaldehyde in phosphate buffered saline solution (PBS) for 30 min and then rinsed with PBS twice. Sarcolemma, t-tubules and the interstitial space were labeled by incubation of the tissue with wheat germ agglutinin (WGA) conjugated to Alexa Fluor 555 (Invitrogen, Carlsbad, CA, USA) at 30 µg/ml at room temperature overnight. The tissue sections were then rinsed 3 times with PBS and permeabilized with 0.3% Triton X-100 (Sigma-Aldrich, St. Louis, MO, USA) for 2 h. Signal enhancer (Invitrogen) was applied to the tissue sections for 30 min. Tissue slices were incubated with blocking solution (0.05% Triton X-100, 4% goat serum in PBS) for 1 h to reduce unspecific labeling. RyRs were labeled with a monoclonal antibody (1:100, MA3-916, ThermoFisher Scientific, Waltham, MA, USA) in incubation solution (2% BSA, 2% goat serum, 0.05% TritonX-100 in PBS) overnight followed by incubation of a secondary antibody attached to Alexa Fluor 488 (1:100, A-11001, Invitrogen) in blocking solution overnight. Tissue sections were rinsed with PBS 3 times after each labeling procedure.

Isolated Cell Labeling

Ventricular myocytes were isolated, labeled with WGA and fixed as previously described.[1] The cells were permeabilized by application of 0.3% Triton-X in PBS for 20 min. After washing with PBS, signal enhancer (Invitrogen) was applied for 30 min. After washing with PBS, blocking was performed by incubation for 1 h in PBS containing 10% goat serum. Cells were then incubated with a primary antibody against NCX (1:100, MA3-926, ThermoFisher Scientific) diluted in incubation solution (2% BSA, 2% goat serum, 0.05% TritonX-100 in PBS) overnight at 4°C.

Cells were washed with PBS and then incubated with a secondary antibody attached to Alexa Fluor 633 (1:100, A-21046, Invitrogen). Cells were washed with PBS and then imaged in the same manner as tissue sections. A washing step consisted of removal of supernatant, application of PBS and allowing cells to settle for 15 min. Washing steps were repeated at least 3 times.

Analysis of T-System and RyR Clusters in 3D Image Stacks

Processing of the WGA and RyR image stacks involved noise reduction, deconvolution and background adjustment. Noise was reduced in WGA and RyR image stacks by applying a Gaussian (5x5x5 voxels, $\sigma = \sigma_y = \sigma_z = 0.1$ µm) and mean filter (6 neighbors), respectively. Subsequently, images were deconvolved with the Richardson-Lucy algorithm using measured point spread functions as described previously.[1, 2] Finally, the mode in the histogram of image intensities was identified as background intensity and adjusted to 256.

After this processing, the interstitial space was segmented from the WGA image stacks by applying a threshold of mode plus one standard deviation. Single, non-connected voxels were considered as noise and removed. RyR clusters were segmented in the RyR image stacks using a threshold of mode plus four standard deviations. The segmented WGA images served as mask for semi-automatic segmentation of individual cells based on a recently published method.[3] In short, seeds for a morphological watershed were iteratively created on the distance map of the segmented WGA images followed by manual merging of intracellular segments.

Only cells with a long axis angle smaller than 20° to the xy plane were selected for analyses. Cells without visible longitudinal end or a visible length of < 40 µm as well as cells showing signs of contracture were excluded. Segmented cells were used as masks to analyze RyR clusters and sarcolemma (including t-tubules). A bounding box was calculated for each cell to determine the distance from the longitudinal cell end of each voxel. Cells were divided into two regions: 0-10 µm and 10-40 µm from the cell end. Assuming a minimum myocyte length of ≈80 µm, regions further than 40 µm from the end were not included in the analyses because most cells were not captured completely due to limited image size (102.4 µm × 102.4 µm). To account for depth-dependent attenuation in confocal microscopy, analysis was restricted to the first 12 µm from the tissue surface.

Analysis of each segmented RyR cluster yielded sum of intensity and intensity-weighted centroid position. To determine the nearest sarcolemma distance we used distance maps (Supplemental Figure I). RyR clusters with intensities higher than 90% of all clusters in the same cell (90^{th} percentile) were defined as high-intensity clusters. RyR cluster density was calculated by dividing the number of clusters by the volume of interest, i.e. 0-10 µm and 10-40 µm from the cell end or 0-1 µm and >1 µm from the nearest sarcolemma. Total RyR intensity in these regions was calculated by summing up the intensity of segmented clusters. As a measure of t-system density, we calculated the mean distance of intracellular voxels to the nearest sarcolemma. Accordingly, high and low distances indicate low and high t-system densities, respectively.

For 3D visualizations of cells, we used ParaView (Kitware, Clifton Park, NY, USA). RyR clusters were displayed as spheres.

We performed analyses to investigate differences of the two different DHF model used in this study. Comparison of cells from animal models based on left bundle branch ablation or RV pacing did not reveal differences of t-system, the t-system-RyR relationship and the normalized

RyR intensity at cell ends/centers (Supplemental Figure XII). For subsequent structural analyses of DHF cells, we pooled data from the two DHF models.

Analysis of Ca^{2+} Spark Density in 2D Image Sequences

The cell membrane was detected using the Di-8-Anepps images (Supplemental Figure IIA). The images were filtered using a Gaussian mask (10 x 10 pixels, $\sigma = \sigma_y = 0.2$ µm). The resulting image was segmented using a threshold of mode plus twice the standard deviation of the image intensities. A morphological closing operator was used to fill holes in the image and obtain a mask of the entire cell (Supplemental Figure IIC). These cell masks were then visually inspected for each cell and adjusted manually for images with poor quality. For subsequent processing, mode and standard deviation were calculated only for the regions contained by this cell mask.

We created distance maps to the cell end by manually selecting the most distal point of the cell. Cell orientation was automatically detected and adjusted when necessary. A line through this point and perpendicular to cell orientation was used as the zero distance marker. The distance of each pixel to this line was then calculated. The distance mask was used for the subsequently described analysis of subcellular heterogeneity of spark density.

Sparks were detected after preprocessing of the Fluo-4 images (Supplemental Figure IIB). Preprocessing of these images included noise removal and bleaching correction. Low-frequency noise was removed by filtering in the frequency domain. High-frequency noise in the images was reduced by filtering with a discretized Gaussian function (25 x 25 pixels, $\sigma = \sigma_y = 0.5$ µm). Bleaching correction was performed by fitting a mono-exponential function to the mode of each frame of the image sequences. The decay was inverted and used for correction of each frame (Supplemental Figure IID). Image sequences were then self-ratioed using a moving window minimum in which each pixel was divided by its minimum value from the 5 previous to the 5 following frames. Potential sparks were segmented in normalized images using a threshold of mode plus five times the standard deviation of the image. These potential regions were then filtered through a set of criteria including: spanning less than 5 frames (42 ms), having circularity greater than 0.5 but less than 2, a minimum area of 79 pixels (~0.5 µm radius), and a maximum intensity greater than the mean intensity of that frame in the non-normalized image. Circularity was defined as:

$$Circularity = \frac{P^2}{4\pi A}$$

with the perimeter *P* and the area *A*. These criteria were applied to the segmentation of the potential spark found in the frame where the maximum intensity of that potential spark occurred. Additionally, all images were inspected for motion artifacts, abnormal cell morphology or cell debris. If necessary, regions and frames of interest were manually selected in the image sequences. Spark detection for these cells was restricted to designated regions of interest.

An Example of the Analysis of Ca^{2+} Transients in 2D Image Sequences

To shed light on potential effects of subcellular micro-structural heterogeneity on EC coupling we performed an exemplary analysis on Ca^{2+} transients in two regions, end and center, of a left lateral myocyte from a DHF animal (Supplemental Figure XIIIA). Our approach is based on methods previously introduced by us[4] and detailed in section Methods. Image acquisition at a frame rate of 4.6 ms/frame was triggered at 35.4 ms before electrical stimulation of the cell. Two-dimensional Ca^{2+} transients at different time points are presented in Supplemental Figure XIIIB. After stimulation the cell exhibited a heterogeneous distribution of signal intensities with

higher intensities in the central region. The measurement of averaged raw signals in the end and central region revealed a delayed upstroke and reduced amplitude of the Ca^{2+} signal at the cell end versus center (Supplemental Figure XIIIC). We applied filtering and attenuation correction to improve image quality. We averaged and self-ratioed signals from the end and central region (Supplemental Figure XIIID), which confirmed our findings in the raw signals.

Limitations

We discussed limitations of confocal microscopy for studies of RyR cluster and t-system previously.[1, 2] A limitation of our imaging approach is that RyR cluster sizes are below the resolution limit of a conventional confocal microscope.[5-7] Segmented RyR clusters therefore appear elongated and larger than their actual size. Thus, an increase in RyR cluster density, i.e. decreased distances between clusters, may have caused detection of fewer, but larger clusters. However, the presented sum of RyR intensity is not affected by this limitation. Our results show that high RyR intensity correlated with high RyR cluster density suggesting only a negligible effect of apparent cluster merging.

We used mounted tissue sections for 3D imaging and image analyses. While this preparation might avoid issues with detubulation that can occur during cell isolation, there are several limitations. The mounting medium to embed tissue sections is based on glycerol, polyvinyl alcohol and water. Evaporation of water increases the refractive index leading to improved image quality. The volume loss may lead to shrinkage of the tissue and compression of tissue between the glass slides. However, average distances of RyRs to the nearest sarcolemma were similar as in our previous study with isolated cells embedded in aqueous solutions.[1] Our imaging and analysis approach did not account for nuclei in cardiac myocytes. In most cells the nucleus membrane was weakly labeled by WGA and visible, for instance, in Figure IIA. In cell centers, distances to the sarcolemma might be increased due to the presence of nuclei, which are devoid of t-tubules. The presence of nuclei together with the absence of transverse cell membrane might explain the marginal increase in sarcolemmal distance in the center of control cells (Figure VI). Nevertheless, all experimental groups were similarly affected by this issue and we do not expect that it impairs the ability of the developed approach to detect differences of subcellular remodeling between the experimental groups.

A potential limitation is related to our approach for labeling of the sarcolemma. While WGA conjugated fluorescent signals exhibited high colocalization with extracellular fluorescent signals in the t-system of control rabbit myocyte,[2] a previous study suggested deficiencies of WGA labeling for some components of the t-system in human myocytes explained by heterogeneous glycosylation within the t-system.[8] We used a dual labeling approach to investigate heterogeneity of glycosylation in our preparation and, in particular, if this heterogeneity explains the subcellular heterogeneity of t-system in our DHF model (Supplemental Figure XIV). Our investigation revealed a high degree of colocalization of WGA and NCX. We were not able to identify significant components of the t-system that are labeled by NCX only. Thus, in our preparations, WGA appears to be a reliable marker of t-system.

	QRS Duration (ms)
Control	44.67 ± 2.32
SHF	36.67 ± 1.23
DHF	81.78 ± 0.97 *
CRT-3 weeks	83.50 ± 2.97 *
CRT-6 weeks	44.00 ± 3.21

Supplemental Table I. QRS durations measured in control, SHF, DHF and CRT models. Measurements for the CRT animals were performed after 3 weeks of RV pacing (CRT-3 weeks) and after additional 3 weeks of resynchronization (CRT-6 weeks). Asterisks marks significance versus control.

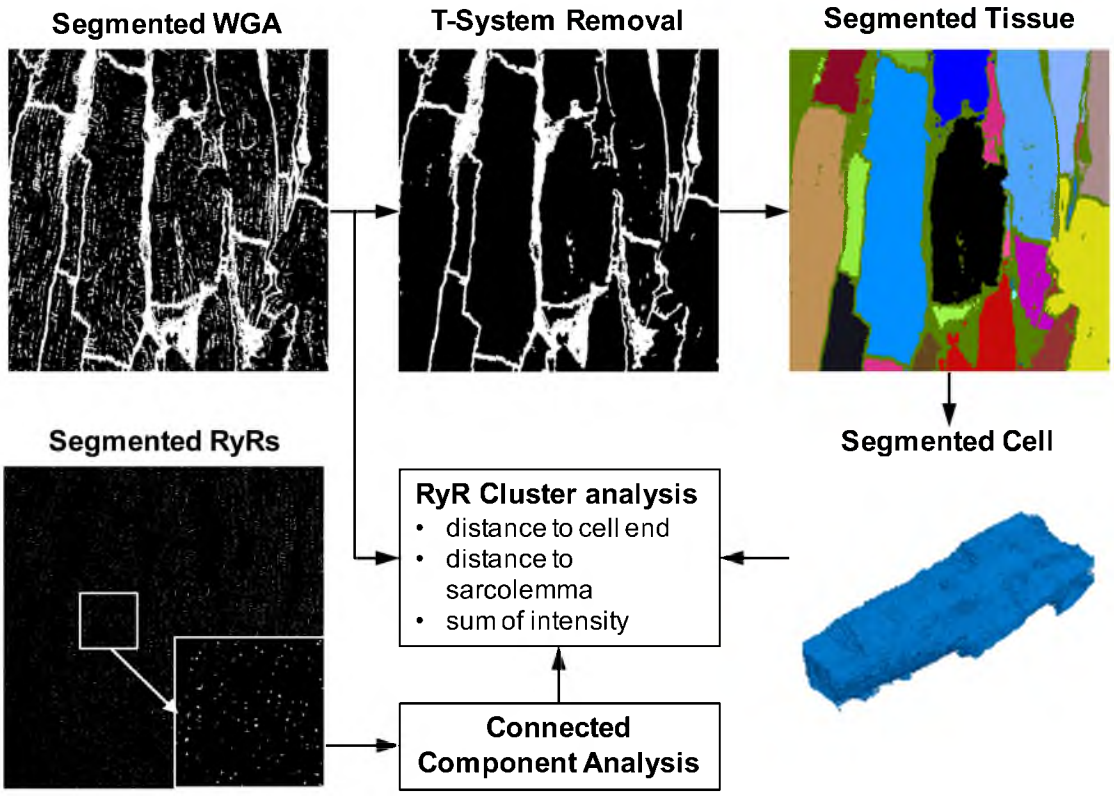

Supplemental Figure I. Processing of 3D image stacks from ventricular myocardium labeled with WGA and for RyRs. Image stacks were segmented using thresholds of mode+1 standard deviation and mode+4 standard deviation, respectively. Filtering removed the t-system from the WGA image allowing watershed-based segmentation of cells in the tissue. Segmented cells were extracted and used as masks for RyR analyses. Distance maps from the WGA images and connected component analysis of RyRs yielded their distances to cell end and sarcolemma as well as sum of RyR intensity.

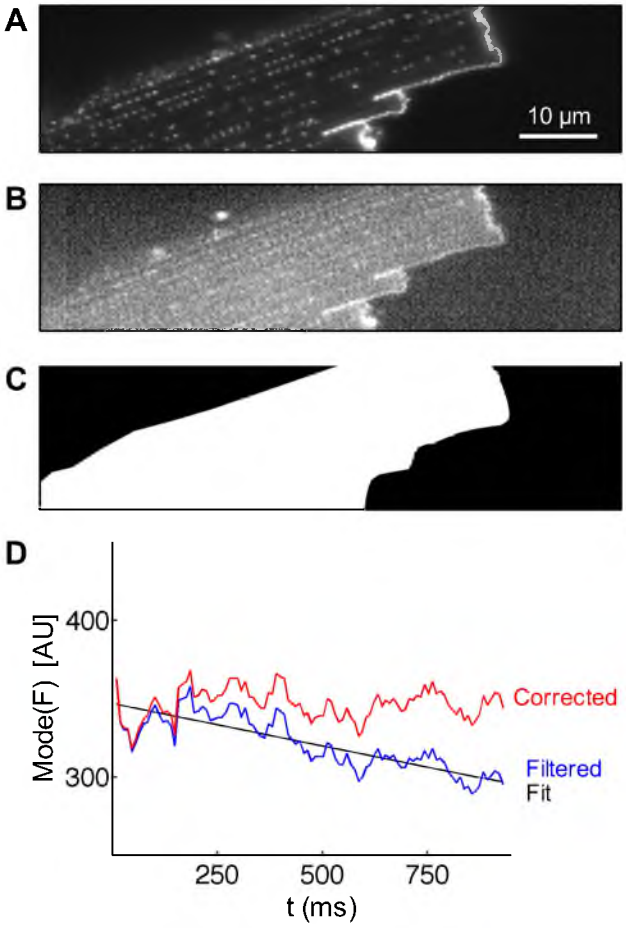

Supplemental Figure II. Processing of images from example control cell. (A) Raw Di-8-Anepps signal. (B) Raw Fluo-4 signal. (C) Automatically segmented cell. (D) Attenuation correction of Fluo-4 signals in each image. After application of a Gaussian filter (blue), a mono-exponential function was fitted to the mode of fluorescence intensity over time (black). The fit was used to correct for time-dependent attenuation (red).

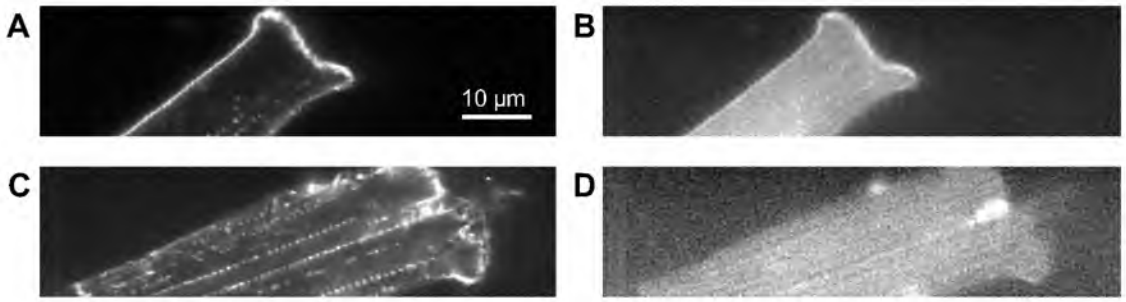

Supplemental Figure III. Example (A, C) Di-8-Anepps and (B,D) Fluo-4 images from a (A, B) DHF and (C,D) CRT cell.

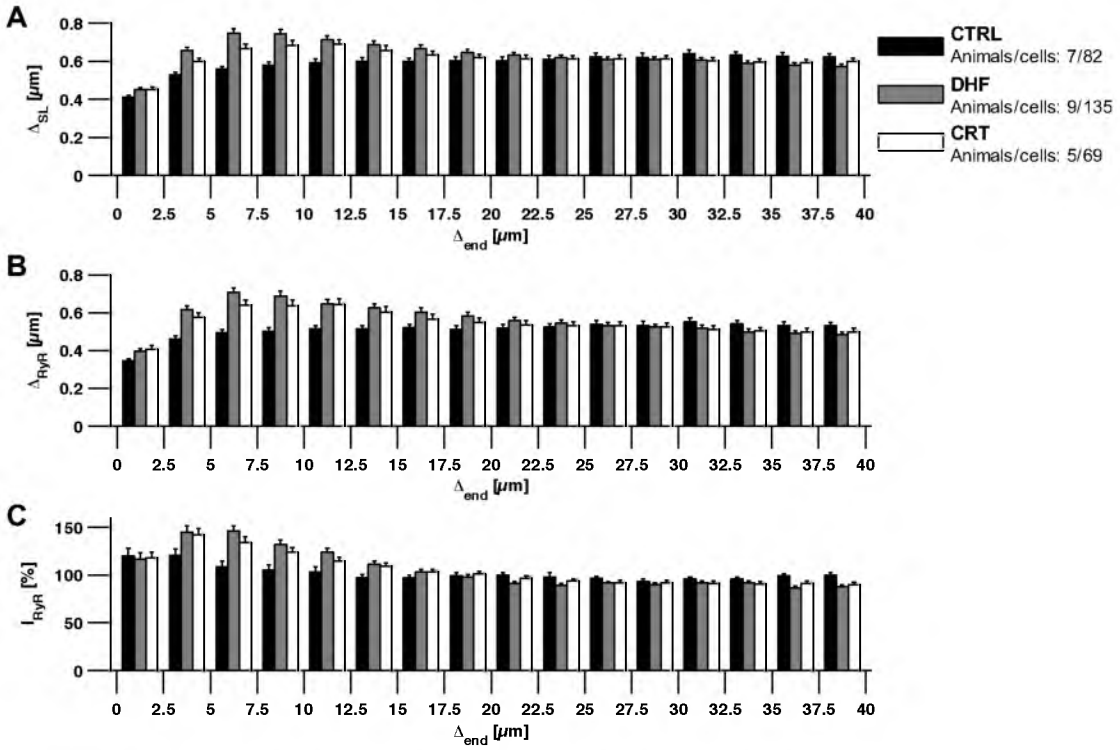

Supplemental Figure IV. Distribution along the cell long axis of (A) intracellular voxel distance to nearest sarcolemma, (B) RyR cluster distance to nearest sarcolemma, and (C) RyR intensity per volume normalized to mean value of the whole cell. Parameters were grouped in bins of 2.5 µm and with increasing distance from the cell end. Means and standard errors were calculated from all analyzed cels.

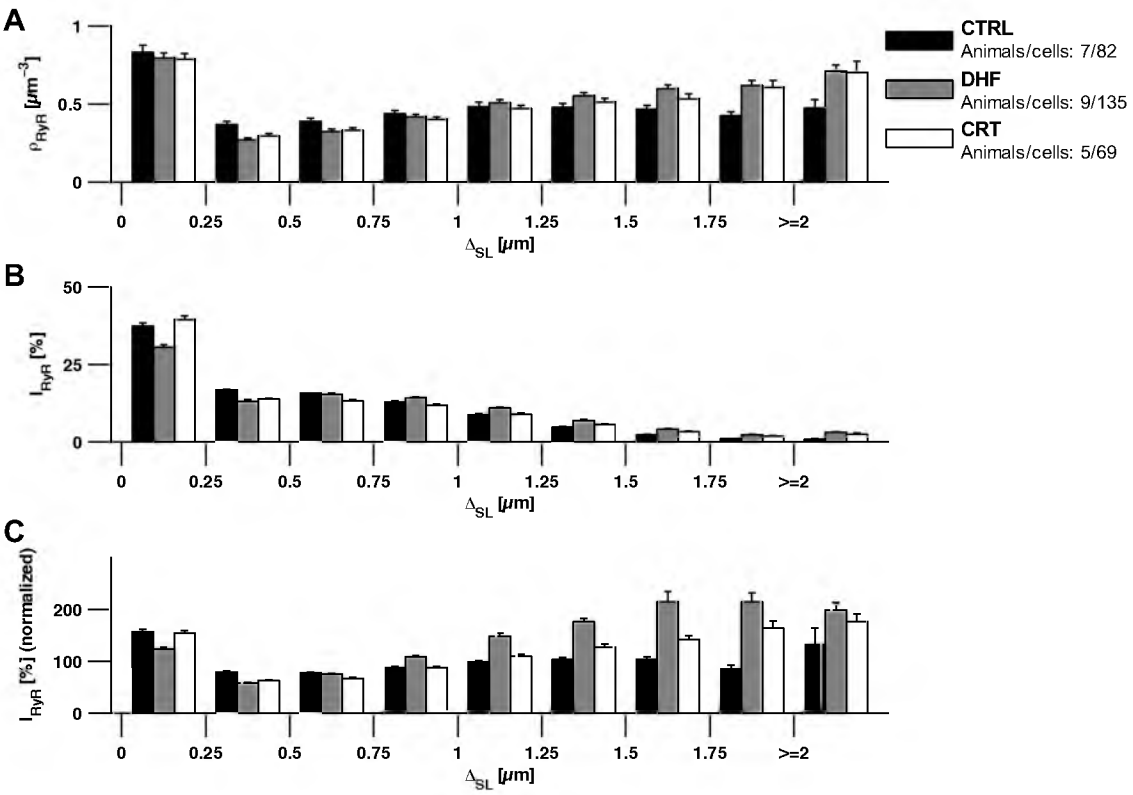

Supplemental Figure V. Distribution of (A) RyR cluster density, (B) RyR intensity, and (C) RyR intensity per volume normalized to mean value of the whole cell. Parameters were grouped with increasing distance to the sarcolemma. Means and standard errors were calculated from all analyzed cels.

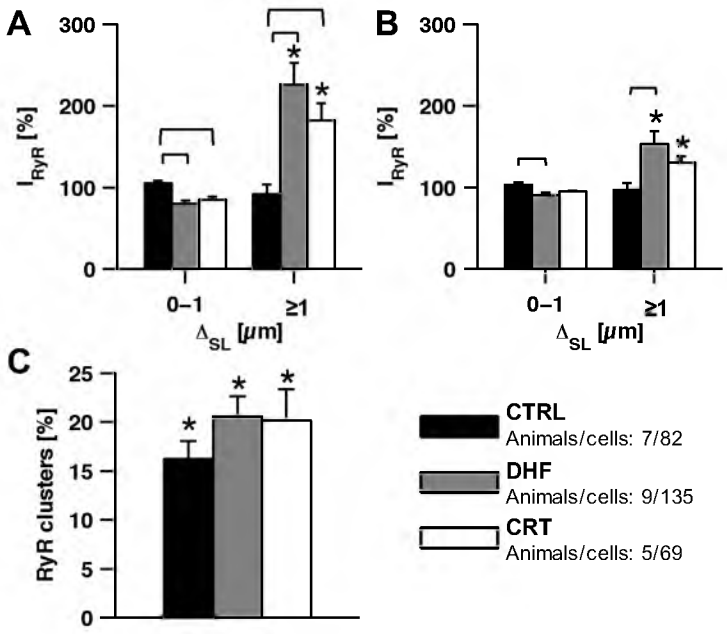

Supplemental Figure VI. Statistical analysis of intensity and occurrence of RyR clusters in lateral LV cardiomyocytes from CTRL, DHF and CRT animals. Fluorescence intensity of RyRs 0-1 and ≥1 µm from the sarcolemma, normalized to volume and mean cell intensity within (A) 0-10 µm and (B) 10-40 µm from cell end. (C) Percentage of RyR clusters detected >1 µm from the sarcolemma, which was significantly lower than within 1 µm from the sarcolemma in all animal models. The percentage did not differ between our animal models, which suggests together with the data presented in (A) and (B) that in DHF cells non-junctional RyR clusters were larger than junctional clusters. Brackets indicate statistical significance between groups, asterisks between bins of one group.

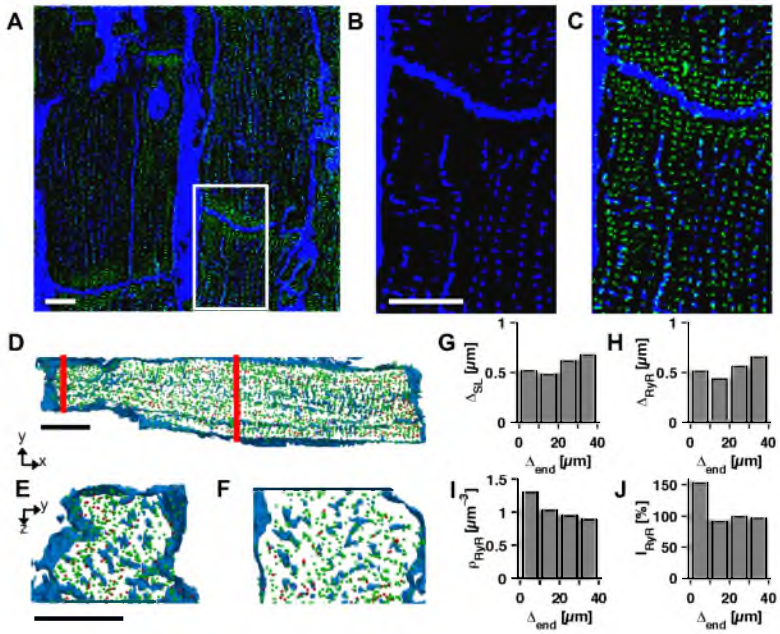

Supplemental Figure VII. Visualization and analysis of DHF cell from the anterior LV wall. (A-C) Confocal microscopic images from DHF anterior tissue showing the extracellular space (blue) and RyR clusters (green). (B) and (C) are zoom-ins from the region indicated by the white rectangle in (A). T-system is intact, but RyR intensity increases at cell ends. (D-F) 3D visualizations of 4 µm thick sections through an example cell. (D) Longitudinal section. (E) Transverse section 5 µm from cell end. (F) Transverse section 40 µm from cell end. Red bars in (D) indicate section planes. RyR clusters of high intensity (90th percentile) are shown in red, others in green. All scale bars: 10 µm. Scale bar in (B) applies to (C), scale bar in (E) applies to (F). Analysis of (G) mean intracellular voxel distance to the nearest sarcolemma, (H) mean RyR cluster distance to nearest sarcolemma, (I) RyR cluster density, and (J) RyR intensity per volume normalized to mean value of the whole cell. These parameters were analyzed within 0-40 µm from the left cell end and grouped in bins of 10 µm.

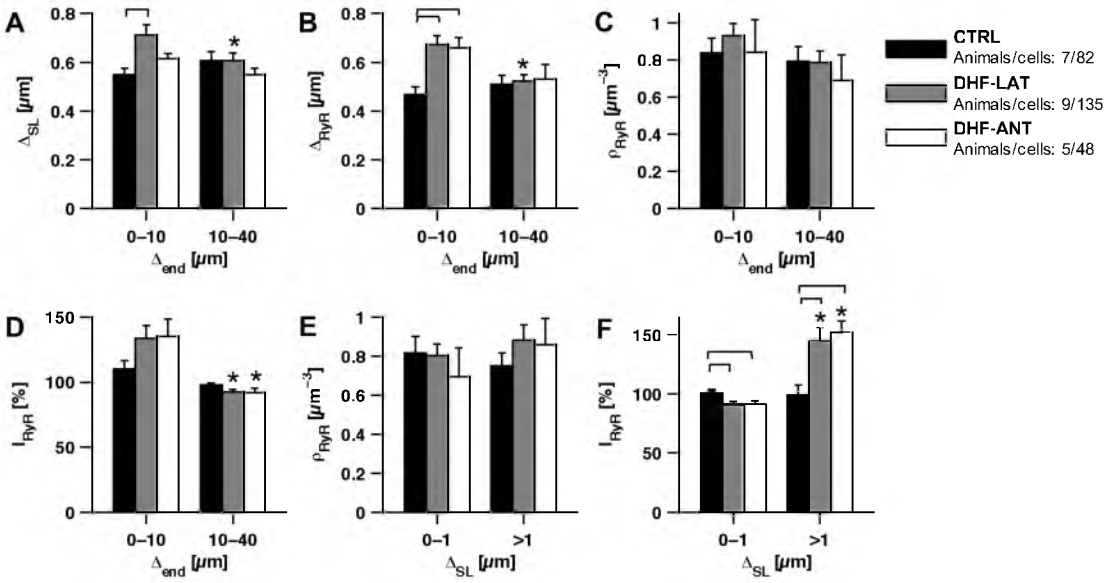

Supplemental Figure VIII. Statistical analysis of myocytes from LV lateral tissue of CTRL animals as well as LV lateral tissue (DHF-LAT) and LV anterior tissue (DHF-ANT) of DHF animals. Parameters were analyzed 0-10 µm and 10-40 µm from the cell end. (A) Intracellular voxel distance to nearest sarcolemma. (B) RyR cluster distance to nearest sarcolemma, (C) RyR cluster density, (D) RyR intensity per volume normalized to mean value of the whole cell. Parameters were analyzed 0-1 µm and ≥1 µm from the sarcolemma. (E) RyR cluster density, (F) RyR intensity per volume normalized to mean value of the whole cell. Brackets indicate statistical significance ($p<0.05$) between groups, asterisks between bins of one group.

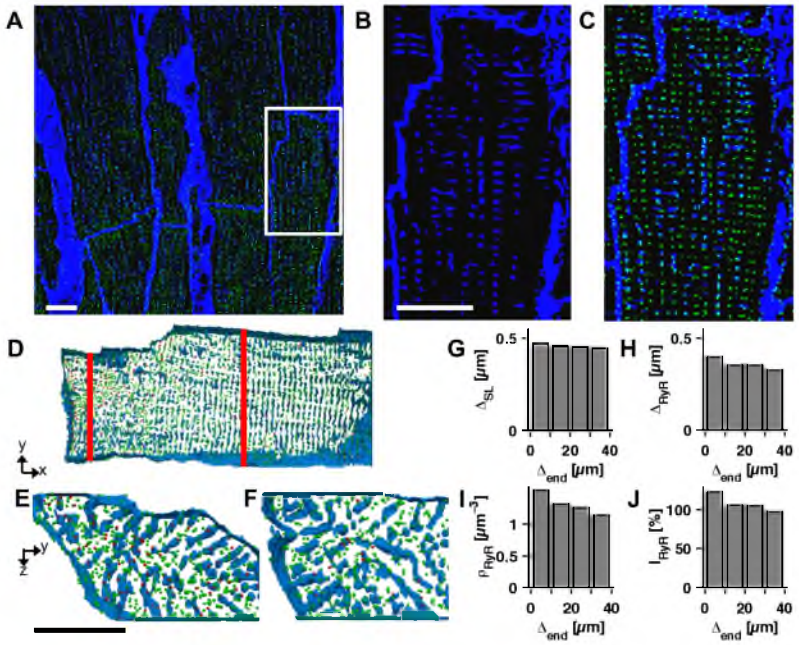

Supplemental Figure IX. Visualization and analysis of SHF cell. (A-C) Confocal microscopic images of SHF tissue showing the extracellular space (blue) and RyR clusters (green). (B) and (C) are zoom-ins from the region indicated by the white rectangle in (A). T-system is intact and RyRs are equally distributed. (D-F) 3D visualizations of 4 µm thick sections through an example cell. (D) Longitudinal section. (E) Transverse section 5 µm from cell end. (F) Transverse section 40 µm from cell end. Red bars indicate section planes. RyR clusters of high intensity (90th percentile) are shown in red, others in green. All scale bars: 10 µm. Scale bar in (B) applies to (C), scale bar in (E) applies to (F). Analysis of (G) mean intracellular voxel distance to the nearest sarcolemma, (H) mean RyR cluster distance to nearest sarcolemma, (I) RyR cluster density, and (J) RyR intensity per volume normalized to mean value of the whole cell. These parameters were analyzed within 0-40 µm from the left cell end and grouped in bins of 10 µm.

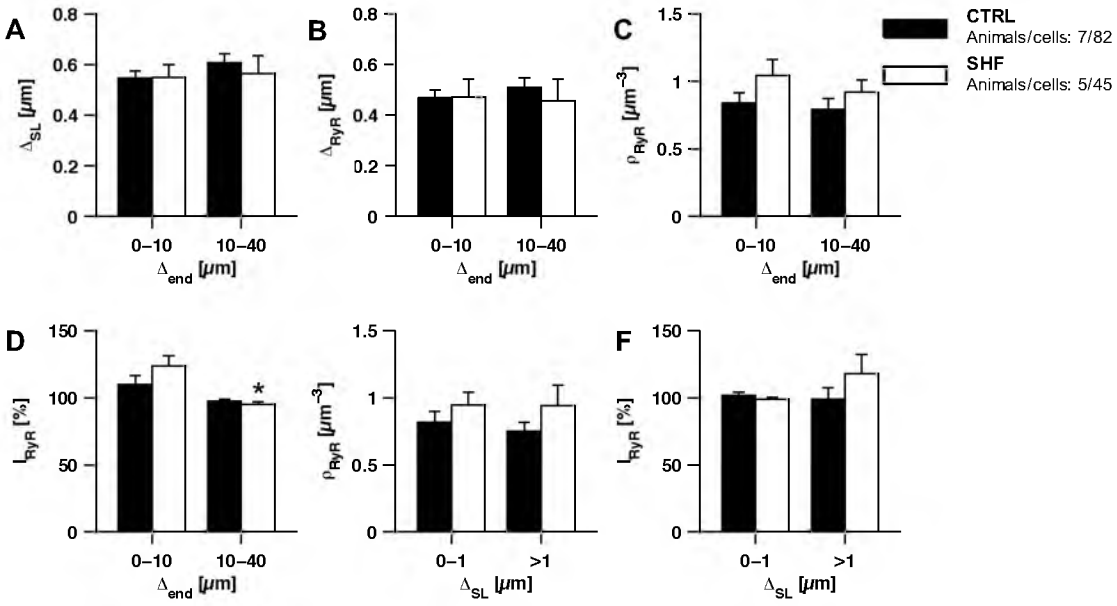

Supplemental Figure X. Statistical analysis of cardiomyocytes from CTRL and SHF animals. Parameters were analyzed 0-10 µm and 10-40 µm from the cell end. (A) Intracellular voxel distance to nearest sarcolemma. (B) RyR cluster distance to nearest sarcolemma, (C) RyR cluster density, (D) RyR intensity per volume normalized to mean value of the whole cell. Parameters were analyzed 0-1 µm and ≥1 µm from the sarcolemma. (E) RyR cluster density, (F) RyR intensity per volume normalized to mean value of the whole cell. Brackets indicate statistical significance between groups, asterisks between bins of one group.

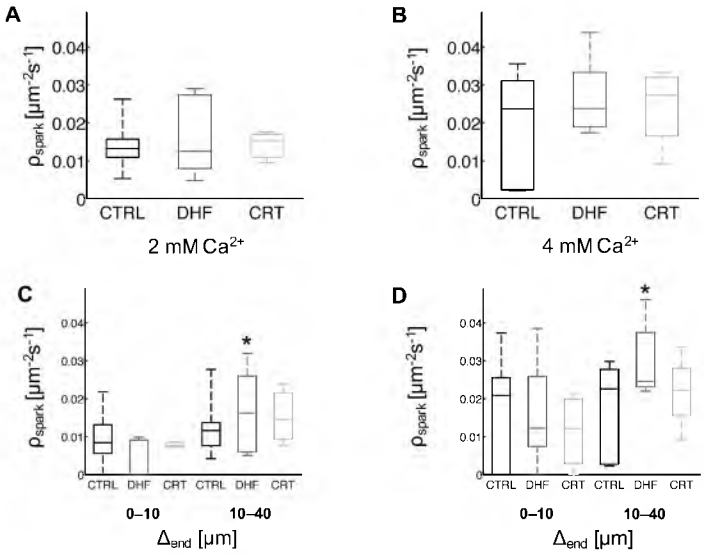

Supplemental Figure XI. Statistical analyses of diastolic spark density. Overall spark density in control (CTRL), DHF and CRT cells in a bathing solution containing (A) 2 mM and (B) 4 mM Ca^{2+} was similar. Analysis of spark density with regions less than 10 µm and between 10 and 40 µm from the cell end in a bathing solution containing (C) 2 mM and (D) 4 mM Ca^{2+} revealed subcellular heterogeneity in DHF cells. Asterisks mark statistical significance ($p<0.05$) between corresponding bins of groups. Box bars present the median, 25% percentile and 75% percentile of samples. Whiskers mark the minimum and maximum of samples.

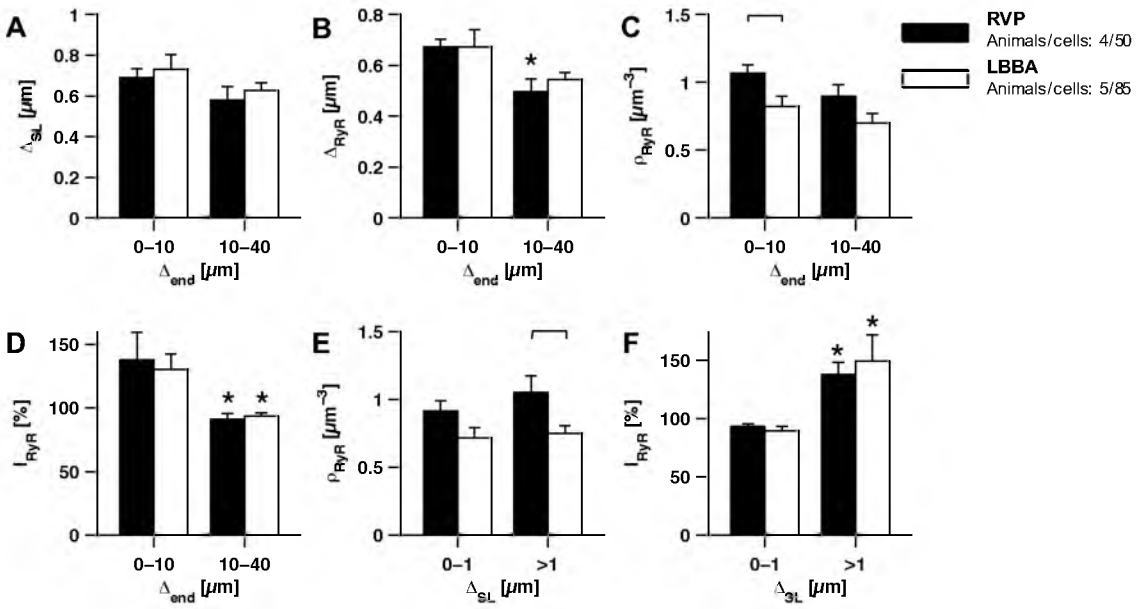

Supplemental Figure XII. Statistical analysis of cardiomyocytes from animals in DHF induced either by right-ventricular pacing (RVP) or left bundle branch ablation (LBBA). Parameters were analyzed at 0-10 µm and 10-40 µm from cell end. (A) Mean intracellular voxel distance to nearest sarcolemma. (B) RyR cluster distance to nearest sarcolemma, (C) RyR cluster density, (D) RyR intensity per volume normalized to mean value of the whole cell. Parameters were analyzed 0-1 µm and ≥1 µm from the sarcolemma. (E) RyR cluster density, (F) RyR intensity per volume normalized to mean value of the whole cell. Brackets indicate statistical significance between groups, asterisks between bins of one group.

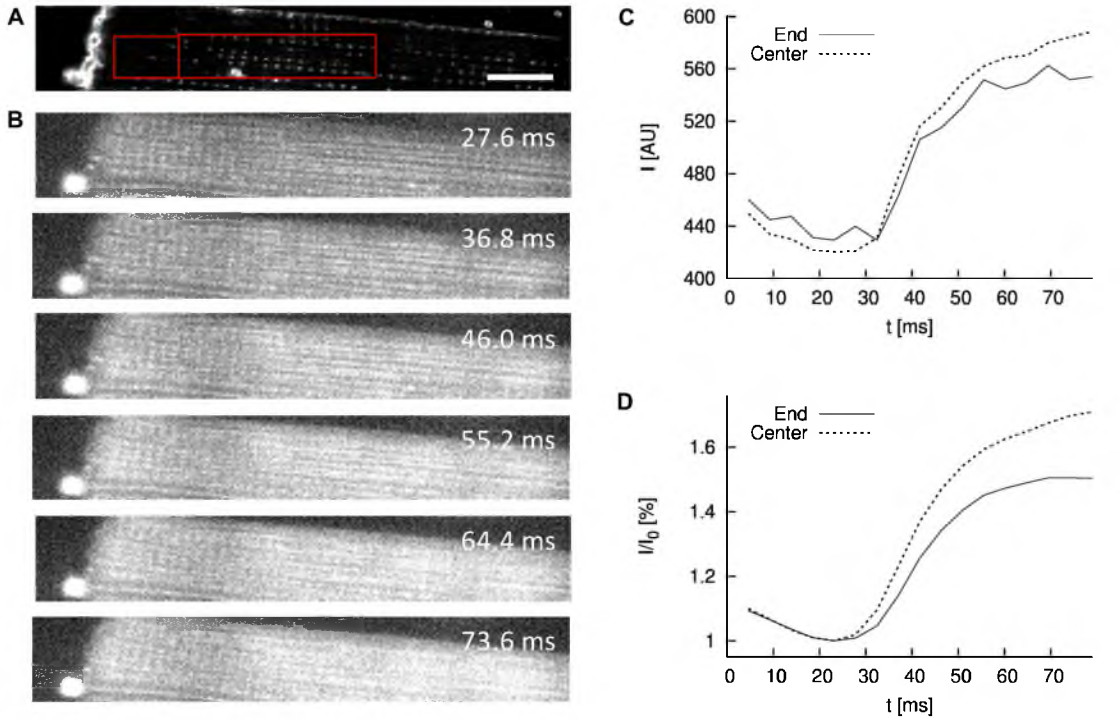

Supplemental Figure XIII. Imaging and analysis of dual-labeled isolated lateral DHF myocyte. (A) Di-8-ANEPPS labeling reveals the sarcolemma and t-system. (B) Labeling with fluo-4 produced low intensity signals in cells at rest and heterogeneously increased intensity after stimulation at 35.4 ms. (C) Fluo-4 signals at the sites marked with box in (A). The box adjacent to the cell end and in the cell center has a width of 10 and 30 µm, respectively. (D) The signals after filtering and self-ratioing with the marked region. Scale bar in (A) has a length of 10 µm and also applies to (B).

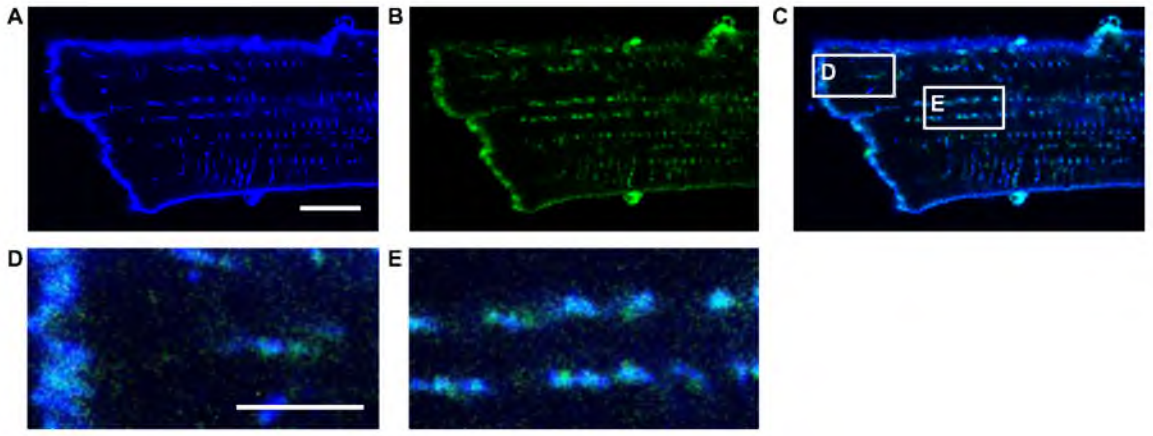

Supplemental Figure XIV. 2D confocal image of isolated lateral DHF myocyte. (A) Stained with WGA. (B) Stained for NCX. (C) Overlay. (D, E) Zoomed in region marked in (C). Scale bar in (A) has a length of 10 µm and also applies to (B) and (C). Scale bar in (D) has a length of 5 µm and also applies to (E).

Supplemental References

1. Sachse FB, Torres NS, Savio-Galimberti E, Aiba T, Kass DA, Tomaselli GF, Bridge JH. Subcellular structures and function of myocytes impaired during heart failure are restored by cardiac resynchronization therapy. *Circ Res*. 2012;110:588-597
2. Savio-Galimberti E, Frank J, Inoue M, Goldhaber JI, Cannell MB, Bridge JH, Sachse FB. Novel features of the rabbit transverse tubular system revealed by quantitative analysis of three-dimensional reconstructions from confocal images. *Biophys J*. 2008;95:2053-2062
3. Seidel T, Dräbing T, Seemann G, Sachse FB. A semi-automatic approach for segmentation of three-dimensional microscopic image stacks of cardiac tissue. *Lecture Notes in Computer Science*. 2013;7945:300-307
4. Torres NS, Sachse FB, Izu LT, Goldhaber JI, Spitzer KW, Bridge JH. A modified local control model for ca2+ transients in cardiomyocytes: Junctional flux is accompanied by release from adjacent non-junctional ryrs. *J Mol Cell Cardiol*. 2014;68:1-11
5. Baddeley D, Jayasinghe ID, Lam L, Rossberger S, Cannell MB, Soeller C. Optical single-channel resolution imaging of the ryanodine receptor distribution in rat cardiac myocytes. *Proc Natl Acad Sci U S A*. 2009;106:22275-22280
6. Franzini-Armstrong C, Protasi F. Ryanodine receptors of striated muscles: A complex channel capable of multiple interactions. *Physiol Rev*. 1997;77:699-729
7. Yin CC, Lai FA. Intrinsic lattice formation by the ryanodine receptor calcium-release channel. *Nat Cell Biol*. 2000;2:669-671
8. Crossman DJ, Ruygrok PR, Soeller C, Cannell MB. Changes in the organization of excitation-contraction coupling structures in failing human heart. *PLoS One*. 2011;6:e17901

CHAPTER 4

MEASUREMENT OF STRAIN IN CARDIAC MYOCYTES AT MICROMETER SCALE BASED ON RAPID SCANNING COFNOCAL MICROSCOPY AND NONRIGID IMAGE REGISTRATION

4.1 Abstract

Measurement of cell shortening is an important technique for assessment of the physiology and pathophysiology of cardiac myocytes. Many types of heart disease are associated with decreased myocyte shortening, which is commonly caused by structural and functional remodeling. Here, we present a new approach for local measurement of 2D strain within cells at high spatial resolution. The approach applies nonrigid image registration to quantify local displacements and Cauchy strain in images of cells undergoing contraction. We extensively evaluated the approach using synthetic cell images and image sequences from rapid scanning confocal microscopy of fluorescently labeled isolated myocytes from the left ventricle of normal and diseased canine hearts. Application of the approach yielded a comprehensive description of cellular strain, including novel measurements of transverse strain and spatial

heterogeneity of strain. Quantitative comparison with manual measurements of strain in imagesequences indicated reliability of the developed approach. We suggest that the developed approach provides researchers with a novel tool to investigate contractility of cardiac myocytes at subcellular scale. In contrast to previously introduced methods for measuring cell shorting, the developed approach provides comprehensive information on the spatio-temporal distribution of 2D strain at micrometer scale.

4.2 Introduction

Efficient pump function of the heart requires concerted contraction of cardiac muscle cells (myocytes). Contraction is commonly initiated by electrical activation of the myocytes. The term excitation-contraction (EC) coupling refers to the signaling cascade transducing electrical activation into mechanical contraction and is based on calcium signaling.[11] EC coupling in cardiac myocytes is initiated by a small influx of calcium through the membrane (sarcolemma), which triggers calcium release from an intracellular calcium store, the sarcoplasmic reticulum, into the cytosol. The calcium diffuses within the cell. Binding of calcium to the protein troponin C allows interactions of actin and myosin filaments, which generate force and induce cell shortening. The actin and myosin filaments are located in sarcomeres, which are the contractile units within cardiac myocytes.

Isolated cardiac myocytes are a major experimental preparation to study the physiological mechanisms underlying contraction. Also, isolated myocytes are a major research tool to investigate structural and functional alterations by

drugs and diseases. Several methods have been introduced to measure mechanical contraction in these cells. Early approaches for measurement of contraction were based on transmitted light microscopy and analysis of 1D or 2D image sequences. Tameyasu et al. used retrospective visual inspection of image sequences acquired at a frame rate of 200 Hz to measure segmental shortening in frog cardiac myocytes.[55] Several groups developed approaches based on 1D photodiode arrays and automated cell length detection from photodiode array data acquired at a rate of up to 1 KHz.[56,57,58] Steadman et al. introduced a video-based device that applied an edge-detector to measure myocyte shortening at a frame rate of 60 Hz.[59] Further measurement approaches employed light diffraction to measure sarcomere length.[60,61] Diffraction instruments commonly apply a laser as a light source and have a spatial resolution of several nanometers per half sarcomere. Recently developed approaches use confocal and 2-photon microscopy for measurement of cell contraction. Analyses of Fourier transformed image data determined the changes of sarcomere length.[62,63]

A typical measure of contraction is myocyte shortening λ, which is defined as

$$\lambda = \frac{l}{l_o} \qquad (1)$$

with the cell length at rest l_o and the length in the contracted state l. Commonly, shortening is presented in percentage. An alternative measure of contraction is the Cauchy (or engineering) strain *e,* defined as

$$e = \frac{l - l_o}{l_o} \quad (2)$$

Similar 1D measures have been established for quantifying shortening of sarcomeres.

While the described approaches yielded valuable insights into myocyte contraction, they only provide 1D information on contraction of cells or sarcomeres and do not yield information on transverse strain in response to contraction. Furthermore, the approaches lack high spatial resolution, which makes it difficult to characterize subcellular heterogeneities.

Here we introduce a new approach for local measurement of 2D strain within cells at a high spatial resolution. We developed the approach based on studies of synthetic cells and paced isolated myocytes from the left ventricle of canine hearts. We used cells from control animals and animals with dyssynchronous heart failure (DHF), which is thought to lead to severe remodeling of structures and functions associated with EC coupling and contraction.[42,43,46,64,65] Our approach is based on fluorescent labeling of the sarcolemma. Many types of myocytes exhibit a specialization of the sarcolemma, the transverse tubular system (t-system), which serves as the major initiation site for excitation-contraction coupling. Our approach takes advantage of the spatial distribution of sarcolemma including t-system within myocytes, which is imaged using rapid-scanning confocal microscopy at high spatiotemporal resolution. We applied a previously developed method for nonrigid image registration to obtain a transformation describing the deformation between sequential frames of contracting myocytes.[66] We used this transformation to quantify the local

displacement and strain within the myocyte during contraction. Finally, we evaluated the approach by comparison with manual measurements of strain.

4.3 Materials and Methods

4.3.1 Animal Model and Cell Preparation

Animal studies complied with the *Guide for the Use and Care of Laboratory Animals* published by the National Institute of Health. All procedures were approved by the Animal Care and Use Committees of the University of Utah.

The animal model and methods for cell isolation have been previously described.[43,46,54,64,67] Briefly, mongrel canines were used as control and DHF models. DHF animals underwent pacemaker implantation with the pacing lead introduced through the jugular vein and anchored in the right ventricular apex. DHF was achieved by tachypacing in the right ventricle at 180-200 BPM for 6 weeks. Success of the model was determined by weekly ECGs and acquisition of hemodynamic data at the time of device implantation and harvesting of cells. We provide a description of our protocol for cell isolation in the supplemental data.

4.3.2 Confocal Imaging and Image Processing

Isolated cells were incubated with 12.5 μM of the Ca^{2+} sensitive dye Fluo-4 AM (Invitrogen, Grand Island, NY, USA) for 20 min. Cells were then exposed to 6.25 μM of the membrane staining dye Di-8-Anepps (Invitrogen) for 8 min. The cells were allowed to settle on the glass slide of a perfusion chamber attached to

a Zeiss LSM 5 Live Duo confocal microscope equipped with a 63× oil immersion objective. The bath chamber was held at 37°C and perfused with the modified Tyrode's solution containing 2 or 4 mM Ca^{2+}. In some cases 1 μM isoproterenol (Iso), a nonselective beta-adrenergic agonist, was added to the 4 mM Ca^{2+} solution to simulate beta-adrenergic stimulation. A 489-nm-wavelength-emitting diode laser was used to excite both dyes simultaneously. Emitted light was filtered using a dichromatic mirror with a cutoff wavelength of 535 nm and bandpass filters of 505 to 610 nm and 560 to 675 nm to split the Fluo-4 and Di-8-Anepps signals, respectively. Cells were field stimulated using a current amplitude of 10 mA. The cells were conditioned with a train of at least 10 stimuli at 0.5 Hz. Image acquisition was triggered 20-40 ms prior to the final stimulus. Sequences of 100 2D images with a size of 128×1024 pixels were acquired at a frame rate of 4.6 ms/frame. Pixel sizes were 0.1×0.1 μm. Imaging was restricted to cells exhibiting clear striations and a regular brick shape. Example images acquired from a control cell are shown in Fig. 4.1A. Images from a control cell in the presence of isoproterenol and a DHF cell are presented in Fig. S4.1 A and C, respectively.

Low-frequency noise in Fluo-4 and Di-8-Anepps images was filtered using Fourier transform. Crosstalk in the two images was calculated and removed in the Di-8-Anepps signal as previously described.[68] Noise reduction and background removal of the Di-8-Anepps signal was performed by filtering with a discretized 2D mean free Gaussian filter (13×13 pixels, $\sigma_x=\sigma_y=0.2$ μm). A mask of the cell interior was created using predefined seed points and the watershed-

based method previously described.[69] The cell mask defined a region of interest for subsequent analyses, allowing for the removal of extracellular debris and segments from other cells. Results of this preprocessing on the control cell, control cell in the presence of isoproterenol, and DHF cell are presented in Fig. 4.1B, C, and D, respectively. Additional examples for this processing are provided in Fig. S4.1. The cell mask, a manually defined angle of orientation, and a semiautomatically selected endpoint were used to create a Euclidean distance map from the cell end. We used the combination of the cell mask and distance map to create regions of interest for the registration algorithm.

4.3.3 Manual Strain Measurement

Manual strain measurement of cells was performed in raw image sequences using ImageJ (v1.48).[70] In an image of a cell at rest, a line with a width of 8 pixels was drawn parallel to the longitudinal axis of the cell, while intersecting the cell end and several t-tubules (Fig. 4.2A). A second line was drawn intersecting the same structural landmarks of the cell in the image at peak contraction (Fig. 4.2C). The profiles of these two lines were examined (Fig. 4.2B and D) and local intensity maxima corresponding to the cell end and t-tubules identified. The maxima locations were used to calculate distances at rest and peak contraction. These distances were then used to calculate the Cauchy strain (Eqn. 2).

4.3.4 Synthetic Cells

We generated synthetic cells with a resting length and width of 100 and 15 μm, respectively. Cells were assumed to be iso-volumetric during contraction and exhibiting transversely isotropic mechanical properties. Thus, for a given longitudinal strain ε_{Long}, the transverse strain ε_{Trans} was calculated as

$$\varepsilon_{Trans} = \sqrt{\frac{1}{(1+\varepsilon_{Long})}} - 1 \quad (3)$$

Cells were modeled to have a ε_{Long} of -10% at maximal contraction, which results in a length and width of 90 and 15.8 μm, respectively. The final ε_{Long} of -10% was achieved in 10 linear steps, each at 1% contraction of the original image. We assumed a homogeneous distribution of t-tubules at a spacing of 2 and 1 μm in the longitudinal and transverse direction, respectively. This resulted in 49 columns and 14 rows of t-tubules. Spacing of the t-tubules was adjusted according to the strain described above.

We rendered the synthetic cells in 2D images at an isotropic spatial resolution of 160 pixels/μm. Images were convolved with a 2D Gaussian filter (208×208 pixels, σ_x=σ_y=0.5 μm). Subsequently, the images were down-sampled to a resolution of 10 pixels/μm.

Overall, five synthetic cells were created. Two complete cells were rendered, one at 0° and one at 10° rotation. Three cropped cells were rendered in an image with a size of 128×1024 pixels. One of these cropped cells had 0° rotation, while the other two had a 5° rotation. One of the cropped cells with 5°

rotation was rendered as a detubulated cell. The detubulated cell had all t-tubules within 10 μm of the cell end removed.

4.3.5 Automated Strain Measurement

4.3.5.1 Nonrigid Image Registration

Our approach for strain measurement in image sequences from contraction cells is based on establishing a transformation **T**, which registers a reference image $\mathbf{I_{ref}}$ to a deformed image $\mathbf{I_{def}}$. To register consecutive images in the image sequences we applied a previously developed efficient method for nonrigid image registration based on B-splines.[66] Here, the transformation for a control point mesh was obtained by minimizing the cost of image registration $C_{Registration}$ comprising four cost terms:

$$C_{Registration} = C_{SSD} + \psi_{Be} C_{Be} + \psi_{Le1} C_{Le_1} + \psi_{Le2} C_{Le_2} \quad (4)$$

with cost related to image similarity C_{SSD}, bending C_{Be}, and linear elasticity C_{Le_1} and C_{Le_2}, as well as the weighting factors for their respective cost terms ψ_{Be}, ψ_{Le1}, and ψ_{Le2}. Full detail on the nonrigid image registration method and cost terms is provided in the supplemental material.

4.3.5.2 Strain Calculation

From the control point grid transformation, we calculated the displacement field **u**:

$$\mathbf{u} = \boldsymbol{\theta}' - \boldsymbol{\theta} \quad (5)$$

where $\boldsymbol{\theta}$ and $\boldsymbol{\theta}'$ are the original and deformed control point positions, respectively. Spacing of the control point grid in all presented studies was 1 µm in x- and y-direction.

From the displacement field we calculated Cauchy's strain tensor $\boldsymbol{\varepsilon}$ at each control point:

$$\boldsymbol{\varepsilon} = \frac{1}{2}((\nabla \mathbf{u})^T + \nabla \mathbf{u}) = \begin{pmatrix} \frac{\partial u_x}{\partial x} & \frac{1}{2}\left(\frac{\partial u_x}{\partial y} + \frac{\partial u_y}{\partial x}\right) \\ \frac{1}{2}\left(\frac{\partial u_x}{\partial y} + \frac{\partial u_y}{\partial x}\right) & \frac{\partial u_y}{\partial y} \end{pmatrix} \quad (6)$$

with the gradient operator $\boldsymbol{\nabla}$. This strain tensor was then rotated into the coordinate system of the myocyte, which allowed us to determine the longitudinal strain $\boldsymbol{\varepsilon_{Long}} = \boldsymbol{\varepsilon_{11}}$ and the transverse strain $\boldsymbol{\varepsilon_{Trans}} = \boldsymbol{\varepsilon_{22}}$.

For parameter sensitivity studies and stochastic parameter optimization we assessed total cost of a transformation obtained by nonlinear image registration by a cost $\boldsymbol{C_{IMG}}$ related to image similarity:

$$C_{IMG} = \frac{1}{N}\sum_{n=1}^{N}(\mathbf{I_{ref}}(n) - \mathbf{I_{def}}(n))^2 \quad (7)$$

and a second cost term C_σ determined by the standard deviation σ of the longitudinal strain ε_{Long} and the transverse strain ε_{Trans}:

$$C_\sigma = \sigma(\varepsilon_{Long})^2 + \sigma(\varepsilon_{Trans})^2 \quad (8)$$

For these cost calculations only image values and strains within a region of interest were considered. These two terms determine the total cost $\boldsymbol{C_{Total}}$:

$$C_{Total} = \sqrt{C_{IMG} + \gamma C_\sigma} \quad (9)$$

with the weighting factor γ.

The algorithm calculated incremental strain ε^f at each control point, which is defined as the strain (longitudinal or transverse) between image f and $f+1$. To obtain the total strain ε_T^f at image f, from initial image $f=1$, we integrated mean incremental strains ε^f using

$$\varepsilon_T^f = \left(\sum_{i=2}^{f} \varepsilon^{i-1}(1+\varepsilon^i) \right) - 1 \qquad (10)$$

4.3.5.3 Parameter Sensitivity

In order to investigate how weights of registration costs affect the image registration results and strain calculations, we designed a parameter sensitivity study. We varied the input parameters, in particular, weights for the bending energy and two linear elasticity terms. Weights of bending cost explored were 10^{-1}, 10^{-2}, ..., 10^{-8}. Weights of both linear elasticity costs explored were 10^{0}, $10^{-0.25}$,$10^{-0.5}$, ..., 10^{-4}. Overall, each parameter sensitivity study led to a total of 2,312 image registrations.

4.3.5.4 Parameterization Based on Stochastic Optimization

We applied an approach for stochastic parameter optimization to minimize total cost of image transformation and the associated strain (Eqn. 9). In previous work, we developed this approach for parameterization of models of ion channels.[71] The approach iteratively evaluates variants of input parameters ψ_{Be}, ψ_{Le1}, and ψ_{Le2} for registration of image pairs. Initial values for optimization were determined by the parameter sensitivity study described above on sample frames

from image sequences. The algorithm then generated 80 parameter sets with random perturbations ($10\% - 1000\%$) from the initial parameter values constrained by the ranges [10^{-8} 10^{-1}] for the weights of bending cost and [10^{-4} 10^{0}] for weights of the linear elasticity costs. The cost C_{Total} for each parameter set was calculated. Two parameter sets yielding the smallest C_{Total} were used as initial values for the next iteration. Five iterations were performed, resulting in 400 calculations for each image pair. The parameter set with minimal C_{Total} after the fifth iteration was kept, and the resulting transformation was used for subsequent analyses.

4.3.5.5 Implementation

Image processing and the strain measurement algorithm were implemented in MATLAB 2014a (Mathworks, Natick, NA). We used a C++ implementation of a method for nonrigid image registration (NiftyReg, v1.39).[72] We provide further detail on the implementation in the Supplemental Material.

4.4 Results

4.4.1 Evaluation of Algorithm

4.4.1.1 Parameter Sensitivity Study on Synthetic Cells

We performed an extensive parameter sensitivity study to investigate properties of nonrigid image registration for strain measurement in cardiomyocytes. We used synthetic cells with a homogeneous strain distribution for this purpose. The sensitivity study revealed that in these cells, minimal C_{IMG},

i.e. maximal similarity of the reference and deformed image, is not associated with minimal $\sigma(\varepsilon_{Long})$ and $\sigma(\varepsilon_{Trans})$ (Fig. 4.3A and B), indicating heterogeneity of strain distributions after image registration. Because strain was homogeneous in the synthetic cells, the measured heterogeneity suggests a general issue in the application of the described nonlinear image registration approach for strain measurement. We thus developed a simple cost function (total cost C_{Total}, Eqn. 9) to include measures of strain heterogeneity. Investigating this cost function (Fig. 4.3C) revealed that various parameter sets yield small C_{Total} while maintaining a small C_{IMG}.

We present cost terms C_{IMG}, C_{σ}, and C_{Total} resulting from image registration of a synthetic cell in Fig. 4.4. Cost distributions were a complex function of weighting parameters. Cost distributions exhibited local maxima and minima, thus hindering traditional optimization approaches for parameter identification. However, various parameter combinations yielded small C_{Total}.

4.4.1.2 Strain Measurement in Synthetic Cells

We studied reliability of strain detection in various synthetic cells. Minimizing the cost function described in Eqn. 9, we studied strain measurement in the complete, unrotated synthetic cell (Fig. 4.5). A calculated displacement field for -10% strain is shown in Fig. 4.5B. Resulting displacements in long-axis (x) direction were 5 and -5 μm at the left and right cell end, respectively. The displacement amplitude decays linearly to 0 μm at the center of the cell. Trans-axis (y) displacements also increased linearly from -0.5 pixels to 0.5 μm from the

top to bottom of the cell. The measured displacements consistent with the displacements specified for a homogeneous ε_{Long} *and* ε_{Trans} of -10% and +5% of the synthetic cell. Cauchy's strain tensor $\boldsymbol{\varepsilon}$ was then calculated using this displacement field (Eqn. 6). A discretized map of the resulting strain tensors is shown in Fig. 4.5C. Strain tensors were approximately uniform within the cell, but strain outside of the cell varied significantly. However, our analyses were restricted to the cell interior.

Fig. 4.5D shows the incremental strains calculated for images with decreasing ε_{Long} to -10% and increasing ε_{Trans} to 5% in 10 steps. Solid lines present results of stochastic optimization (described above). The black plus signs and squares present strain calculations with constant input parameters, which were optimized for the first and second images. In this cell differences between the static registration and the stochastic optimization approach were small. Each image in the sequence describes cell deformation for a specific strain versus the original image, thus ε_{Long} is not constant at 1%. The minor negative slope is in agreement with the specified ε_{Long}.

We assessed homogeneity of ε_{Long} and ε_{Trans} within the cell (Fig. 4.5E). Standard deviation of strain from registration of images 1 and 2 is smallest since optimal parameter values were derived from the parameter sensitivity study using these images. Overall the standard deviation is smaller than 0.1% for both strains. We calculated the total strain (Eqn. 10, Fig. 4.5F). ε_{Long} decreased linearly from -1% to -10% in images 1 to 10, while ε_{Trans} increased from 0.5% to 5.5%, which is consistent with the strain specified for the synthetic cell.

4.4.1.3 Strain Measurements in Rotated and Partial Synthetic Cells

We next assessed reliability of the strain measurement algorithm under realistic conditions for cell imaging. We considered that imaged cells exhibit various angles and are only partially in the field of view (Fig. 4.6). We investigated models of a complete and rotated (Fig. 4.6A), cropped and unrotated (Fig. 4.6D), cropped and rotated (Fig. 4.6G), and cropped, rotated and partially detubulated cell (Fig. 4.6J). Incremental strains using the stochastic parameter optimization approach and static parameters for each of these configurations are shown in Fig. 4.6B, E, H, and K. Total strains are presented in Fig. 4.6C, F, I, and L. While the stochastic optimization approach yielded expected results for all cell configurations, using static parameters led to several cases of inaccurate measurements. This is most apparent in Fig. 4.6E and K. Overall these studies indicate that strain measurement based on stochastic parameter optimization is superior versus measurement applying static parameters.

A summary of strain measurements for all synthetic cells is presented in Table 4.1. This data shows that errors between specified and measured strains are small. Even using images of cells that were cropped, rotated and de-tubulated, errors for ε_{Long} and ε_{Trans} were up to 0.1%, and 0.3%, respectively. Importantly, the summary suggests that the developed stochastic parameter optimization approach was able to capture the strain in a reliable manner. Furthermore, the studies indicate that reliability of strain detection is not affected by limited field of view and density of t-system.

4.4.2 Strain Measurements in Ventricular Cardiomyocytes

We investigated the approach of stochastic parameter optimization introduced above in image sequences from rapid scanning of contracting ventricular myocytes (Fig. 4.1 and Fig. S4.1). In particular, we explored whether the approach is capable of detecting heterogeneity of regional contraction. For this purpose, we binned cells into 10 µm regions from the longitudinal cell end and evaluated cost terms within these regions. We measured regional incremental (Fig. 4.7A, D, and G) and total strains (Fig. 4.7B, E, and H) for a control cell in 4 mM Ca^{2+}, a control cell in 4 mM Ca^{2+} with isoproterenol, and a DHF cell in 2 mM Ca^{2+}. We then analyzed the regional transients of ε_{Long} and ε_{Trans}. In Table 4.2 we summarized quantitative data from these analyses.

The maximal incremental ε_{Long} and its timing varied between all three cells. Time of maximal incremental ε_{Long} was 32.2, 23.0, and 55.2 ms for the control, control/Iso and DHF cell, respectively. Here, times are related to first appearance of calcium signal, which occurs shortly after pacing. Peak ε_{Long} and time to peak ε_{Long} varied among the 3 cells: -13.7% at 170.2 ms for control, -25.7% at 253 ms for control cell/Iso, and -11.0% at 271.4 ms for the DHF cell. Both control cells did not display major differences between the 4 regions over the course of contraction. However, the DHF cell exhibited a ~40% reduction in peak ε_{Long} within 0-10 µm when compared to the other regions, which exhibited only minor differences of peak ε_{Long}.

Comparison of measured ε_{Long} and ε_{Trans} revealed an inverse relationship. In all cells, decreased ε_{Long} was associated with increased ε_{Trans}. Similar as for ε_{Long}, the DHF cell exhibited a large heterogeneity of ε_{Trans}, with small values found at the cell end. In all cells, predicted ε_{Trans} (Eqn. 3) was not in agreement with measured ε_{Trans}.

To evaluate reliability of the developed approach we compared calculated results with results from manual strain measurement. Results from manual strain measurements are plotted in Fig. 4.7C, F, and I. Control cells exhibited homogeneous ε_{Long} within all regions, while the DHF cell showed decreased ε_{Long} within 0-10 μm of the cell end. For all cells and regions, the difference between calculated and measured ε_{Long} was small (Table 4.2).

4.5 Discussion

In this study, we introduced and evaluated an approach for measurement of regional strain in image sequences of contracting cardiac myocytes acquired with rapid scanning confocal microscopy. The approach is based on nonrigid image registration and calculation of strain from registered images. In contrast to previously developed approaches, the approach is capable of measuring longitudinal and transverse strain at microscopic scale in 2D.

We applied synthetic cells to develop and extensively evaluate the approach. We further explored the approach in a control cardiomyocyte, a cell with drug-increased contractility, and a cell from an animal model of heart failure. The presented analyses of measured strain profiles indicate that the approach

facilitates quantitative characterization of contractility of cardiac myocytes. In particular, application of the approach allowed us to comprehensively quantify cell contractility and regional heterogeneity of cell contraction in heart failure cells. Contraction in control cells with or without adrenergic stimulation was regionally homogenous. Adrenergic stimulation was associated with accelerated and largely increased shorting (more negative ε_{Long}) versus control. DHF was associated with delayed and decreased shortening (less negative ε_{Long}), which is consistent with previous measurements,[73] as well as regional heterogeneity of contraction, which has not been reported before.

While it is well established that various types of heart failure are associated with microstructural heterogeneity of cardiomyocytes,[64,65] effects of this heterogeneity on regional contraction have not been studied. In our previous work, we found regional structural remodeling, in particular, detubulation at cell ends in DHF,[65] which might explain the finding of reduced shortening detected by the developed approach. Some degree of detubulation at the cell end is also visible in the studied DHF cardiomyocyte (Fig. S4.1C). The presented development was motivated by our interest in the effects of this heterogeneity on contraction. We suggest that the developed approach provides researchers with a crucial tool to investigate regional heterogeneity of contraction. Additionally, the approach provides additional information on strain versus previously employed methods. We anticipate that improved description of the mechanical properties of contracting myocytes using these measurements will lead to further development and evaluation of computational models of myocyte contraction.[74]

In initial studies with synthetic cells we found that various choices of parameters for image registration were associated with high similarity of registered images, but strains measured from these registrations varied widely within the cell (Fig. 4.3). Thus it is not possible to use them without modification for reliable measurement of regional cellular strain. We added a cost term to restrict the regional strain variability, while maintaining high similarity of registered images (Eqn. 9). The results of the parameter sensitivity study show that even this cost term yields many maxima and minima. This hinders the ability of traditional methods for minimization to converge and find a global minimum. Thus we implemented a stochastic optimization approach using a total cost term for parameterization of image registration, which was crucial to avoid issues resulting from static parameterization of the image registration (e.g. Fig. 4.6E and G). We investigated several variants of synthetic cells, including cells that were cropped and rotated within the image similar as seen in our imaging sequences from rapid scanning confocal microscopy (Fig. 4.1 and Fig. S4.1). Strain measurements from those cells and a synthetic cell with sparse t-system suggested that the developed stochastic optimization approach is robust with respect to imaging conditions and microstructural variation of cells.

Our approach provides information on transverse strain in addition to the conventionally measured longitudinal strain. None of the methods developed over the last 3 decades described in the Introduction were capable of or attempted to extract this information. The measured strain yielded an inverse relationship between ε_{Long} and ε_{Trans}, which reflects the volume preservation that

is commonly assumed during myocyte contraction. However, the prediction of ε_{Trans} based on ε_{Long}, assuming volume preservation and transversely isotropic mechanical properties (Eqn. 3), yielded larger values than our measurement of ε_{Trans}. This might be explained by transversely anisotropic dilation of contracting cells. Commonly, isolated cells are lying flat on the glass slide, i.e. cell height is smaller than width. The imaging section is parallel to the first and second principal axes of myocytes. To account for volume preservation and our resulting measurements, ε_{Trans} would be required to be larger along the third than the second principal axis. Anisotropy in the transverse strain could be caused by anisotropic mechanical properties of cells resulting from cellular microstructure, for instance, by anisotropic arrangement of the cytoskeleton.

We evaluated our approach for strain measurement using manual detection in image sequences during contraction of cardiac myocytes. Manual strain detection was based on analyses of images from cells at rest and peak contraction. While manually measured and calculated strains were in agreement for all investigated cells, we note several major difficulties with the approach for manual measurements. First of all, small differences of peak image intensity detection strongly affect strain calculations. In particular at the cell end, local intensity profiles might exhibit peaks that do not correspond to a single location, but are produced by overlay of several structures that are displaced during contraction. A further issue is related to structures that move into and out of the field of view. Here, correspondence of profiles at rest and in contraction cannot be established.

4.5.1 Limitations

We discussed limitations of our methods for cell labeling and rapid scanning confocal microscopy previously.[65,75] In short, confocal microscopy has a limited spatial and temporal resolution. Imaged structures, i.e. Di-8-anepps labeled sarcolemma, are thin (~5 nm), thus images of those structures are strongly affected by the point-spread function of the imaging system.[76] We did not explore methods of image deconvolution to reduce this artefact. We do not believe that limited temporal resolution affected the presented strain measurements, because inspection of the strain profiles caused by contraction did not indicate frequency components beyond what can be covered by a sampling of 4.6 ms/frame based on the sampling theorem. Also, images from confocal microscopy are affected by several sources of noise. To reduce the effects of noise on strain detection, we applied filters for noise reduction. A limitation of our approach is its dependence on t-system distribution as structural markers within the cell. Alternative labeling approaches in living cells are currently in development and include fluorescent markers of intracellular organelles, in particular, mitochondria and sarcomeric proteins.[77] A limitation of our study is that we investigated only contraction and neglected relaxation. While this was motivated by our focus on characterizing the contractility of diseased cells, we do not expect issues with applying the approach for measurements of cell relaxation. While our image data also includes information on calcium signaling, we did not attempt to establish a relationship between calcium and contraction.

4.5.2 Acknowledgements

This study was supported by NIH grant R01 HL094464 (FBS) and the Nora Eccles Harrison Treadwell Foundation (FBS). We thank Mrs. Jayne Davis and Mrs. Nancy Allen for technical support as well as Dr. Thomas Seidel for discussions and help with the segmentation of cardiomyocytes. We acknowledge Dr. Marc Modat for providing us with information on the implementation of NiftyReg.

Table 4.1. Quantitative results of strain measurement in synthetic cells. Corresponding cells are shown in Figs. 4.4A, 4.5A, 4.5D, 4.5G, and 4.5J. *Set* ε_{Long} is the strain specified for the synthetic cells. *Measured* ε_{Long} is peak longitudinal strain measured using stochastic parameter optimization. $\Delta\varepsilon_{Long}$ is the difference between the mean of *Set* ε_{Long} and *Measured* ε_{Long}. *Set* ε_{Trans} is the specified transverse strain calculated using Eqn. 3. *Measured* ε_{Trans} is the peak measured transverse strain using stochastic parameter optimization. $\Delta\varepsilon_{Trans}$ is the difference between *Set* ε_{Trans} and *Measured* ε_{Trans}.

Cell	*Set* ε_{Long} [%]	*Measured* ε_{Long} [%]	$\Delta\varepsilon_{Long}$ [%]	*Set* ε_{Trans} [%]	*Measured* ε_{Trans} [%]	$\Delta\varepsilon_{Trans}$ [%]
Complete	-10.0	-9.9	0.1	5.4	5.4	0.0
Complete and rotated	-10.0	-10.1	0.1	5.4	5.4	0.0
Cropped	-10.0	-10.0	0.0	5.4	5.5	0.1
Cropped and rotated	-10.0	-10.0	0.0	5.4	5.6	0.2
Cropped, rotated and de-tubulated	-10.0	-10.1	0.1	5.4	5.7	0.3

Table 4.2. Quantitative results of strain algorithm on ventricular cardiomyocytes. Control, Control/Iso and DHF cells are shown in Fig. 4.1B, 4.1C, and 4.1D respectively. *Manual* ε_{Long} is the average of the manual strain calculation for each region, reported as mean ± standard deviation with the number of points, n, measured for the region. *Measured* ε_{Long} is the peak longitudinal strain measured using stochastic parameter optimization. $\Delta\varepsilon_{Long}$ is the difference between the mean of *Manual* ε_{Long} and *Measured* ε_{Long}. *Predicted* ε_{Trans} is the transverse strain calculated by Eqn. 3 using *Measured* ε_{Long}. *Measured* ε_{Trans} is the peak measured transverse strain using stochastic parameter optimization. $\Delta\varepsilon_{Trans}$ is the difference between *Predicted* ε_{Trans} and *Measured* ε_{Trans}.

Cell	Range [μm]	*Manual* ε_{Long} [%]	*Measured* ε_{Long} [%]	$\Delta\varepsilon_{Long}$ [%]	*Predicted* ε_{Trans} [%]	*Measured* ε_{Trans} [%]	$\Delta\varepsilon_{Trans}$ [%]
Control	0-10	-13.8 ± 1.2 (n=5)	-13.5	0.3	7.5	6.9	0.6
	10-20	-13.2 ± 1.1 (n=5)	-14.0	0.8	7.8	6.6	1.2
	20-30	-14.0 ± 0.8 (n=2)	-13.7	0.3	7.6	5.1	2.5
	30-40	-13.5 (n=1)	-13.0	0.5	7.2	5.8	1.4
Control /Iso	0-10	-23.1 (n=1)	-24.4	1.3	15.0	7.5	7.5
	10-20	-26.5 (n=1)	-25.7	0.8	16.0	8.3	7.7
	20-30	---	-23.7	---	14.5	7.8	6.7
	30-40	-25.0 (n=1)	-23.1	1.9	14.1	9.0	5.1
DHF	0-10	-6.3 ± 0.8 (n=5)	-6.5	0.2	3.4	-0.3	3.7
	10-20	-12.0 ± 1.8 (n=5)	-11.0	1.0	6.0	2.9	3.1
	20-30	-10.5 ± 0.6 (n=2)	-10.6	0.1	5.8	1.7	4.1
	30-40	---	-10.0	---	5.4	3.8	1.6

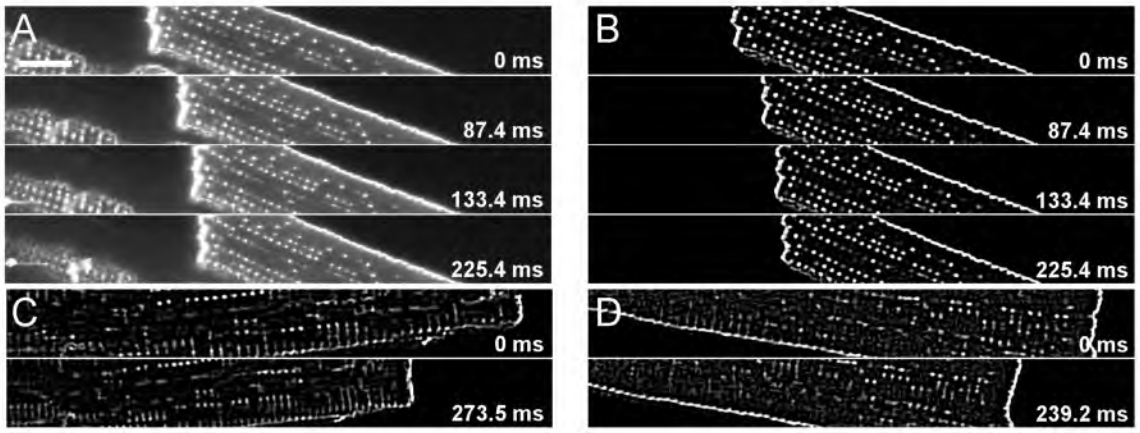

Fig. 4.1. Raw and preprocessed Di-8-Anepps images from ventricular cardiomyocytes. (A) Raw and (B) preprocessed Di-8-Anepps images from control cell at different times during contraction. Preprocessed images of (C) control cell/Iso and (D) DHF cell at 0 ms and at peak contraction. Scale bar in (A) applies to (B), (C) and (D): 10 μm.

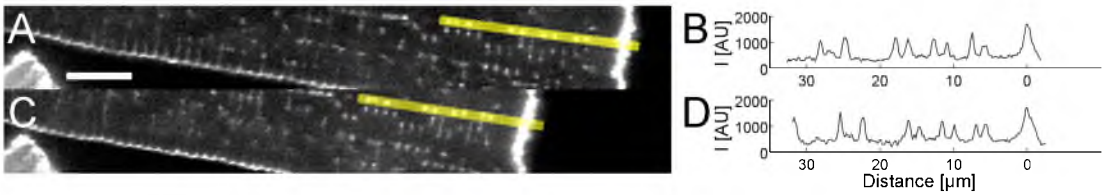

Fig. 4.2. Example of manual strain measurement. (A) Cell at rest with line of interest along longitudinal axis of cell starting at cell end. (B) Intensity profile of line shown in (A). (C) Line of interest drawn in cell at peak contraction. (D) Intensity profile of line shown in (C). Scale bar in (A) applies to (B): 10 µm.

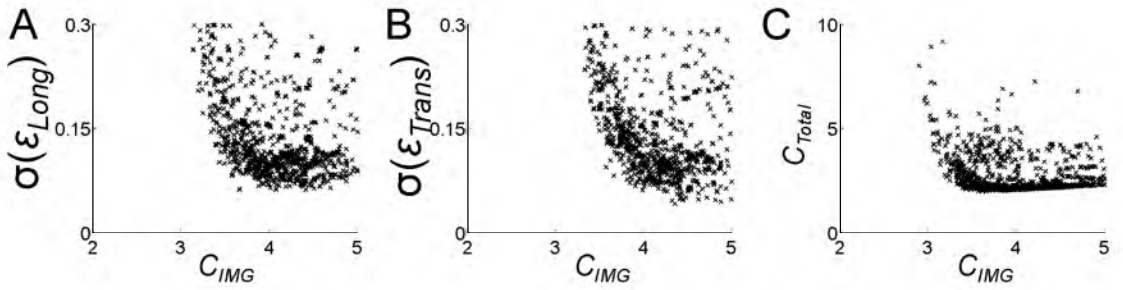

Fig 4.3. Parameter sensitivity study on cropped synthetic cell. (A) Scatter plot of standard deviation of longitudinal strain $\sigma(\varepsilon_{Long})$ versus cost of image similarity C_{IMG}. (B) Scatter plot of standard deviation of transverse strain $\sigma(\varepsilon_{Trans})$ versus C_{IMG}. (C) Scatter plot of total cost C_{Total} versus C_{IMG}.

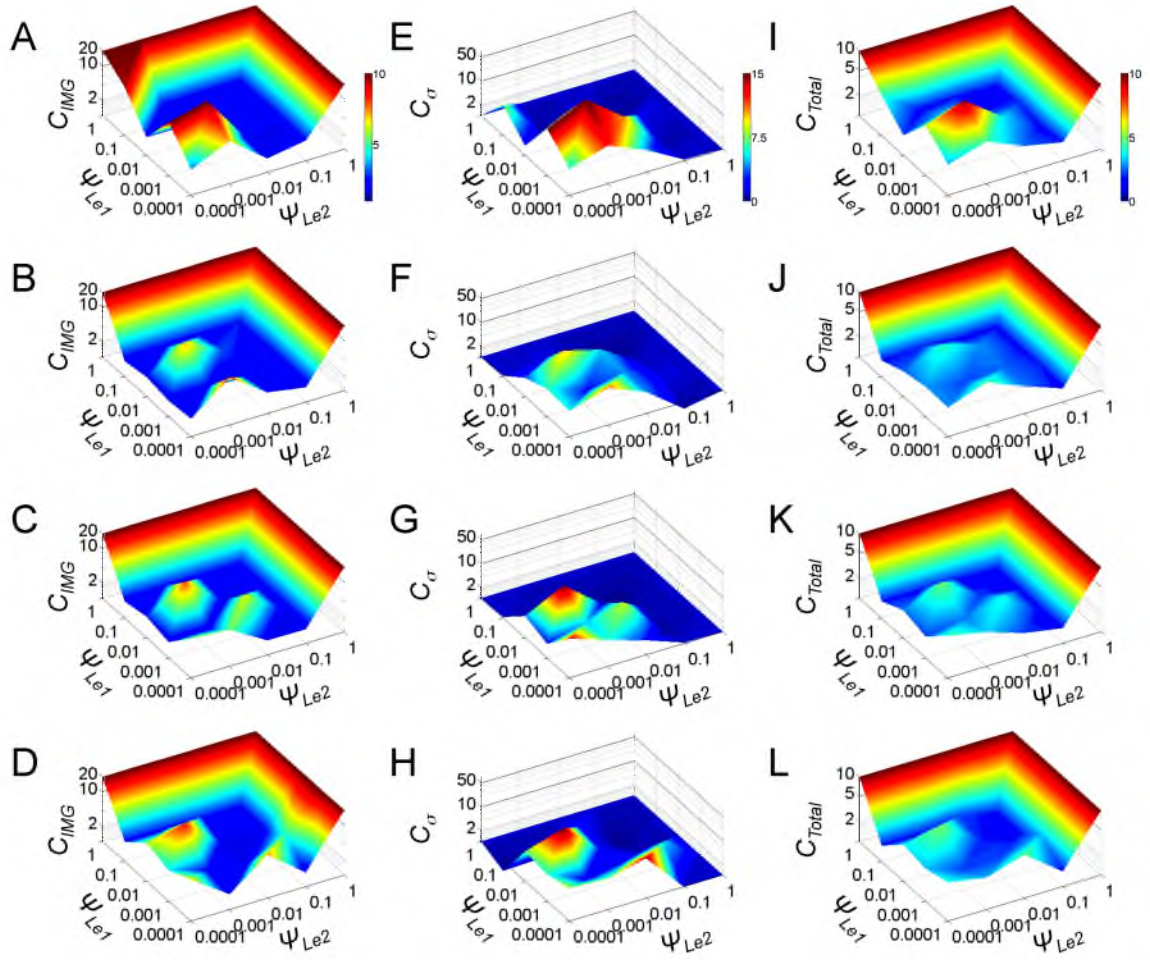

Fig 4.4. Parameter sensitivity study on cropped synthetic cell. (A-D) Costs related to image similarity C_{IMG}. (E-H) Costs related to standard deviation of strain C_{σ}. (I-L) Total cost C_{Total}. Bending weights ψ_{Be} were set to (A, E, I) 10^{-5}, (B, F, J) 10^{-6}, (C, G, K) 10^{-7} and (D, H, L) 10^{-8}. Colorbars in (A, E, and I) apply to all plots of the respective costs.

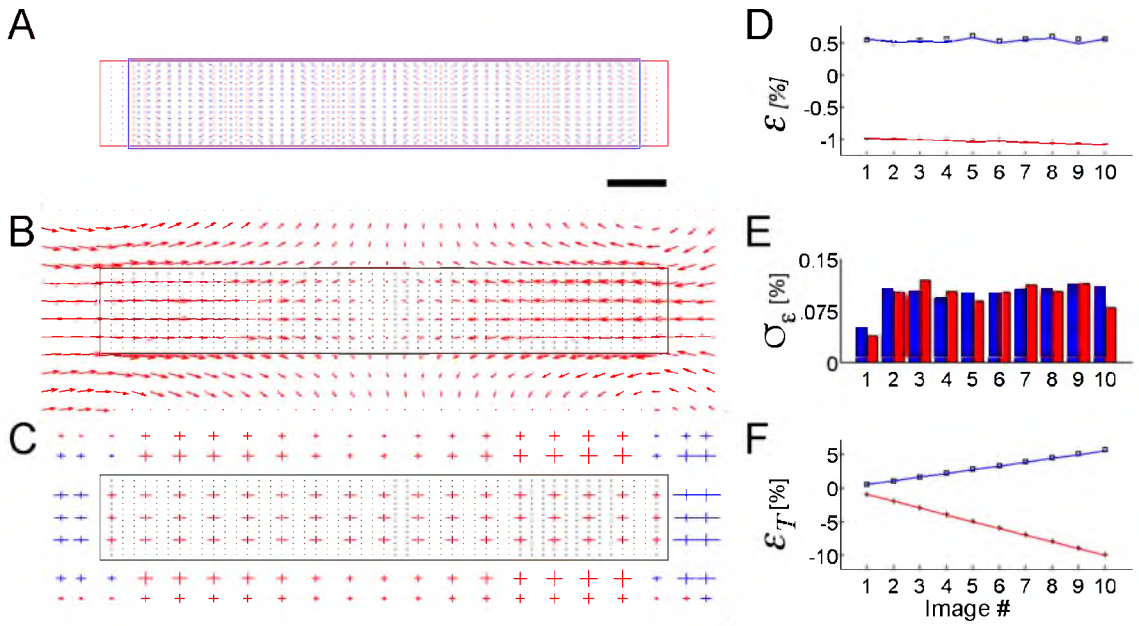

Fig 4.5. Strain measurement in complete, unrotated synthetic cell. (A) Cell at 0% (red) and -10% ε_{Long} (blue). (B) Displacements and (C) strain tensors associated with -10% ε_{Long} overlaid on cell at 0% ε_{Long}. Red and blue color represent shortening and dilation, respectively, along the x-axis. (D) Calculated strain for each frame using a stochastic optimization approach (red and blue) versus a static parameter approach (□ and +). Transverse strain shown in blue and □, longitudinal strain in red and +. (E) Standard deviation of the longitudinal (red) and transverse (blue) strain for each frame. (F) Total strain using the stochastic optimization approach (red and blue) versus a static parameter approach (□ and +). Transverse strain shown in blue and □, longitudinal strain in red and +. Scale bar in (A) applies to (B) and (C): 10 μm.

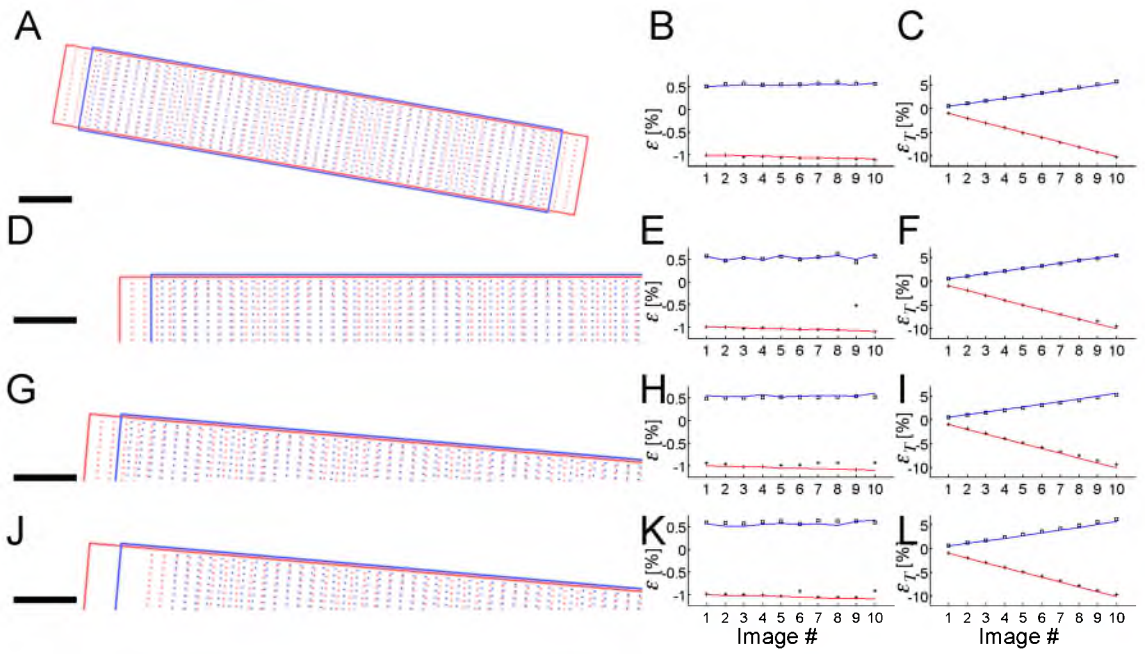

Fig. 4.6. Strain measurement in synthetic cells. (A, D, G, J) Images of cells with 0% (red) and -10% ε_{Long} (blue). (A) Fully padded synthetic cell rotated by 10˚. (D) Cropped synthetic cell with no rotation. (G) Cropped synthetic cell rotated by 5˚. (J) Cropped synthetic cell rotated by 5˚ and detubulated within 10 μm of cell end. (B, E, H, K) Incremental strain and (C, F, I, L) total strain for each frame in the longitudinal (red) and transverse (blue) directions. Results from the stochastic parameter optimization approach (red and blue lines) are contrasted with results from the static parameter approach (□ and +). Scale bars: 10 μm.

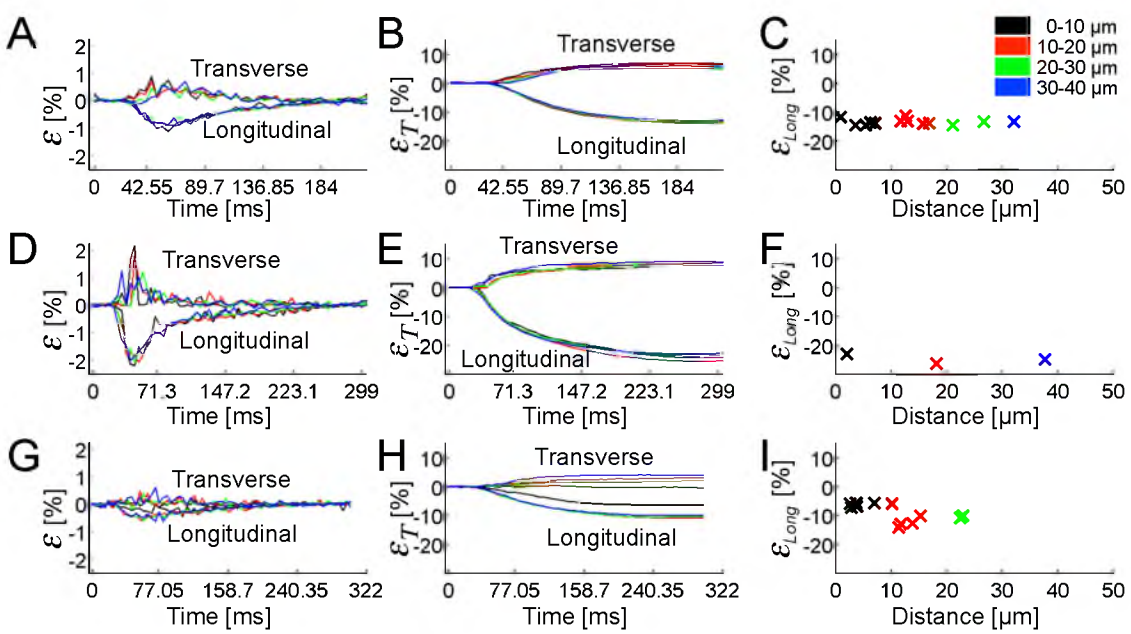

Fig. 4.7. Strain measurement in ventricular cardiomyocytes. (A, D, G) Incremental and (B, E, H) total ε_{Long}. (C, F, I) Manual measurement of ε_{Long}. Calculated ε_{Long} in (A-C) control cell, (D-F) control cell/Iso and (G-I) DHF cell.

4.6 Supplemental Material

4.6.1 Cell Preparation

For cell isolation, animals were anesthetized by propofol injection and isoflurane inhalation. After the heart was excised, it was Langendorff-perfused with a Ca^{2+} free modified Tyrode's solution comprising (in mM) NaCl 92, KCl 4.4, $MgCl_2$ 5, NaH_2PO_4 5, D-glucose 11, HEPES 24, NaOH 12.5, Taurine 20, Creatine 5, Na^+ Pyruvate 1. Myocytes were isolated via enzymatic digestion of the tissue by addition of Collagenase P (0.1-0.2 mg/ml, Roche Diagnostics, Indianapolis, IN, USA), Protease Type XIV (0.06 mg/ml, Sigma-Aldrich, St. Louis, MO, USA) and 50 μM Ca^{2+} to the perfusate. While perfusing with enzyme solution, tissue was periodically checked for structural integrity. When cells freely released from the tissue (~30 min), the enzyme perfusate was stopped and the heart was perfused with modified Tyrode's solution containing 50 μM Ca^{2+} for 10 min. Tissue chunks from the left lateral wall were removed with a scalpel and placed into the washout solution. The tissue was mechanically homogenized using scissors and then gently shaken at 37°C for 10 min. We removed tissue chunks from the solution using a metallic mesh screen. Bath Ca^{2+} was increased to 1 mM in 4 steps over 24 min.

4.6.2 Nonrigid Image Registration based on B-Splines

The transformation **T** is described as the 2D tensor product of the cubic B-splines: [66]

$$\mathbf{T}(x,y) = \sum_{m}^{3}\sum_{n}^{3} B_m(u)B_n(v)\theta_{i+m,j+n} \quad (11)$$

Here θ denotes an $n_x \times n_y$ mesh of control points with uniform spacing. The indices in the mesh are calculated by $i = \left\lfloor \frac{x}{n_x} \right\rfloor - 1$, $j = \left\lfloor \frac{y}{n_y} \right\rfloor - 1$, $u = \frac{x}{n_x} - \left\lfloor \frac{x}{n_x} \right\rfloor$, $v = \frac{y}{n_y} - \left\lfloor \frac{y}{n_y} \right\rfloor$. B_i represents the i-th basis function of the B-spline defined as:

$$B_0(u) = \frac{(1-u)^3}{6} \quad (12)$$

$$B_1(u) = \frac{(3u^3 - 6u^2 + 4)^3}{6} \quad (13)$$

$$B_2(u) = \frac{(-3u^3 + 3u^2 + 3u + 1)^3}{6} \quad (14)$$

$$B_3(u) = \frac{u^3}{6} \quad (15)$$

The method applies a multilevel approach iteratively increasing the resolution of the control point mesh. The sum of transformation at different levels $\mathbf{T}^l$ defines the overall local transformation

$$\mathbf{T}(x,y) = \sum_{l=1}^{L} \mathbf{T}^l(x,y) \quad (16)$$

where L is the total number of mesh levels. This reduces computational complexity since we simply insert new control points into the previous mesh in order to create the mesh at level $l+1$. Enforcing the rule that the control point mesh spacing is halved every step identifies the position of control point $\theta_{2i,2j}^{l+1}$ as the same as $\theta_{i,j}^{l}$, thus allowing the values of the new control points θ^{l+1} to be

calculated directly from those of θ^l using a B-spline subdivision.[78] The number of subdivisions in all presented studies was 6.

The optimal transformation for a control point mesh was calculated by minimizing a cost function comprising 4 different costs. A cost related to image similarity was calculated as the squared sum of intensity differences between the reference image $\mathbf{I_{ref}}$ and transformed image $\mathbf{I_{def}}$:

$$C_{SSD} = \frac{1}{N}\sqrt{\sum_{n=1}^{N}(\mathbf{I_{ref}}(n) - \mathbf{I_{def}}(n))^2} \quad (17)$$

with the total number of pixels N.

A cost associated with the bending energy was determined from second-order derivatives of the transformation:

$$C_{Be} = \frac{1}{A}\int_0^Y \int_0^X \left(\left(\frac{\partial^2 \mathbf{T}}{\partial x^2}\right)^2 + \left(\frac{\partial^2 \mathbf{T}}{\partial y^2}\right)^2 + 2\left(\frac{\partial^2 \mathbf{T}}{\partial xy}\right)^2\right) dydx \quad (18)$$

Two costs dependent on the linear elasticity were determined from first-order derivatives of the transformation:

$$C_{Le_1} = \frac{1}{A}\int_0^Y \int_0^X \left(\left(\frac{\partial \mathbf{T}_x}{\partial x}\right)^2 + \left(\frac{\partial \mathbf{T}_y}{\partial y}\right)^2 + \frac{1}{2}\left(\frac{\partial \mathbf{T}_x}{\partial y} + \frac{\partial \mathbf{T}_y}{\partial x}\right)^2\right) dydx \quad (19)$$

$$C_{Le_2} = \frac{1}{A}\int_0^Y \int_0^X \left(\left(\frac{\partial \mathbf{T}_x}{\partial x}\right)^2 + \left(\frac{\partial \mathbf{T}_y}{\partial y}\right)^2\right) dydx \quad (20)$$

4.6.3 Implementation

Image sequences from rapid-scanning confocal microscopy of ventricular cardiomyocytes were processed as described in the Methods section and saved as individual frames for registration. Synthetic cells were also saved as individual frames, but no further processing was performed on them after rendering. The input of the algorithm consisted of the 2 images, an angle to orient the strain calculation with, the range from the cell end to use for the cost calculations and the weights for the cost of the bending and 2 linear elasticity terms. The algorithm then performed the registration on the given frames and returned values of mean ε_{Long} and ε_{Trans}, the standard deviation of ε_{Long} and ε_{Trans}, the image registration cost and the total cost $\mathrm{C_{Total}}$. In images of the synthetic cells the entire visible cell interior was used for calculating the error and strains. In the image sequences from live cardiomyocytes specific 10 μm ranges were examined.

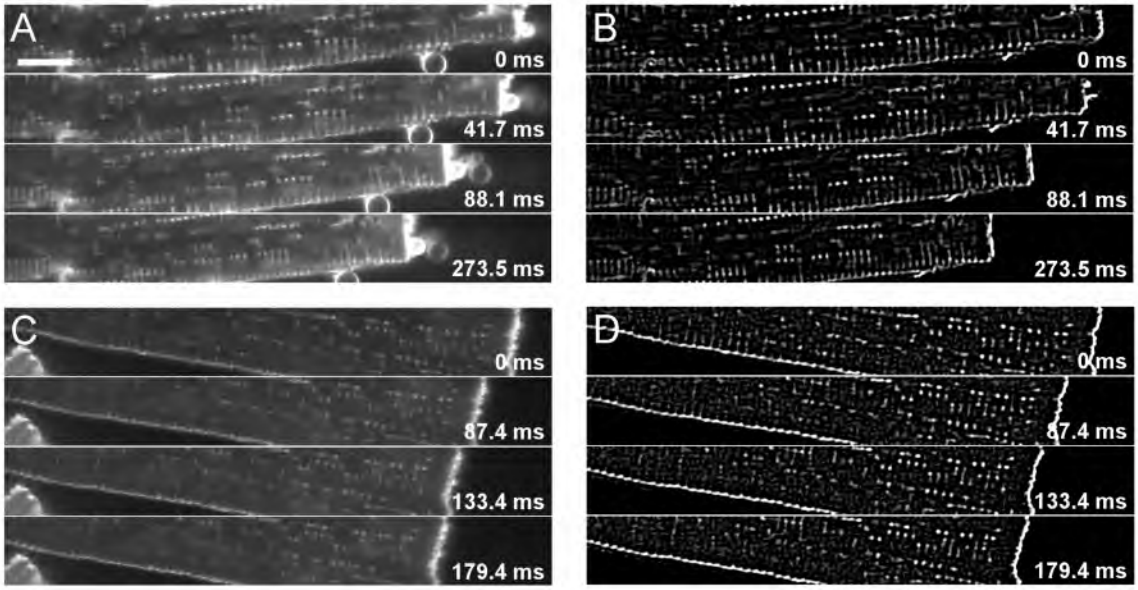

Fig. S4.1. (A) Images of Di-8-Anepps labelled left ventricular myocyte from control animal in the presence of isoproterenol in the bath solution. (B) Corresponding pre-processed images. Image processing comprised filtering and masking. (C) Images of Di-8-Anepps labeled DHF cell. (D) Corresponding pre-processed images. Scale bar in (A) applies to (B), (C) and (D): 10 μm

CHAPTER 5

SUMMARY AND PERSPECTIVES

In summary, this dissertation presents multiple findings of previously unknown microstructural remodeling based on novel methods of microscopic imaging and image analyses. Using Fourier analysis, we found that the spatial regularity of α-actinin was drastically reduced during DHF. In addition to disruption of the spatial regularity, we also showed a novel remodeling of α-actinin in the form of longitudinal depositions spanning neighboring Z-disks. This particular remodeling was specific to α-actinin and not present in the other examined sarcomeric proteins. Using super resolution confocal microscopy we were able to determine that these longitudinal depositions were approximately half as dense as the standard Z-disk. Additionally, CRT reversed disruption of the spatial regularity of the Z-disk, however, CRT was not able to reduce the occurrence of longitudinal depositions.

The finding that remodeling of the t-system and RyR clusters is heterogeneous within cells during DHF was also a novel insight for the field. We found that detubulation of cells during DHF was significantly more prominent near the longitudinal cell ends. Furthermore, this finding was localized to cells isolated from the left ventricular free wall. In addition to de-tubulation, RyR

density and fluorescence intensity were significantly increased near the longitudinal cell ends. According to a recent model of Ca^{2+} release,[75] this heterogeneous remodeling of t-system and RyR clusters will result in a heterogeneous Ca^{2+} transient within the cell. Specifically, this remodeling will result in delayed onset times and reduced amplitudes at cell ends versus cell centers. Structural remodeling of t-system and RyR clusters was also associated with a functional remodeling. A decrease in spontaneous Ca^{2+} release events was associated with areas showing significant detubulation, even though RyR intensity was increased. This finding supports the idea that RyR clusters have varying Ca^{2+} release probabilities, depending on their distance to t-system.

While there are numerous studies describing microstructural remodeling in cardiac ventricular myocytes during various forms of HF and disease states, the studies presented in this dissertation are among the first to describe any form of microstructural remodeling during DHF and after CRT.

Sarcomeric disruption is a common phenotype during many disease states. In cardiomyocytes infected with *Typsanoma Cruzi*, the parasite responsible for Chagas disease, the periodic arrangement of α-actinin is completely lost and α-actinin becomes localized to focal adhesion sites.[31] Electron microscopy revealed that during arrhythmogenic right ventricular cardiomyopathy the sarcomeric arrangement is disturbed by accumulation of electron-dense material around the Z-disk, and this material extended in various directions and filled the entirety of the sarcomere space.[32] Similar disruption was found in skeletal myocytes from patients with nemaline myopathy, a skeletal

myopathy that primarily affects muscles of the limbs, neck and face.[32] A missense mutation in the gene responsible for the primary cardiac isoform of α-actinin, *ACTN2*, is highly conserved in patients experiencing hypertrophic cardiomyopathy.[79] Genetic studies have shown mutations in this gene to be a direct cause of hypertrophic cardiomyopathy.[80] The work in this thesis takes these findings in structural alterations of α-actinin and expands on this knowledge in relation to DHF. Additionally, this work is the first to explore the ability of α-actinin to be reverse remodeled from a diseased to a healthy phenotype after CRT. The findings presented here support the idea that sarcomeric remodeling occurs in two stages. An initial reversible stage characterized by an accumulation of cytoskeletal proteins in order to offset the strain imposed on the myocardium, followed by an irreversible stage characterized by the loss of contractile filaments.[81]

A previous study found that t-system is depleted during DHF, specifically in myocytes isolated from the left lateral wall, and that this depletion was reversed after CRT.[46] Part of the work in this dissertation serves as a follow-up to this study, showing that this depletion of t-system preferentially occurs within 10 μm of the longitudinal cell ends. In addition to the increased number of nonjunctional RyR clusters, this work found the novel result that these nonjunctional RyR clusters have an increased size and density. Furthermore, this remodeling had an effect on Ca^{2+} handling within the cells. In myocytes isolated from the left lateral wall of animals experiencing DHF, within 10 μm of the longitudinal cell end there was a significantly reduced occurrence of spontaneous

Ca^{2+} release events. This finding is not intuitive since it is easy to imagine that an up-regulation in RyR intensity would result in a higher amount of Ca^{2+} leak from the sarcoplasmic reticulum. Instead we found the opposite, suggesting the importance of the t-system presence in these spontaneous release events.

Characterizing strain within contracting myocytes exposes the fundamental mechanical properties of the cells. Within myocytes are a variety of cellular pathways that respond to physical stimuli.[82-85] Understanding the mechanical properties of the myocyte would help elicit how external physical stimuli, like stretch or strain, are transmitted to the internal machinery. Not only is this information useful for understanding physiological processes, it is also necessary for the creation of more thorough computational models. Many methods have been developed to characterize strain within cells,[56-58,61-63,86,87] however, the majority of these studies rely on either line-scan microscopy, which yields information on a very small portion of the cell in only 1D, or they used some method to obtain an average shortening for the entire cell. In all of these methods, only longitudinal strain is described, and regional differences of this strain within the cells would be difficult to determine. In this dissertation I present a method that uses fast scanning confocal microscopy to describe the longitudinal and transverse strain tensor in 2D at an unprecedented spatial and temporal resolution. The ability to describe the strain tensor in such detail is a significant contribution to the field. Using this technique with various fluorescent labels would allow investigation into how specific protein structures affect local strain generation. Additionally, the data obtained and presented with this method

suggest that in DHF strain amplitude is substantially reduced within 10 μm of the cell end, indicating further functional consequences of the structural remodeling described throughout this thesis.

Combined, the research presented in this thesis constitutes a significant advancement of knowledge on the microstructural remodeling that occurs within cardiomyocytes during DHF and their restoration after CRT. The knowledge presented here will lead towards a better understanding of this disease state and help guide the development of future studies. In order to combat the growing epidemic of HF, many physicians believe that within the next few decades we will see a paradigm shift towards personalized medicine, where patients are treated according to their personalized symptoms and body chemistry instead of being lumped into broad categories of disease. One could envision a diagnostic method in which microscopic images are obtained from hearts of patients using minimally invasive procedures and then examined for specific biomarkers or protein distributions. Using the information obtained with these biopsies, physicians would be able to make a better prediction as to how well treatments like CRT will work for a specific patient, and then prescribe therapies accordingly. In order to reach this goal of personalized medicine, a deeper understanding of what goes wrong in specific disease states will be necessary. While this is beyond the scope of this work, as a whole this dissertation significantly contributes to the knowledge available for DHF and CRT.

REFERENCES

1. Roth GA, Huffman MD, Moran AE, Feigin V, Mensah GA, Naghavi M, Murray CJ. Global and Regional Patterns in Cardiovascular Mortality From 1990 to 2013. *Circulation*. 2015;132:1667-78.

2. Mendis S, Puska P, Norrving B, World Health Organization., World Heart Federation., World Stroke Organization. *Global atlas on cardiovascular disease prevention and control*. Geneva: World Health Organization in collaboration with the World Heart Federation and the World Stroke Organization; 2011.

3. Mozaffarian D, Benjamin EJ, Go AS, Arnett DK, Blaha MJ, Cushman M, de Ferranti S, Despres JP, Fullerton HJ, Howard VJ, Huffman MD, Judd SE, Kissela BM, Lackland DT, Lichtman JH, Lisabeth LD, Liu S, Mackey RH, Matchar DB, McGuire DK, Mohler ER, 3rd, Moy CS, Muntner P, Mussolino ME, Nasir K, Neumar RW, Nichol G, Palaniappan L, Pandey DK, Reeves MJ, Rodriguez CJ, Sorlie PD, Stein J, Towfighi A, Turan TN, Virani SS, Willey JZ, Woo D, Yeh RW, Turner MB, American Heart Association Statistics C, Stroke Statistics S. Heart disease and stroke statistics--2015 update: a report from the American Heart Association. *Circulation*. 2015;131:e29-322.

4. Roth GA, Nguyen G, Forouzanfar MH, Mokdad AH, Naghavi M, Murray CJ. Estimates of Global and Regional Premature Cardiovascular Mortality in 2025. *Circulation*. 2015;132:1270-82.

5. Mudd JO, Kass DA. Tackling heart failure in the twenty-first century. *Nature*. 2008;451:919-28.

6. Ford ES, Ajani UA, Croft JB, Critchley JA, Labarthe DR, Kottke TE, Giles WH, Capewell S. Explaining the decrease in U.S. deaths from coronary disease, 1980-2000. *N Engl J Med*. 2007;356:2388-98.

7. Roth GA, Forouzanfar MH, Moran AE, Barber R, Nguyen G, Feigin VL, Naghavi M, Mensah GA, Murray CJ. Demographic and epidemiologic drivers of global cardiovascular mortality. *N Engl J Med*. 2015;372:1333-41.

8. Jessup M, Brozena S. Heart failure. *N Engl J Med*. 2003;348:2007-18.

9. Xin M, Olson EN, Bassel-Duby R. Mending broken hearts: cardiac development as a basis for adult heart regeneration and repair. *Nat Rev Mol Cell Biol*. 2013;14:529-41.

10. Severs NJ. The cardiac muscle cell. *Bioessays*. 2000;22:188-99.

11. Bers DM. Cardiac excitation-contraction coupling. *Nature*. 2002;415:198-205.2. Hwang PM, Sykes BD. Targeting the sarcomere to correct muscle function. *Nat Rev Drug Discov*. 2015;14:313-28.

12. Hwang PM, Sykes BD. Targeting the sarcomere to correct muscle function. *Nat Rev Drug Discov*. 2015;14:313-28.

13. Dabiri GA, Turnacioglu KK, Sanger JM, Sanger JW. Myofibrillogenesis visualized in living embryonic cardiomyocytes. *Proc Natl Acad Sci U S A*. 1997;94:9493-8.

14. Wang J, Shaner N, Mittal B, Zhou Q, Chen J, Sanger JM, Sanger JW. Dynamics of Z-band based proteins in developing skeletal muscle cells. *Cell Motil Cytoskeleton*. 2005;61:34-48.

15. Frank D, Kuhn C, Katus HA, Frey N. The sarcomeric Z-disc: a nodal point in signalling and disease. *J Mol Med (Berl)*. 2006;84:446-68.

16. Otey CA, Carpen O. Alpha-actinin revisited: a fresh look at an old player. *Cell Motil Cytoskeleton*. 2004;58:104-11.

17. Michela P, Velia V, Aldo P, Ada P. Role of connexin 43 in cardiovascular diseases. *Eur J Pharmacol*. 2015;768:71-76.

18. Lackey DP, Carruth ED, Lasher RA, Boenisch J, Sachse FB, Hitchcock RW. Three-dimensional modeling and quantitative analysis of gap junction distributions in cardiac tissue. *Ann Biomed Eng*. 2011;39:2683-94.

19. Ibrahim E-SH. *Heart Mechanics: Magnetic Resonance Imaging*: CRC Press; 2014.

20. Grant AO. Cardiac ion channels. *Circ Arrhythm Electrophysiol*. 2009;2:185-94.

21. Randall DJ, Burggren WW, French K, Eckert R. *Eckert animal physiology : mechanisms and adaptations.* Ed. 5 ed. New York: W.H. Freeman and Co.; 2002.

22. Sandri M. Signaling in muscle atrophy and hypertrophy. *Physiology (Bethesda)*. 2008;23:160-70.

23. Schoenfeld BJ. The mechanisms of muscle hypertrophy and their application to resistance training. *J Strength Cond Res*. 2010;24:2857-72.

24. Frey N, Katus HA, Olson EN, Hill JA. Hypertrophy of the heart: a new therapeutic target? *Circulation*. 2004;109:1580-9.

25. Dargie H. Heart failure post-myocardial infarction: a review of the issues. *Heart*. 2005;91 Suppl 2:ii3-6; discussion ii31, ii43-8.

26. Mone SM, Sanders SP, Colan SD. Control mechanisms for physiological hypertrophy of pregnancy. *Circulation*. 1996;94:667-72.

27. Pluim BM, Zwinderman AH, van der Laarse A, van der Wall EE. The athlete's heart. A meta-analysis of cardiac structure and function. *Circulation*. 2000;101:336-44.

28. Drazner MH. The progression of hypertensive heart disease. *Circulation*. 2011;123:327-34.

29. Segura AM, Frazier OH, Buja LM. Fibrosis and heart failure. *Heart Fail Rev*. 2014;19:173-85.

30. Gorelik J, Yang LQ, Zhang Y, Lab M, Korchev Y, Harding SE. A novel Z-groove index characterizing myocardial surface structure. *Cardiovasc Res*. 2006;72:422-9.

31. Melo TG, Almeida DS, Meirelles MN, Pereira MC. Disarray of sarcomeric alpha-actinin in cardiomyocytes infected by Trypanosoma cruzi. *Parasitology*. 2006;133:171-8.

32. Oxford EM, Danko CG, Kornreich BG, Maass K, Hemsley SA, Raskolnikov D, Fox PR, Delmar M, Moise NS. Ultrastructural changes in cardiac myocytes from Boxer dogs with arrhythmogenic right ventricular cardiomyopathy. *J Vet Cardiol*. 2011;13:101-13.

33. Balijepalli RC, Lokuta AJ, Maertz NA, Buck JM, Haworth RA, Valdivia HH, Kamp TJ. Depletion of T-tubules and specific subcellular changes in sarcolemmal proteins in tachycardia-induced heart failure. *Cardiovasc Res*. 2003;59:67-77.

34. Hasenfuss G. Alterations of calcium-regulatory proteins in heart failure. *Cardiovasc Res*. 1998;37:279-89.

35. He J, Conklin MW, Foell JD, Wolff MR, Haworth RA, Coronado R, Kamp TJ. Reduction in density of transverse tubules and L-type Ca(2+) channels in canine tachycardia-induced heart failure. *Cardiovasc Res*. 2001;49:298-307.

36. Wei S, Guo A, Chen B, Kutschke W, Xie YP, Zimmerman K, Weiss RM, Anderson ME, Cheng H, Song LS. T-tubule remodeling during transition from hypertrophy to heart failure. *Circ Res*. 2010;107:520-31.

37. Lou Q, Janardhan A, Efimov IR. Remodeling of calcium handling in human heart failure. *Adv Exp Med Biol*. 2012;740:1145-74.

38. Coronel R, Wilders R, Verkerk AO, Wiegerinck RF, Benoist D, Bernus O. Electrophysiological changes in heart failure and their implications for arrhythmogenesis. *Biochim Biophys Acta*. 2013;1832:2432-41.

39. Turer AT. Using metabolomics to assess myocardial metabolism and energetics in heart failure. *J Mol Cell Cardiol*. 2013;55:12-8.

40. Grines CL, Bashore TM, Boudoulas H, Olson S, Shafer P, Wooley CF. Functional abnormalities in isolated left bundle branch block. The effect of interventricular asynchrony. *Circulation*. 1989;79:845-53.

41. Iuliano S, Fisher SG, Karasik PE, Fletcher RD, Singh SN, Department of Veterans Affairs Survival Trial of Antiarrhythmic Therapy in Congestive Heart F. QRS duration and mortality in patients with congestive heart failure. *Am Heart J*. 2002;143:1085-91.

42. Aiba T, Hesketh GG, Barth AS, Liu T, Daya S, Chakir K, Dimaano VL, Abraham TP, O'Rourke B, Akar FG, Kass DA, Tomaselli GF. Electrophysiological consequences of dyssynchronous heart failure and its restoration by resynchronization therapy. *Circulation*. 2009;119:1220-30.

43. Chakir K, Daya SK, Aiba T, Tunin RS, Dimaano VL, Abraham TP, Jaques-Robinson KM, Lai EW, Pacak K, Zhu WZ, Xiao RP, Tomaselli GF, Kass DA. Mechanisms of enhanced beta-adrenergic reserve from cardiac resynchronization therapy. *Circulation*. 2009;119:1231-40.

44. Helm RH, Byrne M, Helm PA, Daya SK, Osman NF, Tunin R, Halperin HR, Berger RD, Kass DA, Lardo AC. Three-dimensional mapping of optimal left ventricular pacing site for cardiac resynchronization. *Circulation*. 2007;115:953-61.

45. Barth AS, Aiba T, Halperin V, DiSilvestre D, Chakir K, Colantuoni C, Tunin RS, Dimaano VL, Yu W, Abraham TP, Kass DA, Tomaselli GF. Cardiac resynchronization therapy corrects dyssynchrony-induced regional gene expression changes on a genomic level. *Circ Cardiovasc Genet*. 2009;2:371-8.

46. Sachse FB, Torres NS, Savio-Galimberti E, Aiba T, Kass DA, Tomaselli GF, Bridge JH. Subcellular structures and function of myocytes impaired during heart failure are restored by cardiac resynchronization therapy. *Circ Res*. 2012;110:588-97.

47. Butler J, Fonarow GC, Zile MR, Lam CS, Roessig L, Schelbert EB, Shah SJ, Ahmed A, Bonow RO, Cleland JG, Cody RJ, Chioncel O, Collins SP, Dunnmon P, Filippatos G, Lefkowitz MP, Marti CN, McMurray JJ, Misselwitz F, Nodari S, O'Connor C, Pfeffer MA, Pieske B, Pitt B, Rosano G, Sabbah HN, Senni M, Solomon SD, Stockbridge N, Teerlink JR, Georgiopoulou VV, Gheorghiade M. Developing therapies for heart failure with preserved ejection fraction: current state and future directions. *JACC Heart Fail*. 2014;2:97-112.

48. Abraham WT. Cardiac resynchronization therapy for the management of chronic heart failure. *Am Heart Hosp J*. 2003;1:55-61.

49. Abraham WT, Hayes DL. Cardiac resynchronization therapy for heart failure. *Circulation*. 2003;108:2596-603.

50. Blanc JJ, Etienne Y, Gilard M, Mansourati J, Munier S, Boschat J, Benditt DG, Lurie KG. Evaluation of different ventricular pacing sites in patients with severe heart failure: results of an acute hemodynamic study. *Circulation*. 1997;96:3273-7.

51. Kass DA, Chen CH, Curry C, Talbot M, Berger R, Fetics B, Nevo E. Improved left ventricular mechanics from acute VDD pacing in patients with dilated cardiomyopathy and ventricular conduction delay. *Circulation*. 1999;99:1567-73.

52. Nelson GS, Berger RD, Fetics BJ, Talbot M, Spinelli JC, Hare JM, Kass DA. Left ventricular or biventricular pacing improves cardiac function at diminished energy cost in patients with dilated cardiomyopathy and left bundle-branch block. *Circulation*. 2000;102:3053-9.

53. Cleland JG, Daubert JC, Erdmann E, Freemantle N, Gras D, Kappenberger L, Tavazzi L, Cardiac Resynchronization-Heart Failure Study I. The effect of cardiac resynchronization on morbidity and mortality in heart failure. *N Engl J Med*. 2005;352:1539-49.

54. Chakir K, Daya SK, Tunin RS, Helm RH, Byrne MJ, Dimaano VL, Lardo AC, Abraham TP, Tomaselli GF, Kass DA. Reversal of global apoptosis and regional stress kinase activation by cardiac resynchronization. *Circulation*. 2008;117:1369-77.

55. Tameyasu T, Toyoki T, Sugi H. Nonsteady motion in unloaded contractions of single frog cardiac cells. *Biophys J*. 1985;48:461-5.

56. Harris PJ, Stewart D, Cullinan MC, Delbridge LM, Dally L, Grinwald P. Rapid measurement of isolated cardiac muscle cell length using a line-scan camera. *IEEE Trans Biomed Eng*. 1987;34:463-7.

57. London B, Krueger JW. Contraction in voltage-clamped, internally perfused single heart cells. *J Gen Physiol*. 1986;88:475-505.

58. Philips CM, Duthinh V, Houser SR. A simple technique to measure the rate and magnitude of shortening of single isolated cardiac myocytes. *IEEE Trans Biomed Eng*. 1986;33:929-34.

59. Steadman BW, Moore KB, Spitzer KW, Bridge JHB. A video system for measuring motion in contracting heart cells. *IEEE Transactions on Biomedical Engineering*. 1988;35:264-272.

60. Lecarpentier Y, Martin JL, Claes V, Chambaret JP, Migus A, Antonetti A, Hatt PY. Real-time kinetics of sacromere relaxation by laser diffraction. *Circulation research*. 1985;56:331-339.

61. Goldman YE. Measurement of sarcomere shortening in skinned fibers from frog muscle by white light diffraction. *Biophys J*. 1987;52:57-68.

62. Bub G, Camelliti P, Bollensdorff C, Stuckey DJ, Picton G, Burton RA, Clarke K, Kohl P. Measurement and analysis of sarcomere length in rat cardiomyocytes in situ and in vitro. *Am J Physiol Heart Circ Physiol*. 2010;298:H1616-25.

63. McNary TG, Bridge JH, Sachse FB. Strain transfer in ventricular cardiomyocytes to their transverse tubular system revealed by scanning confocal microscopy. *Biophys J*. 2011;100:L53-5.

64. Lichter JG, Carruth E, Mitchell C, Barth AS, Aiba T, Kass DA, Tomaselli GF, Bridge JH, Sachse FB. Remodeling of the sarcomeric cytoskeleton in cardiac ventricular myocytes during heart failure and after cardiac resynchronization therapy. *Journal of molecular and cellular cardiology*. 2014;72:186-95.

65. Li H, Lichter JG, Seidel T, Tomaselli GF, Bridge JH, Sachse FB. Cardiac Resynchronization Therapy Reduces Subcellular Heterogeneity of Ryanodine Receptors, T-Tubules, and Ca2+ Sparks Produced by Dyssynchronous Heart Failure. *Circ Heart Fail*. 2015;8:1105-14.

66. Rueckert D, Sonoda LI, Hayes C, Hill DL, Leach MO, Hawkes DJ. Nonrigid registration using free-form deformations: application to breast MR images. *IEEE Trans Med Imaging*. 1999;18:712-21.

67. Li H, Lichter JG, Seidel T, Tomaselli GF, Bridge JH, Sachse FB. Cardiac Resynchronization Therapy Reduces Subcellular Heterogeneity of Ryanodine Receptors, T-Tubules and Ca2+ Sparks Produced by Dyssynchronous Heart Failure. *Circ Heart Fail*. 2015.

68. Schwab BC, Seemann G, Lasher RA, Torres NS, Wulfers EM, Arp M, Carruth ED, Bridge JH, Sachse FB. Quantitative analysis of cardiac tissue including fibroblasts using three-dimensional confocal microscopy and image

reconstruction: towards a basis for electrophysiological modeling. *IEEE Trans Med Imaging*. 2013;32:862-72.

69. Seidel T, Dräbing T, Seemann G, Sachse FB. A semi-automatic approach for segmentation of three-dimensional microscopig image stacks of cardiac tissue. *Lecture Notes in Computer Science*. 2013;7945:7.

70. Schneider CA, Rasband WS, Eliceiri KW. NIH Image to ImageJ: 25 years of image analysis. *Nature methods*. 2012;9:671-5.

71. Abbruzzese J, Sachse FB, Tristani-Firouzi M, Sanguinetti MC. Modification of hERG1 channel gating by Cd2+. *J Gen Physiol*. 2010;136:203-24.

72. Modat M, Ridgway GR, Taylor ZA, Lehmann M, Barnes J, Hawkes DJ, Fox NC, Ourselin S. Fast free-form deformation using graphics processing units. *Comput Methods Programs Biomed*. 2010;98:278-84.

73. Chakir K, Depry C, Dimaano VL, Zhu WZ, Vanderheyden M, Bartunek J, Abraham TP, Tomaselli GF, Liu SB, Xiang YK, Zhang M, Takimoto E, Dulin N, Xiao RP, Zhang J, Kass DA. Galphas-biased beta2-adrenergic receptor signaling from restoring synchronous contraction in the failing heart. *Sci Transl Med*. 2011;3:100ra88.

74. Sachse FB. *Computational cardiology : modeling of anatomy, electrophysiology, and mechanics*. Berlin ; New York: Springer; 2004.

75. Torres NS, Sachse FB, Izu LT, Goldhaber JI, Spitzer KW, Bridge JH. A modified local control model for Ca2+ transients in cardiomyocytes: junctional flux is accompanied by release from adjacent non-junctional RyRs. *J Mol Cell Cardiol*. 2014;68:1-11.

76. Diaspro A. *Confocal and two-photon microscopy : foundations, applications, and advances*. New York: Wiley-Liss; 2002.

77. Goldman RD, Swedlow J, Spector DL. *Live cell imaging : a laboratory manual.* 2nd ed. Cold Spring Harbor, N.Y.: Cold Spring Harbor Laboratory Press; 2010.

78. Forsey DR, Bartels RH. Hierarchical B-spline refinement. *ACM Transactions on Computational Graphics*. 1988;22:7.

79. Bos JM, Ackerman MJ. Z-disc genes in hypertrophic cardiomyopathy: stretching the cardiomyopathies? *J Am Coll Cardiol*. 2010;55:1136-8.

80. Chiu C, Bagnall RD, Ingles J, Yeates L, Kennerson M, Donald JA, Jormakka M, Lind JM, Semsarian C. Mutations in alpha-actinin-2 cause hypertrophic cardiomyopathy: a genome-wide analysis. *J Am Coll Cardiol*. 2010;55:1127-35.

81. Hein S, Kostin S, Heling A, Maeno Y, Schaper J. The role of the cytoskeleton in heart failure. *Cardiovasc Res*. 2000;45:273-8.

82. Knoll R, Hoshijima M, Hoffman HM, Person V, Lorenzen-Schmidt I, Bang ML, Hayashi T, Shiga N, Yasukawa H, Schaper W, McKenna W, Yokoyama M, Schork NJ, Omens JH, McCulloch AD, Kimura A, Gregorio CC, Poller W, Schaper J, Schultheiss HP, Chien KR. The cardiac mechanical stretch sensor machinery involves a Z disc complex that is defective in a subset of human dilated cardiomyopathy. *Cell*. 2002;111:943-55.

83. Komuro I, Kudo S, Yamazaki T, Zou Y, Shiojima I, Yazaki Y. Mechanical stretch activates the stress-activated protein kinases in cardiac myocytes. *FASEB J*. 1996;10:631-6.

84. Kudoh S, Komuro I, Hiroi Y, Zou Y, Harada K, Sugaya T, Takekoshi N, Murakami K, Kadowaki T, Yazaki Y. Mechanical stretch induces hypertrophic responses in cardiac myocytes of angiotensin II type 1a receptor knockout mice. *J Biol Chem*. 1998;273:24037-43.

85. Sadoshima J, Izumo S. Mechanical stretch rapidly activates multiple signal transduction pathways in cardiac myocytes: potential involvement of an autocrine/paracrine mechanism. *EMBO J*. 1993;12:1681-92.

86. Lecarpentier Y, Martin JL, Claes V, Chambaret JP, Migus A, Antonetti A, Hatt PY. Real-time kinetics of sarcomere relaxation by laser diffraction. *Circ Res*. 1985;56:331-9.

87. Steadman BW, Moore KB, Spitzer KW, Bridge JH. A video system for measuring motion in contracting heart cells. *IEEE Trans Biomed Eng*. 1988;35:264-72.